國立交通大學

應用化學系

博 士 論 文

有機分子與有機奈米粒子在溶液中之飛秒螢光動力學研究

Femtosecond fluorescence Dynamics of Organic Molecules and Organic Nanoparticles in Solutions

研 究 生：張智煒

指導教授：刁維光 教授

中 華 民 國 九十六 年 六 月

有機分子與有機奈米粒子在溶液中之飛秒螢光動力學研究

學生:張智煒　　指導教授:刁維光

摘　　要

在本篇論文中,我們利用時間解析螢光光譜對於有機奈米粒子(PPB) 和有機奈米帶 (CNDSB) 的激發態動力學以及螢光增益現象作一深入的探討。在水和 THF 的混合溶液中，我們藉由控制水和 THF 比例生成不同大小的奈米粒子。研究結果顯示，在 PPB 奈米粒子中的螢光增益效應主要是由於在奈米粒子中分子的平面化以及在聚集體(aggregate)中分子和分子間的交互作用所造成。我們利用時間解析螢光光譜以及粉末 X 光繞射 (powder XRD)的量測，發現在 PPB 奈米粒子中，其晶體的排列具有兩種不同的構型。對於 CNDSB 分子，藉由比較 CNDSB 在 THF 和 PMMA 薄膜中的時間解析螢光光譜,我們發現在結構上的限制僅能造成部分的螢光增益效應。然而在 CNDSB 奈米帶中，我們觀測到一十分有趣的超快能量傳遞過程，其時間小於 150 飛秒。由於在 PPB 奈米粒子中，我們並沒觀測到此一現象，因此我們認爲此一超快的能量傳遞過程應該由於 CNDSB 的一維奈米結構所造成,而其反映了能量在奈米帶的長軸方向的傳遞速度。

在第二部份的研究方面，我們針對了一新合成的咔唑(carbazole) 衍生物: BMVC，分別對其在有機溶劑中以及 DNA 錯合物中的激發態及水合動力學做一探討。當 BMVC 溶解於 tris-buffer (PH=7.5)時，其激發態的緩解主要是經由 C=C 雙鍵旋轉所造成的內轉換(internal conversion) 或是 C-C 單鍵旋轉所造成的系統間跨越(intersystem crossing)。也因此當我們將 BMVC 溶解在甘油(glycerol)時，由於分子的轉動受到了限制，其螢光強度以及生命期均大幅的增加。在水合動力學(solvation dynamics)方面，在甘油中由於分子的高黏滯性，因此使得水合時間大幅度的減緩。而當 BMVC 雙股螺旋(duplex)及四股螺旋(quadruplex) DNA 作用時，由於 BMVC 和 DNA 間的作用限制了分子內運動,因此其螢光強度和在甘油中一樣均有大幅度的增加。藉由水合動力學的測量，我們認爲在 DNA 表面的水可分爲兩種，其中之一是屬於自由的水分子，而另一種則屬於和表面有部份結合的水分子。藉由分析此兩種水分子的水合時間，我們認爲 BMVC 在雙股螺旋 DNA 中的結合位置是位於大溝(major groove)以及小溝(minor groove)之間。而當 BMVC 和四股螺旋 DNA 結合時，其水合作用中和表面有部份結合水分子所佔的比例和 BMVC 在雙股螺旋 DNA 中相較有顯著的增加。因此我們認爲在四股螺旋中 BMVC 是更加深埋在 DNA 分子之中。

Femtosecond fluorescence Dynamics of Organic Molecules and Organic Nanoparticles in Solutions

Student: Chih-Wei Chang Adviser:Eric Wei-Guang Diau

Institute of applied chemistry
Nation Chiao Tung University

Abstract

With the application of time-resolve fluorescence spectroscopy, Field Emission Scanning Electron Microscopy (FESEM), single crystal X-ray Diffraction (XRD) and powder XRD; the excited state dynamics and origin of the fluorescence enhancement of organic nanoparticle (1,4-di[(E)-2-phenyl-1-propenyl] benzene, PPB) and nanobelts((*Z*)-3-{4-[(*Z*)-2-cyano-2-phenyl-1-ethenyl] phenyl }-2-phenyl-2-propenenitrile, CNDSB) was investigated. Through the reprecipitation method, organic nanostructure of those two compounds was formed in water/ THF solution, and the size increases with the water percentage. The crystal structure of PPB nanoparticles and single crystal was also determined. For PPB nanoparicles, the origin of this fluorescence enhancement was contributed from both the conformational planarization, and the herringbone-type aggregate. The time-resolved fluorescence spectroscopy and powder XRD reveal that two different packing structures involved in the PPB nanoparticles. For CNDSB, the role of intramolecular motion was tested by measuring the time-resolved transient of CNDSB/PMMA film. The result reveals that the structure confinement only contributes parts of the fluorescence enhancement of the CNDSB nanobelts. In CNDSB nanobelts, a unique ultrafast energy transfer

process along the long axis of crystal was observed (~150 fs), which was absent in PPB nanoparticle.

For 3,6-bis(1-methyl-4-vinylpyridium) carbazole diiodide (BMVC) molecules, by comparing the time-resolved transient of BMVC in tris-HCl buffer and glycerol, the excited-state and solvation dynamics has been investigated. The results indicated that the rotational induced internal conversion and intersystem crossing process is an important nonradiative process for excited BMVC molecules. The solvation dynamics of BMVC in glycerol is significant decelerated due to the high viscosity of solvent. As BMVC interacted with linear duplex DNA (LD) and quadruplex DNA (Hum24), significant fluorescence enhancement was observed, which accompany with the hypsochromic shift of absorbance. The fluorescence enhancement was attributed to the specific interaction between BMVC and DNA macromolecule, which suppress the intramolecular motion of the molecules. The solvation dynamic of BMVC/LD and BMVC/Hum 24 complexes reveal that there are two types of water on DNA surface: bulk like and weakly bound water, and the solvation time is ~1 ps and ~9 ps, respectively. The result indicated that in BMVC/LD, BMVC is buried between the major and minor grooves. For BMVC/Hum 24, the fraction of the solvation caused by weakly bound water is increased, which indicated that BMVC is further buried into the DNA surface.

誌　　謝

時光荏然，剛進研究所的情景還歷歷在目，轉眼間已經到了撰寫誌謝的時刻，碩士班加上博士班一共六年的求學過程期間，經由許多人的幫助、支持與鼓勵，終於使我順利完成論文寫作及畢業，這些點點滴滴都讓我感激在心頭，藉此對你們致上我萬分的謝意。

首先感謝我的指導教授刁維光老師，在這六年期間諄諄不誨的教導，使我從中學習到從事學術研究的方法。

感謝論文口試委員:張大釗老師、鄭博元老師、胡景瀚老師以及吳東昆老師對於我論文上不足之處所給予的指證，使得論文能夠更加完備。

感謝佩珍在我論文撰寫時能耐著性子幫我看完初稿，並做修正的工作，這本論文的完成真的要大大感謝你的幫忙。

感謝這六年來陪我一路走來的夥伴們:陳建仲博士、盈志、立揚、載德、思成、佳珍、士勳、建源、思敏、鈺菁、睿勻、重光、清輝、嘉益、學沛、思帆、賢文。沒有你(妳)們，這段日子將會顯得黯然失色。

要感謝的是中壢西區扶輪社的先進們,以及中華扶輪教育基金會所提供的中華扶輪獎學金使我在論文撰寫的期間減少了許多經濟上的壓力，而能專心於論文上。

最後要感謝我的家人，給予我百分百的支持與實質的協助，讓我能專心唸書，無後顧之憂完成學業。

Table of contents

Table of Figures

Chapter 1 General Introduction

1.1 Luminescence

Luminescence is the ultraviolet, visible or infrared radiation emitted by the electronic excited molecule. There are two types of luminescence: fluorescence and phosphorescence, which is distinguished by the nature of the excited state. If the spin of the upper state and the lower state is the same (single-single or triplet-triplet), the radiatve transition occur between those two states is called fluorescence. On the other word, if spin of the upper and the lower state is different, the radiative transition occur between those two states is called phosphorescence. In most cases, the spin of the ground state is singlet, and the process of emitting a photon from singlet excited state to ground state is spin-allowed. The emission of fluorescence can occur rapidly, and the typical radiative lifetime is ranging from nanosecond (10^{-9}s) to microsecond (10^{-6}s) time scale. Once the molecule is excited, many other pathways like internal conversion, intersystem crossing, intramolecular conformational change and charge transfer….etc, will compete with the radiatve process. (Figure 1.1)

Therefore, the characteristic of fluorescence (spectrum, quantum yield, and lifetime) can provide us the information of the above-mentioned non-radiative process. In early years, because of the restriction of instruments, the fluorescence measurement was restricted on the steady state spectra, which can be thought as the average of the time-resolved spectra:

$$I_{ss} = \sum_{n=1}^{\infty} \int_{0}^{\infty} I_0 \times e^{-t/\tau_n} dt \qquad (1)$$

The multi-exponential decay reflects the processes that involved in the excited-state deactivation. However, much information about the molecules is lost during the time-averaging process. For that reason, to obtain the time-resolved fluorescence spectra become very important to investigate those non-radiative processes, and the time-resolved fluorescence technique will be introduced in the next section.

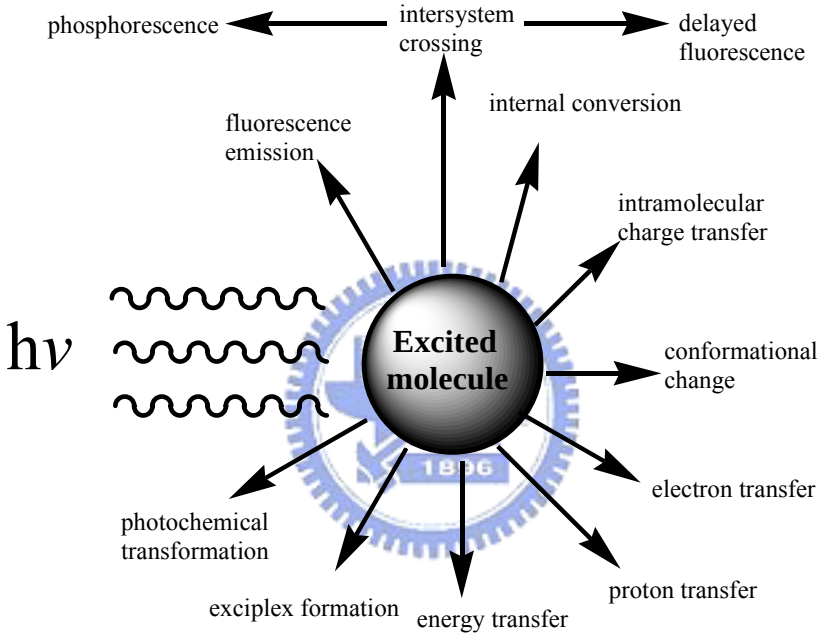

Figure 1.1: Possible non-radiative processes that compete with the fluorescence emission

1.2 Fluorescence lifetime

Fluorescence lifetime is the most important quantity for people who want to investigate the excited state dynamics by using time-resolved fluorescence spectroscopy. Since fluorescence is proportional to the excited state population of molecules, fluorescence lifetime can be defined as the reciprocal of the rate of depopulation of excited state molecules following optical excitation.[1] For radiative

[1] Lakowicz, J. R. *Topics in fluorescence spectroscopy vol. 1: Techniques*; Plenum Publishing

process, the decay of excited state population can be described with the following equation:

$$\frac{d\left[M^*\right]}{dt} = -\frac{\left[M^*\right]}{\tau_r} \tag{2}$$

In which, $[M^*]$ denotes the concentration of excited state molecules.

After integration, we obtain:

$$\left[M^*\right] = \left[M^*\right]_0 \times e^{-t/\tau_r} \tag{3}$$

Where $\left[M^*\right]_0$ indicates the excited state concentration at time-zero. Equation 3 describes the simplest case of fluorescence decay, in which all excited molecules return to the ground state via radiative process. In this case, τ_r is called the radiative lifetime of the molecule, and radiative rate constant k_r is the reciprocal of τ_r. However, in most cases non-radiative processes will compete with the radiative pathway, and the observed fluorescence lifetime τ_f is the reciprocal of the sum of k_r and nonradiative rate constant k_{nr}:

$$\tau_f = \frac{1}{k_r + k_{nr}} \tag{4}$$

In general, the fluorescence lifetime of the interesting molecule will be measured under various conditions (different excitation and probing wavelengths, viscosity, temperature, etc). The nature of the nonradiative process can be investigated by comparing the fluorescence transients under those conditions, and verify how k_{nr} changes with those parameters

1.3 Phase-modulation and pulse excitation method

The first nanosecond lifetime was measured by E. Gaviola in 1926 by using phase

---

Corporation: New York, 1991; Vol. 1.

modulation method.[2] In phase-modulation method, the sample was excited by intensity-modulated light. Usually, the excitation light is modulated with sin wave. Once the molecule was excited by modulated light, the intensity of fluorescence was forced to respond at the same modulation frequency. However, the phase of emitted fluorescence would be shifted, and the extent of modulation would be decreased due to the delay of the fluorescence emission.

An alternative method is pulse-excitation method, which is the most popular method at present. In pulse-excitation method (Figure. 1.2), the sample is excited with a short pulse. The time-dependent fluorescence transient is detected following optical excitation, and the decay time is calculated from the slope of plot intensity versus time. Usually fluorescence lifetime τ is defined as the time of the intensity decrease to 1/e of the value at time-zero.

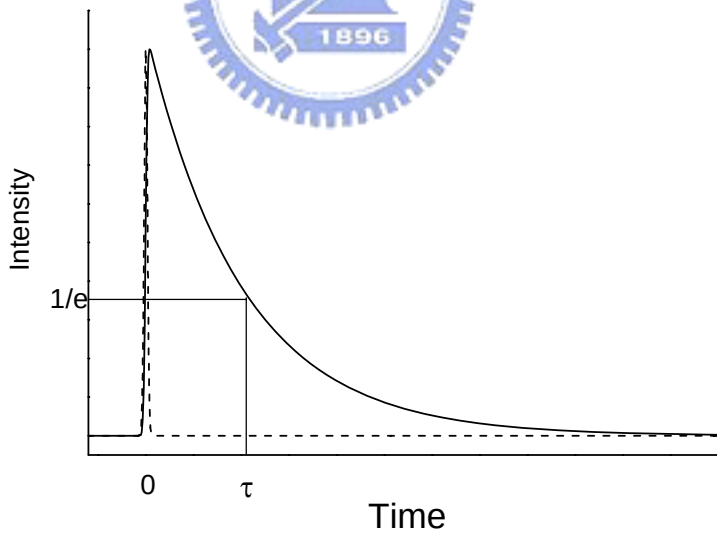

Figure 1.2: The principle of time-domain method for measuring fluorescence lifetime

1.4 Pulse excitation techniques

At present, time-correlated single photon counting (TCSPC) is widely used in

[2] Valeur, B. *Molecular fluorescence*; Weinheim; Wiley-VCH: New York, 2002.

time-domain lifetime measurement. This method was first developed by Bollinger and Thomas in 1961,[3] and the basic principle is that the probability of detecting a single photon at a delay time "t" is proportion to the fluorescence intensity at that time. Therefore, by histogramming the arrival time of individual photon over millions of excitation cycles, we can reconstruct the fluorescence decay profile. With the improvements of technology, the time resolution of TCSPC technique can reach tens of ps. Because of the importance of TCSPC method, the detail principle will be described in Chapter 2.

For the fluorescence decay within the range between picosecond to subpicosecond time scale, fluorescence up-conversion method has been widely used. The basic idea is to pass the fluorescence signal through a nonlinear crystal (LBO or BBO) and gated by another femto or picosecond light pulse.[4] Once phase-matching angle and optical delay between fluorescence and gate pulse are properly adjusted, the up-converted signal will appear. The wavelength of the up-converted signal can be calculated using the following equation:

$$\frac{1}{\lambda_{\text{signal}}} = \frac{1}{\lambda_{\text{fluorescence}}} + \frac{1}{\lambda_{\text{gate}}} \tag{5}$$

The time-resolved transient is obtained by measuring the intensity of up-converted signal as the delay time is changed. (Figure. 1.3) The superior time resolution (<150 fs, depending on the pulse duration) of this method makes the investigation of the ultrafast elementary molecular-relaxation processes become possible. However, this method is difficult to obtain the fluorescence in nanosecond timescale, because the

[3] Bollinger, L. M.; Thomas, G. E. *Rev. Sci. Instrum.* **1961**, *32*, 1044.
[4] Kahlow, M. A.; Jarzeba, W.; DuBruil, T. P.; Barbara, P. F. *Rev. Sci. Instrum.* **1988**, *59*, 1098.

delay line will become too long (1 ns is corresponding to 30 cm optical delay), and the alignment of the delay line will be too difficult to maintain as the time delay is changed.

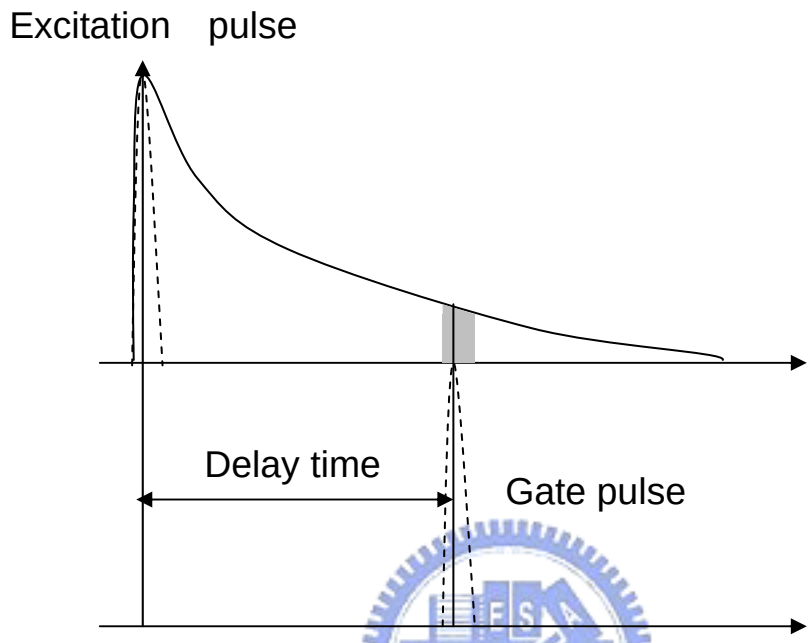

Figure 1.3: Scheme layout of the principle of fluorescence up-conversion

1.5 Summary

In summary, by using the above-mentioned time-resolved fluorescence spectroscopy, my works are focused on the excited-state dynamics of organic nanoparticles and 3,6-bis(1-methyl-4-vinylpyridinium) carbazole diiodide (BMVC), and I will give a brief introduction in the following paragraph.

In the past few years, organic nanostructures has became more and more important because of its large variety and the interesting properties.[5,6,7]. In many cases, the fluorescence property of organic molecules and its nanostructure are very

[5] Horn, D.; Rieger, J. *Angew. Chem. Int. Ed.* **2001**, *40*, 4330.
[6] Kasai, H.; Kamatani, H.; Okada, S.; Oikawa, H.; Matsuda, H.; Nakanishi, H. *Jpn. J. Appl. Phys.* **1996**, *35*, L221
[7] Yoshikava, H.; Masuhara, H. *J. Photochem. Photobiol., C* **2000**, 57.

different.[8,9,10,11] For 1,4-distyrylbenzene (DSB)[12] or DPST[13] , the formation of nanoparticles will decrease the fluorescence. However, for CN-MBE, the formation of the nanoparticle increases the fluorescence.[13] In order to understand the crucial factor in determining the fluorescence change of nanoparticles, we investigated the excited state dynamics of 1,4-di[(E)-2-phenyl-1-propenyl]benzene (PPB), and CNDSB. Chapter 3 is focused on PPB nanoparticles. In PPB, we observed the enhancement of the fluorescence due to the formation of nanoparticles. Our results reveal that the fluorescence enhancement is due to not only the geometry restriction of the molecules, but also the combined effects of the conformational planarization and the herringbone-type aggregate formation. In Chapter 4, I extend the work to CNDSB, which forms nanobelts in solution, and we also observe similar fluorescence enhancement due to the formation of nanostructures. However, a unique ultrafast energy transfer is observed in this case, which might be caused by the one-dimensional nanostructure of the nanobelts.

The second series of studies is about the 3,6-bis(1-methyl-4-vinylpyridinium) carbazole diiodide (BMVC), which can recognize the quadruplex structure of DNA. Recently, the interaction between telomerase and telomere has attracted lots of attention because of its importance in the abnormal overgrowth of cancer cells.[14,15,16]

---

[8] Onodera, T.; Kasai, H.; Okada, S.; Oikawa, H.; Mizuno, K.; Fujitsuka, M.; Ito, O.; Nakanishi, H. *Optical Materials* **2002**, *21*, 595.
[9] Oikawa, H.; Mitsui, T.; Onodera, T.;Kasai, H.; Nakanishi, H.; Sekiguchi, T. *Jpn. J. Appl. Phys.* **2003**, *42*, L111.
[10] Fu, H. B.; and Yao, J. N.; *J. Am. Chem. Soc.* **2001**, *123*, 1434.
[11] Fu, H. B.; Loo, B. H.; Xiao, D.; Xie, R.; Ji, X.; Yao, J.; Zhang, B.; Zhang, L. *Angew. Chem. Int. Ed.* **2002**, *41*, 962.
[12] Oelkrug, D.; Tompert, A.; Gierschner, J.; Egelhaaf, H.-J.; Hanack, M.; Hohloch, M.; Steinhuber, E. *J. Phys. Chem. B* **1998**, *102*, 1902.
[13] An, B.-K.; Kwon,S.-K.; Jung S.-D.; Park, S. Y. *J. Am. Chem. Soc.* **2002**, *124*, 14410.
[14] Greider, C. W. and Blackburn, E. H. *Cell* **1987**, *51*, 887.
[15] Feng, J., Funk, W. D., Wang, S.-S., Weinrich, S. L., Avilion, A. A., Chiu, C.-P., Adams, R. R., Chang,

some studies pointed out that the formation of quadruplex structure in telomere can inhibit the activity of telomerase,[17,18] and therefore the studies about the quadruplex structure DNA become more and more important. In 2003, Ta-Chau Chang's group synthesized a new carbazole dye: BMVC, which can be used to distinguish the duplex and quadruplex structure of DNA, and can be used to label the cancer cell. [19] According to their result, the fluorescence of BMVC is weak in tris-buffer.[19] However, as BMVC interacted with liner duplex (LD) and quadruplex (Hum24) DNA, they observed a dramatic enhancement of the fluorescence. The emission spectrum of BMVC/LD and BMVC/Hum24 is central at ~560 nm and ~580 nm, respectively. Therefore it can be used to recognize the quadruplex structure of DNA. However, the information about the excited state dynamics of BMVC is still absent. In Chapter 5, the excited state dynamics of BMVC in tris-buffer and glycerol is reported. By comparing the fluorescence transient of BMVC in tris-buffer and glycerol, we found that both rotational induced internal conversion and vibrational relaxation process are involved in the excited-state dynamics of the molecules. In glycerol, because of the high viscosity of glycerol, the intramolecular motion is suppressed, therefore we observed the increase of fluorescence. By reconstructing the time-resolved emission spectra, the environment sensitivity of the solvation dynamics were tested in tris-buffer and glycerol, and the results indicated that it is sensitive to the local

---

E., Allsopp, R. C., Yu, J., Le, S., West, M. D., Harley, C. B., Andrews, W. H., Greider, C. W. and Villeponteau, B. *Science* **1995**, *269*, 1236.

[16] Hahn, W. C., Counter, C. M., Lundberg, A. S., L., B. R., Brooks, M. W. and Weinberg, R. A. *Nature* **1999**, *400*, 464.

[17] Zahler, A. M., Williamson, J. R., Cech, T. R. and Prescott, D. M. *Nature* **1991**, *350*, 718.

[18] Neidle, S. and Parkinson, G. N. *Nat. Rev. Drug Discovery* **2003**, *1*, 383.

[19] Chang, C.-C., Kuo, I.-C., Ling, I.-F., Chen, C.-T., Chen, H.-C., Lou, P.-J., Lin, J.-J. and Chang, T.-C. *Anal. Chem.* **2004**, *76*, 4490.

environment. In Chapter 6, we focused on the interaction between BMVC and DNA in BMVC/DNA (LD or Hum24) complexes. When BMVC interacted with linear duplex DNA (LD) or quadruplex DNA (Hum24), the fluorescence intensity and lifetime increase dramatically. The results indicated that the interaction between BMVC and DNA molecule can suppress the intramolecular motion of the molecule. The solvation dynamics reveals that for BMVC in LD and Hum24, the solvation process is contributed from both bulk like water and weakly bound water. The relative amplitude of the salvation caused by those two kinds of water is different in LD and Hum24. It can be used as the alternative method to obtain the information about the bind site of BMVC in LD and Hum24 DNA.

Chapter 2 Experimental setup

2.1 Introduction

Laser is an optical oscillator, which creates a highly directional beam of light at narrow wavelength. Figure 2.1 is the diagram of a simple laser cavity. Generally, there are three important components of lasers.

1: High reflector

2: Gain medium

3: Output coupler / partial reflector

The length L between high reflector and output coupler is the length of laser cavity. When the gain medium is excited and reaching population inversion, the light passing through the gain medium will be amplified.

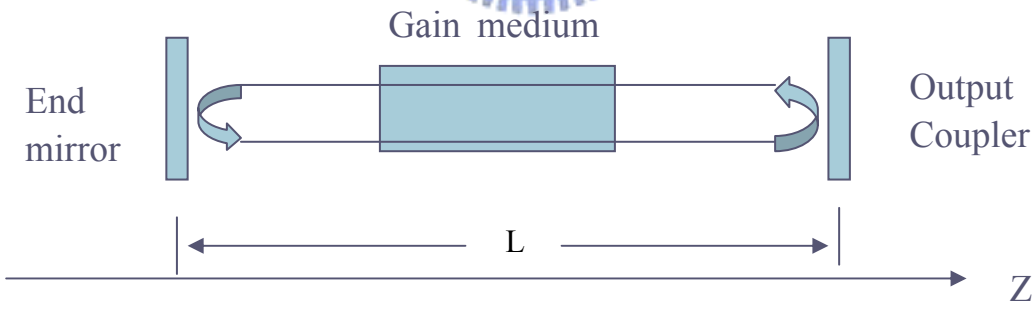

Figure 2.1: The scheme diagram of a simple laser cavity

2.2 Ultrashort pulse formation: principle of mode locking

In principle, because of the requirement of resonance condition, only the wavelengths satisfy the condition that the cavity length is the integral number of the half wavelength can survive in laser cavity, which means:

$2L = q\lambda_q$ q :any positive integral number

$$\Rightarrow \lambda_q = \frac{2L}{q},\quad \upsilon_q = \frac{C}{\lambda_q} = q\left(\frac{C}{2L}\right) \qquad C : \text{the speed of light} \tag{1}$$

and the mode space $\delta\upsilon = \frac{C}{2L}$.

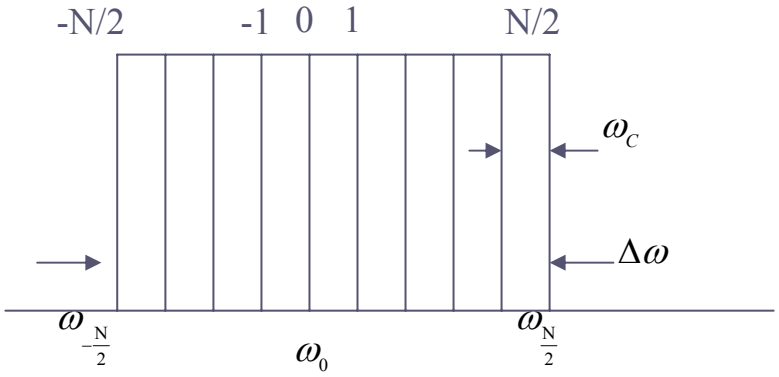

Figure 2.2: The imaginary rectangular spectra in laser cavity.

In Figure 2.2, we assume a rectangular form spectrum in laser cavity and the electric field of each cavity mode can represent as the following equation:

$$E_n(t,z) = E_0 e^{i(\omega_n t - k_n Z + \phi_n)} \tag{2}$$

In which ω, k, and ϕ denote the angular frequency, the wave vector, and the initial phase of the cavity mode, respectively. At Z=0, the superposition of all cavity modes is:

$$E(t) = E_0 \sum_{n=-\frac{N}{2}}^{n=\frac{N}{2}} e^{i(\omega_n t + \phi_n)} = E_0 \sum_{n=-\frac{N}{2}}^{n=\frac{N}{2}} e^{i[(\omega_0 + n\omega_C)t + \phi_n]} \tag{3}$$

If the initial phase of all cavity modes are the same ($\varphi_n = \varphi_0 \equiv$ constant), equation (3) can be further reduced:

$$E(t) = E_0 e^{i(\omega_0 t + \phi_0)} \sum_{n=-\frac{N}{2}}^{\frac{N}{2}} e^{in\omega_c t} \tag{4}$$

Due to $e^{i\theta} = \cos\theta + i\sin\theta$ (Euler formula), we only focus on the real number part of the equation, and equation (4) can be rearranged:

$$E(t) = E_0 e^{i(\omega_0 t+\phi_0)}(1+2\sum_{n=1}^{\frac{N}{2}}\cos n\omega_c t) = E_0\left[\frac{\sin\left(\frac{N+1}{2}\right)\omega_c t}{\sin\frac{\omega_c t}{2}}\right] * e^{i(\omega_0 t+\phi_0)} \quad (5)$$

We obtained

$$E(t) = A(t)\times e^{i(\omega_0 t+\phi_0)}, \quad A(t) = E_0\left(\frac{\sin\left(\frac{N+1}{2}\omega_c t\right)}{\sin(\frac{\omega_c t}{2})}\right) \quad (6)$$

Because the intensity of laser I(t) is proportion to $E(t)\times E^*(t)$, I(t) can be represented by equation (7):

$$I(t) \propto E(t)\times E^*(t) = A(t)^2 = {E_0}^2\left[\frac{\sin^2\left(\frac{N+1}{2}\omega_c t\right)}{\sin^2(\frac{\omega_c t}{2})}\right] \quad (7)$$

The plot of I(t) for N=4 is shown in Figure 2.3

From the above equation, I(t) would be the maximum value when $\frac{1}{2}\omega_c t = m\pi$, while the time interval between pulses $t_m = \frac{2m\pi}{\omega_c}$. Therefore, we obtained:

$$\Delta t = t_{m+1} - t_m = \frac{2\pi}{\omega_c} = \frac{1}{\delta\upsilon} = \frac{2L}{C} \quad (8)$$

The time interval between two pulses is equal to the time of pulse traveling in the laser cavity, which is called the round-trip time.

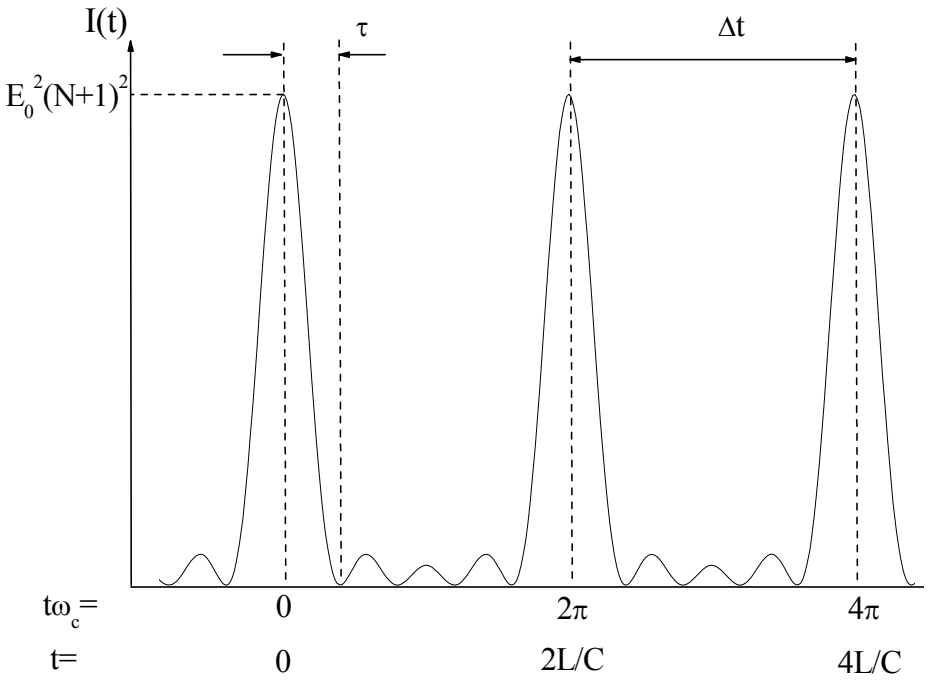

Figure 2.3: The illustration of the laser intensity change versus time for N=4.

From equation 7, the maximum intensity also can be estimated:

$$I(t)_{max} = \lim_{\frac{1}{2}\omega_c t \to 0} E_0^2 \frac{\sin^2\left(\frac{N+1}{2}\omega_c t\right)}{\sin^2\left(\frac{1}{2}\omega_c t\right)} \approx E_0^2 \frac{\left(\frac{N+1}{2}\omega_c t\right)^2}{\left(\frac{1}{2}\omega_c t\right)^2} = E_0^2 (N+1)^2 \qquad (9)$$

The pulse width $\tau = \frac{1}{N+1}\left(\frac{2L}{C}\right)$ (10)

The bandwidth $\Delta\nu = N\delta\nu = N\left(\frac{C}{2L}\right)$ (11)

If we multiply those two quantities, we obtained:

$$\tau\,\delta\nu = \frac{N}{N+1} \approx 1 \text{ (for } N >> 1) \qquad (12)$$

The units of τ and ν are second and Hz, respectively. The time-bandwidth product indicated that enough bandwidth is essential to produce an ultrashort pulse. For various pulse shapes, the time-bandwidth product are different (ex: for Gaussian shape pulses, $\tau\,\delta\nu = 0.441$), and only pulses that have their frequency components all

locked in phase obey this relationship. If the pulse obeys this relationship it is called a transform-limited pulse.

2.3 Active mode-locking and passive mode-locking

From the above derivation, we know that for mode-locked laser, the output will become pulsed, and the repetition rate is equal to the round-trip time, which is determined by the length of laser cavity. If we want to produce a mode-locked laser, we need to place an ultrafast shutter (the repetition rate is equal to $\frac{C}{2L}$, C: the speed of light), and the opening time must be synchronized to the mode-locked pulse. For a typical mode-locked laser, the cavity length is about 150 cm, which corresponds to ~10 ns round-trip time, and no mechanical chopper can afford this speed. Hence, a special designed mechanism is required, and there are two types of mode-locking mechanisms.

— *Active mode-locking*: this method needs an external modulation at specific frequency, and the target of the modulation can be either the gain of amplifying medium or the cavity loss.

— *Passive mode-locking*: No external modulation is required. It results from the insertion of a saturable absorber into the cavity or the optical Kerr effect of optical components, which can automatically select the mode-locked pulse.

The femtosecond Ti:sapphire laser in our laboratory is using optical Kerr effect to achieve the mode-locking condition. In normal case, the refractive index "n" of a material obeys the following relationship:

$$n = n_0 + \frac{1}{2} n_2 I \qquad (13)$$

In which, n_0 is the intrinsic refractive index of material, n_2 (positive) is the nonlinear coefficient of the refractive index, and I is the intensity of the laser. In general, n_2 is a very small value, and the second term can be ignored. However, if the intensity is high enough and the alternation caused by n_2 cannot be ignored, this effect is called optical Kerr effect.

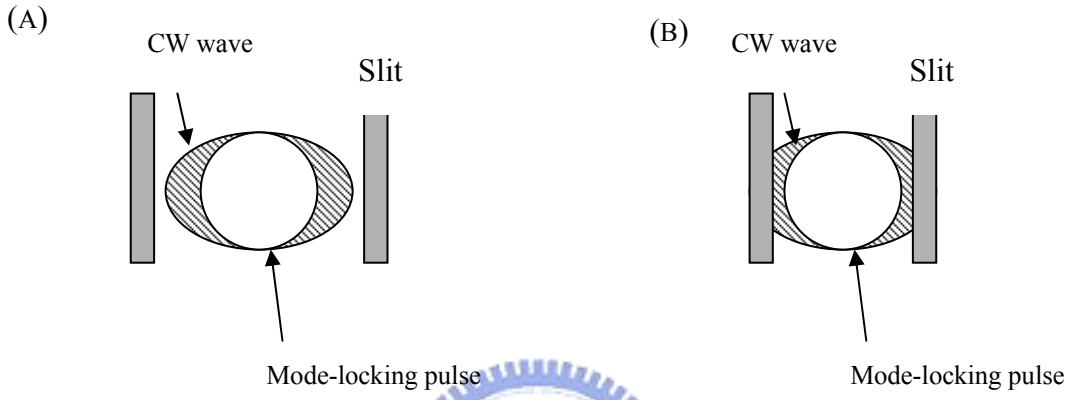

Figure 2.4: The scheme diagram for cross-sectional view of CW wave and a mode-locked pulse. (A) Slit is open; the loss of a CW wave and a mode-locked pulse is the same. (B) Slit is closed; the loss of a CW wave increases, and only the mode-locked pulse can survive

For TEM00 mode, the intensity distribution is bell shape (Gaussian) across the laser beam. Since the beam is less intense at its edge, the refractive index at the center will larger than at the edge. This causes the light to bend toward the center, and functions like a lens. In Figure 2.4A, the optical Kerr effect is more significant for mode-locked pulse than for continue wave because of its high intensity. If we place a slit, and the width is properly adjusted (Figure 2.4 B), the cavity loss of the continue wave will increase, and only the mode-locked pulse can survive and amplify in laser cavity.

2.4 Birefringent filter

For mode-locked Ti:sapphire laser, another important issue is the wavelength tuning element. In our system, the wavelength tuning is achieved by using birefringent filter, and the principle will be introduced in this paragraph.

The light enters the crystal at an arbitrary angle can be break up into two separate components that perpendicular to each other. The component on the plane, which containing the propagation direction ($\vec{k}$) and the optical axis ($\overrightarrow{OA}$), is called the extraordinary wave (e-ray). Another component, which is perpendicular to the e-ray, is called the ordinary wave (o-ray). In principle, the refractive index of o-ray (n_o) is a constant, and the refractive index of e-ray (n_e) changes with the angle between the direction of light propagate ($\vec{k}$) and the optical axis of the crystal ($\overrightarrow{OA}$). Because e-ray and o-ray have different refractive index and travel at different speed of light in the crystal, the phase shift ($\Delta\phi$) induced by this optical anisotropy effect can be calculated:

$$\Delta\phi = \frac{2\pi}{\lambda}(n_e - n_o)d \tag{14}$$

In which, d is the thickness of crystal. Only when the phase is equal to $2m\pi$ (m is an integral), the wave can survive. Therefore, we obtained:

$$2m\pi = \frac{2\pi}{\lambda}(n_e - n_o)d$$

$$\lambda = \frac{(n_e - n_o)d}{m} \tag{15}$$

Since n_e changes with the angle between $\vec{k}$ and $\overrightarrow{OA}$, the wavelength tuning can be achieved by rotating the birefringent filter.

2.5 Femtosecond Ti:sapphire laser: Mira 900-D

The femtosecond light source used in our lab is Coherent Mira Model 900-D laser. (Coherent, Inc.) Mira 900-D uses Ti:sapphire as the gain medium and is tunable from 700 to 1000 nm. The oscillator is pumped by a solid state diode-pumped frequency-doubled Nd:YVO_4 laser (Verdi^{TM} V-10, Coherent), which the output wavelength is 532 nm and the averaged power is 10 W. The optical path of the oscillator is shown in Figure 2.5. Pumping beam is focused on Ti:sapphire crystal by lens L1. M7 is the flat end mirror and M1 serves as the output coupler of laser cavity. Two prisms BP1 and BP2 are used to compensate the group velocity dispersion of the femtosecond pulse. A birefringent filter selects the wavelength of the laser output. By using optical Kerr effect, the laser cavity has been designed so that the diameter of the mode locked beam is slightly small than the non-mode locked beam. Therefore we can select the mode locked pulse with the application of a simple slit. The repetition rate is 76 MHz, and the pulse width is ~150 fs (FWHM of autocorrelation).

2.6 Autocorrelator (Mini, Inrad)

The characterization of the temporal profile of laser pulse is an important issue for time-resolved spectroscopy measurement. The response time of the electric components is limited from tens of ps (photodiode) to ps (streak camera). Therefore, for the pulse generated by the mode-locked Ti:sapphire laser, we used autocorrelation techniques to measure the pulse width. Figure. 2.6 is the optical layout of autocorrelator.

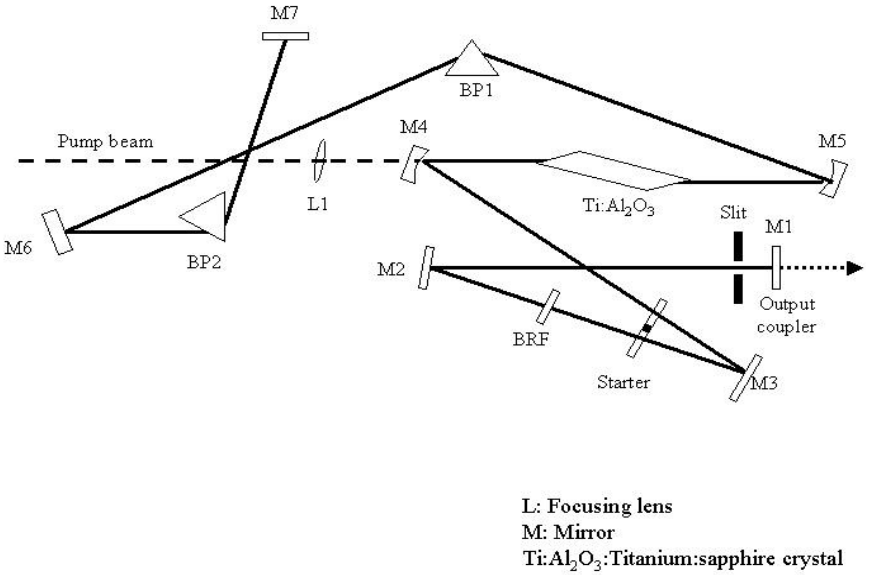

Figure 2.5: The optical scheme for Coherent Mira-900 D oscillator.

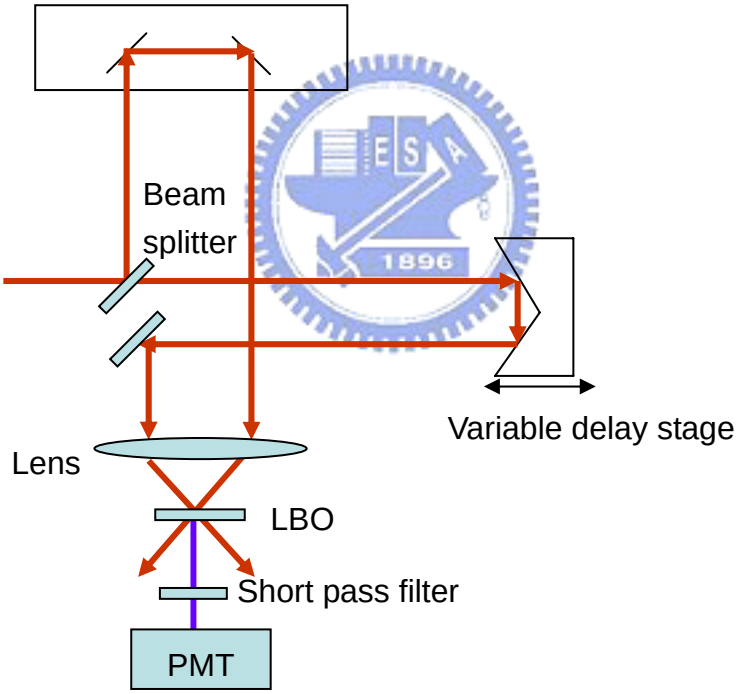

Figure 2.6: The optical layout of femtosecond autocorrelator

A beam splitter separates input pulse. The two beams are focused and overlapped on a LBO crystal. Once the delay time and the phase matching angle of those two beams are properly adjusted, the second harmonic signal will be generated and detected by PMT. The optical delay of those two beams is controlled by a

computer-controlled stage. Scanning back and forth the delay stage and monitoring the intensity change of the second harmonic signal can obtain the autocorrelation trace. For a Gaussian pulse, the FWHM of the autocorrelation trace is $\sqrt{2}$ times the FWHM of laser pulse.

2.7 Fluorescence optically gated system

Femtosecond temporally resolved spectra were obtained with an fluorescence optically gated system (FOG100, CDP) in combination with a mode locked Ti:sapphire laser (Coherent, Mira 900D). A schematic depiction is shown in Figure 2.7 The femtosecond laser system generates output pulses of duration ~150 fs (FWHM of autocorrelation) with 76 MHz repetition rate. The spectral bandwidth is 10~12 nm and the wavelength is tunable from 700 to 1000 nm. The frequency of the laser pulse is doubled by a BBO type-I crystal to generate the second harmonic signal ranging from 350~500 nm and used as excitation (pump); the residual fundamental pulse is used as a probe beam and split from the pump beam with two dichroic beam splitters (BS1, BS2). A berek polarization compensator (B) controls the polarization of the pump beam; for fluorescence lifetime measurement the relative polarization between pump and probe beams is fixed at 54.7^{o} (magic angle). The intensity of the excitation beam is properly attenuated and focused onto a rotating sample cell (S). Fluorescence is collected with two parabolic mirrors and focused onto another BBO type-I crystal (NC, thickness 0.5 mm). The gate pulse (probe) also focuses on NC for sum-frequency generation (SFG). The delay time between gate pulse and fluorescence is controlled by a stepping translational stage (maximum delay 2.0 ns, minimum step

size 6.25 fs). The SFG signal is collected by a lens (L4) and separated from the interference (pump or gate pulse) by the combination of an iris (A), a band-pass filter (F3) and a double monochromator. The signal is detected by a photomultiplier (Hamamatsu, R1527P), which is in turn connected to a computer-controlled photon-counting system.

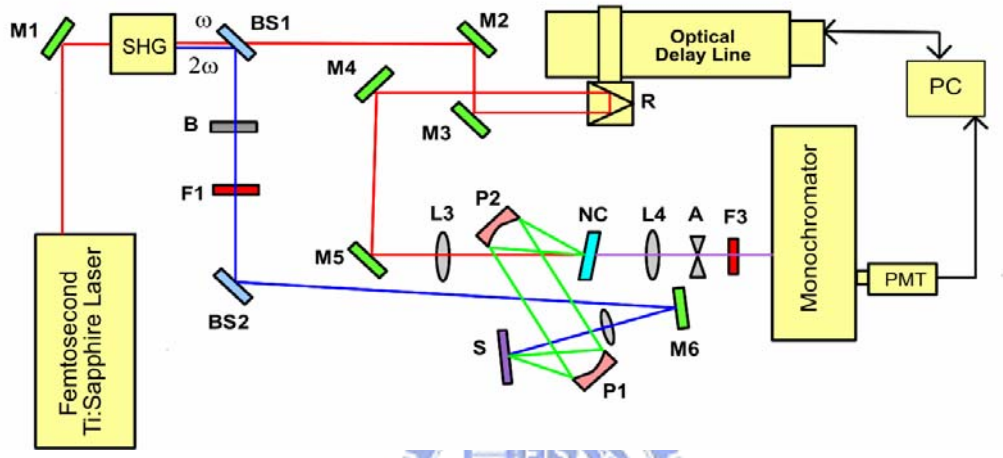

Figure 2.7 :The optical scheme for femtosecond fluorescence optical gated system. M1~M7: dielectric mirror (700~1000 nm), BS:dichroic beamsplitter, B:berck polarization compensator, P1 and P2:parabolic mirror, S: rotating sample cell.

2.8 Time-Correlated Single Photon Counting (TCSPC) system

The time-correlated single photon counting (TCSPC) system in our laboratory was purchased from PicoQuant GmbH, and the optical layout is shown in Figure 2.8. Excitation light source is introduced into the sample chamber by a reflective mirror, and an iris controls the intensity. The excitation laser is focused onto the sample holder by a focusing lens. The fluorescence is collected by high numerical aperture UV grade lens, and the distance between lens and sample cell can be adjusted by the handle ring outside the sample chamber. The collimated fluorescence then passes through an adjustable iris, and an adjustable polarizer controls the polarization. The

wavelength of the fluorescence is selected by a double subtractive monochromator (Sciencetech 9030DS). In double subtractive monochromator, the two gratings operate in a subtractive dispersion mode, which can remove the temporal and angular dispersions of the fluorescence. The silt, which locates at the center of the two monochromators, controls the spectral resolution, and the resolution is 8 nm with a 1-mm slit. Finally, the collecting signal is detected by a single photon sensitive detector (Photomultiplier, PMT), which is connected to a computer with a TCSPC-module (SPC-630, Becker and Hickl) card for data acquisition.

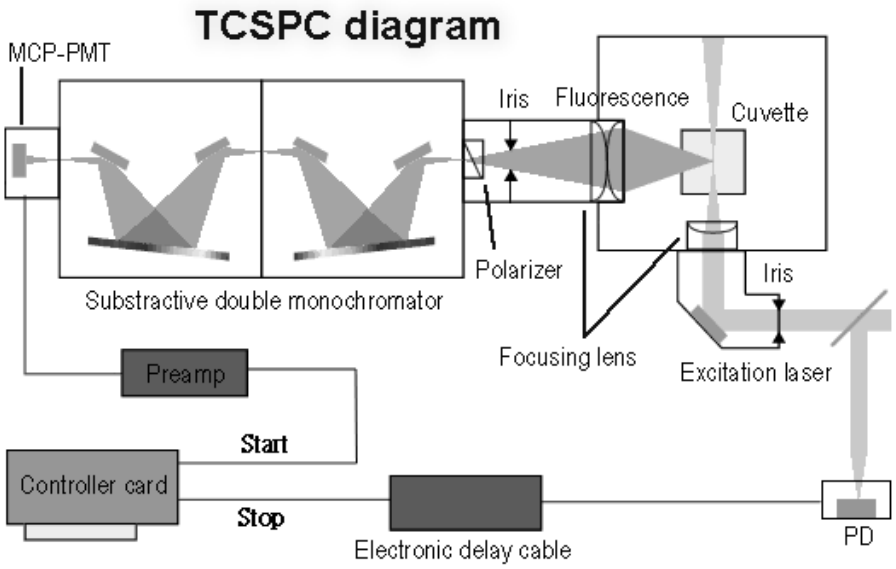

Figure 2.8: The optical layout of TCSPC system

Figure 2.9 is a scheme for the data acquisition and timing procedure of the TCSPC module. The fluorescence signal is monitored by a photon counting PMT. A constant fractional discriminator (CFD) is used to determine the exact arriving time of the photon. Simultaneously, the synchronal trigger signal of the excitation laser is sent to another CFD and used as the reference. The signal of CFD is sent to time to amplitude converter (TAC), which converts the delay time between fluorescence and the

synchronized trigger signal into voltage. The output voltage is sent to analog to digital converter (ADC) and addresses to corresponding time channel. Finally, the signal from ADC is sent to multi-channel analyzer (MCA) and the fluorescence decay is reconstructed after accumulating millions of signal. The detail description of each component will be shown in the following paragraph.

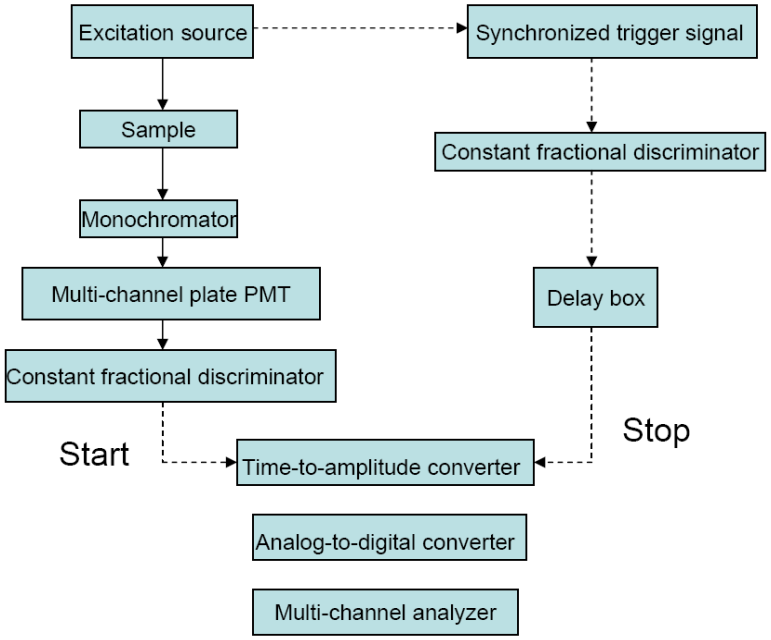

Figure 2.9: Data acquisition and timing diagram of TCSPC module

2.8.1 Double subtractive monochromator

For a monochromator used in pico or femto-second time resolved experiment, the temporal dispersion of the light with different wavelengths is not able to neglect anymore. To solve this problem, a double subtractive monochromator (Sciencetech Model 9030) was used to compensate the temporal dispersion. The first monochromator is used to select a band pass, and the variation of the optical path in different wavelength lights is removed by second monochromator. The spectral

dispersion is selected by using interchangeable slits with 0.5, 1.0, 2.0 mm, and the corresponding spectral resolution is 4, 8, and 16 nm, respectively.

2.8.2 Constant fractional discriminator (CFD)

Constant fractional discriminator is used to determine the arriving time of photon and synchronized signal. Figure 2.10 is the illustration of the principle of CFD; a part of input pulse is inverted and delayed with constant delay time. The sum of input pulse and inverted pulse generates a zero-crossing point as we can see in Figure 2.10. Since the temporal position of the crossover point is independent of the pulse amplitude, the time jitter caused by the amplitude fluctuation of the detector pulses can be eliminated by this method. On the other word, the CFD also contains a window discriminator which can reject the signal smaller or outside of the selected amplitude interval. By adjusting this interval, the noise from the environment can be effectively rejected.

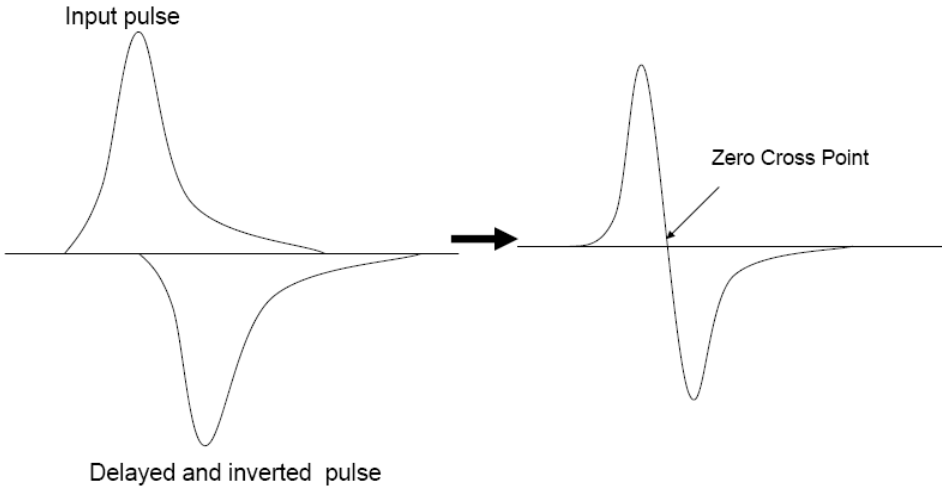

Figure 2.10: Basic function of CFD, a small portion of the input signal is inverted, and the arriving time is determined by the zero cross point.

2.8.3 Time-to-amplitude converter (TAC)

The time-to-amplitude converter is used to determine the delay time between detected photon and sync signal. When TAC receives the fluorescence pulse signal form CFD, it generates a linear ramping voltage and stop by the sync pulse train. The output voltage of TAC depends linearly on the time interval between photon and sync pulse. In contrast to tradition start-stop method, which starts from a sync pulse and stops at the fluorescence signal, this ‘reversed start-stop‘ method reduces the speed requirements of TAC, because its working cycle is performed with the photon detection rate instead of the considerable higher pulse repetition rate.

If the fluorescence intensity is too high, more than one photon will come to TAC within one excitation period. At this time, TAC starts to charge as the first photon arrives, and the second photon is neglected. Because only the first arriving photon is counted, the fluorescence lifetime obtained in this condition is shorter than the actual value, and this phenomenon is called “multi-photons pile up”. To avoid the pile up, the repetition rate of the detected photon is controlled lower than 1/100 of the repetition rate of excitation source.

2.8.4 Analog-to-digital converter (ADC)

The analog-to-digital converter converts TAC signal into the address of the memory. The ADC must have very high accuracy; because it has to resolve TAC signals into 4096 time channels, and the width of particular channel is only ~0.024% of the total voltage amplitude.

2.8.5 Multi-channel analyzer (MCA)

After the output voltage of TAC converts into the address of the memory, the data are saved in memory. After accumulating billions of photons, the fluorescence decay is reconstructed.

2.8.6 Variable delay box

The variable delay box is composed of coaxial cables, and no power is required to operate this component. The main purpose of this box is to delay the SYNC pulses so that they reach the TAC after the start pulse within the selected time range of interest. It provides a variable delay input signal from 0~63 ns.

2.8.7 Microchannel-plate photomultiplier Tube (MCP PMT)

MCP PMT includes anode (generates the photoelectron), microchannel plate (formed by capillary), and the cathode (receives the amplified photoelectron). When a high voltage is applied in anode and cathode, the photoelectron emitted from the anode will be collected and send into the capillary. The diameter of capillary is about 10 μm, and one layer of amplification media is coated on the inside wall of capillary. The cathode detects the amplified signal. Because this single photon detector is highly sensitive, and even dimmed ambient light can permanently damage it, there is a built-in shutter that interlocked with the chamber lid to prevent any damage caused by accident.

Chapter 3 Relaxation Dynamics of PPB nanoparticles

3.1 Introduction

Organic nanoparticles have attracted tremendous research interests over the past few years, owing to their special properties which lie between the properties of free molecules and those of bulk materials.[1] The electronic properties in organic nanoparticles are different from those of the inorganic ones[2] because of the weak intermolecular interaction forces of the van der waals type or the hydrogen bond.[3] However, organic nanocrystals are expected to be useful as novel functional materials in electronics and photonics, because of their variability and flexibility in synthesizing materials, preparing nanoparticles, and investigating their physicochemical properties such as luminescence[4] or high nonlinear optical efficiency.[5] In the other words, the size-dependent absorption and emission is also an interesting topic for the fundamental research.[6] Nakanishi and co-workers first initiated the investigation on this topic, they focused on nanocrystal fabrications and characterizations for perylene[6a-c] and many other organic systems.[6e,f] Recent investigations on the

[1] Horn, D.; Rieger, J. *Angew. Chem. Int. Ed.* **2001**, *40*, 4330.
[2] (a)Forrest, S. *MRS Bull.* **2001**, *26*, 108. (b)Alivistos., A. P. *Science* **1996**, *271*, 933.(c)Peng, X. G. *J. Am. Chem. Soc.* **1997**, *119*, 7019.
[3] Silinsh, E. A. *Organic Molecular Crystals: Their Electronic States*; Springer-Verlag: Berlin, 1980
[4] Yoshikava, H.; Masuhara, H. *J. Photochem. Photobiol. C* **2000**, 1, 57.
[5] (a)Chemla, D. S.; Zyss, J. *Nonlinear Optical Properties of Organic Molecules and Crystals*; Academic Press: Orlando, 1987; vol 1 (b)Gehr, R. J.; Boyd, R. W. *Chem. Mater.* **1996**, *8*, 1807.
[6] (a)Kasai, H.; Kamatani, H.; Okada, S.; Oikawa, H.; Matsuda, H.; Nakanishi, H. *Jpn. J. Appl. Phys.* **1996**, *35*, L221.(b)Onodera, T.; Kasai, H., Okada, S.;Oikawa, H.; Mizuno, K.; Fujitsuka, M.; Ito, O.; Nakanishi, H. *Optical Materials* **2002**, *21*, 595. (c)Oikawa, H.; Mitsui, T.; Onodera, T.; Kasai, H.; Nakanishi, H.; Sekiguchi, T. *Jpn. J. Appl. Phys.* **2003**, *42*, L111. (d)Katagi, H.; Kasai, H.; Okada, S.; Oikawa, H.; Komatsu, K.; Matsuda, H.; Liu, Z.; Nakanishi, H. *Jpn. J. Appl. Phys.* **1996**, *35*, L1364. (e) Baba, K.; Kasai, H.; Okada, S.; Oikawa, H.; Nakanishi, H. *Optical Materials* **2002**, *21*, 591. (f) Takahashi, H.; Miura, H.; Kasai, H.; Okada, S.; Oikawa, H.; Nakanishi, H. *J. Am. Chem. Soc.* **2002**, *124*, 10944.

nanoparticles of the pyrazoline derivatives[7] indicate that the emission color is affected by the particle sizes or the excitation wavelengths. Moreover, enhanced emissions due to aggregation have been reported for the organic systems of 1-cyano-trans-1,2-bis-(4¢-methylbiphenyl)ethylene (CN-MBE).[8]

In the present study, we collaborate with Prof. Chain-Shu Hsu for the synthesizing of 1,4-di[(E)-2-phenyl-1-propenyl]benzene (PPB, the structure is shown in scheme 1). This compound belongs to the family of phenylenevinylenes (PV) with two methyl groups added to 1,4-distyrylbenzene (DSB) skeleton. It is observed that the fluorescent emission from PPB nanoparticles is extremely strong, but PPB itself is non-fluorescent in dilute solution, which is similar to the feature observed in CN-MBE.[8] In contrast, free DSB in solution is highly fluorescent, but its nanoparticle shows low-emission feature.

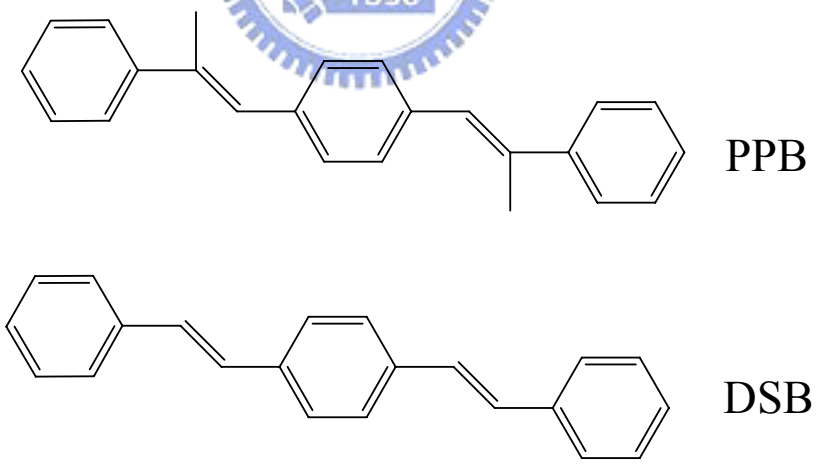

Scheme1: Chemical structures of PPB and DSB

In order to gain better understanding for this unusual phenomenon, we have

[7] (a)Fu, H. B.; Yao, J. N. *J. Am. Chem. Soc.* **2001**, *123*, 1434. (b)Fu, H. B.; Loo, B. H.; Xiao, D.; Xie, R.; Ji, X.; Yao, J.; Zhang, B.; Zhang, L.*Angew. Chem. Int. Ed.* **2002**, *41*, 962. (c) Xiao, D.; Xi, L.; Yang, W.; Fu, H.; Shuai, Z.; Fang, Y.; Yao. J. *J. Am. Chem. Soc.* **2003**, *125*, 6740.
[8] An, B.-K.; Kwon, S.-K.; Jung, S.-D.; Park, S.-Y. *J. Am. Chem. Soc.* **2002**, *124*, 14410.

investigated the excited-state relaxation dynamics and undertaken structural identification for free molecule and nanoparticles using the techniques of Field Emission Scanning Electron Microscopy (SEM), femtosecond (fs) and picosecond (ps) time-resolved fluorescence spectroscopy, and powder and single-crystal X-ray diffractions (XRD). The nanostructure samples are prepared according to the reprecipitation method in water/THF solutions. As water volume fraction exceeds 65 %, the nanoparticle of PPB starts to appear in solution. For PPB nanoparticles, two emissive states were observed in fluorescence transients and confirmed by the powder XRD measurements with two different packing structures. Fs fluorescence dynamics measurements have shown the significance of molecular geometry that affected the relaxation dynamics in the excited state of free molecule: efficient isomerization deactivation in PPB was observed, and the twisted nature of the geometry accelerated the rotational non-radiative process. In combination with the versatile results obtained in this study, we conclude that the enhanced emissions in PPB nanoparticles reflects the geometrical change from the twisted conformation to the nearly planar one in order to form the herringbone-type aggregation of nanoparticles, which is shown in the single crystal structure of PPB.

3.2 Experimental Section

Materials. The synthesis of PPB molecules was described elsewhere.[9] PPB was synthesized by Heck coupling.[10] A mixture of α-methylstyrene (2.5 g, 25.4 mmol), 1, 4-dibromobenzene (2.0 g, 8.4 mmol), palladium (II) acetate (0.037 g, 0.16 mmol), tris-(*ortho*-tolylphosphine) (0.102 g, 0.33 mmol) and triethylamine (4.92 g, 48.78 mmol) was prepared in thick-walled screw capped glass tube. The tube was capped under argon and heated overnight at 120°C. After cooling, the mixture was extracted with ethyl acetate, and the organic layer was washed with saturated NaCl and water by turns. It was dried with $MgSO_4$ and filtered, and then crude solid was recrystallized from hexane to get fine transparent crystals (yield: 65%).

Formation of Nanoparticles. The PPB nanoparticles were prepared by a simple reprecipitation method. Water and THF was used as a non-solvent and solvent, respectively. Volume fractions of water were controlled from 0 through 80%, with vigorous stirring at room temperature. In all solutions, the concentration of the chromophore (2.9×10^{-5} M) was constant after adding distilled water. After 65% volume fraction of water addition, PPB in mixture solution started to aggregate into nanosize particles. Nanoparticles' suspensions were homogenous and stable even after four months. Colloid sample for powder and SEM studies were prepared by the following procedures: the sample was first dispersed in THF and then dropped on a glass substrate (for powder XRD) or a carbon tape (for SEM) until it dried. The

[9] Bhongale, C. J.; Chang, C.-W.; Lee, C.-S. and Diau, E. W.-G. *J. Phys. Chem. B* **2005**, *109*, 13472-13478.

[10] Dieck, H. A.; Heck, R. F. *J. Am. Chem. Soc.* **1974**, *96*, 1133.

drop-dry process was preformed several times in order to deposit enough colloid samples.

X-ray Crystallography. (a) Powder XRD Collections. X-ray powder diffraction data were collected using a Bruker D8 diffractometer with Bragg-Brentano geometry (40 kV, 40 mA), Cu Kα radiation (λ= 1.5406 Å), and a 40 mm Göbel mirror. For a bulk sample, the powder pattern was scanned over the angular range 5-60° (2θ) with a step length of 0.1° and a counting time of 4 s per step. For a colloid sample (bulk and 65-80% solutions), the pattern was scanned over the angular range 5~16° (2θ), with a step length of 0.02° (2θ) and a counting time of 10 s per step. The measurements were carried out at room temperature. **(b) Single-crystal XRD Collections.** Single crystal suitable for the X-ray diffraction study was prepared from the slow evaporation of PPB in THF solution. A crystal with an average cubic shape (0.1×0.1×0.1 mm) is selected under an optical microscope, glued on glass fibers, and then mounted on an Enraf-Nonius CAD4 diffractometer using Mo Kα radiation (λ = 0.71073 Å) and ω-2θ scan mode. The SEARCH procedures were carried out for orientation matrix determination and peak indexing on the basis of 25 observed reflections. An orthorhombic cell was initially found a = 6.30(2) Å, b = 7.56(2) Å, c = 36.7(7) Å, V = 1750(3) $Å^3$. A datum collection of reflections was performed in 2θ ranges from 2 to 55°. No significant intensity variation was observed during the acquisition for the three standard reflections chosen for each recording. The crystal revealed a orthorhombic unit cell (a = 6.3218(13)Å, b = 7.555(2)Å, c = 36.774(7)Å, V =1756.4(6)$Å^3$). All carbon atoms were refined with isotropic displacement parameters and the H atoms are added manually, and their positions and thermal parameters are

fixed.

Computational Methods.

The structures of the isolated PPB and DSB molecules were determined by the density functional theory (DFT) methods implemented in the Gaussian 03 software package. The geometries of the molecules in the ground state were optimized at the B3LYP/6-31G(d) level of theory with the vibrational frequencies calculated at the same level being all positive numbers.

3.3 Results and discussion

3.3.1 Formation of PPB nanoparticles

A series of PPB nanoparticles with various percentage of water volume fractions viz. 0, 50, 55, 60, 65, 70, 75 and 80%, were prepared by the simple reprecipitation method using water as a poor solvent in THF. The evidence of the nanoparticle suspension was observed with the appearance of turbidity in the mixed solution when the volume fractions of water exceeded 65%. The color of solutions becomes deepened as the volume fractions of water increase from 65 to 70%. In addition, the size of the nanoparticles increased as a function of the volume fraction of water addition. Figure 3.1 shows the SEM photographs of PPB nanoparticles with different average particle sizes at various water volume fractions of solutions: (A) 50 nm at 65%; (B) 150nm at 70%; (C) 300 nm at 75%; (D) ~μm at 80%. It is observed that the free molecules in the solution starting to aggregate at 65% volume fractions of water addition.

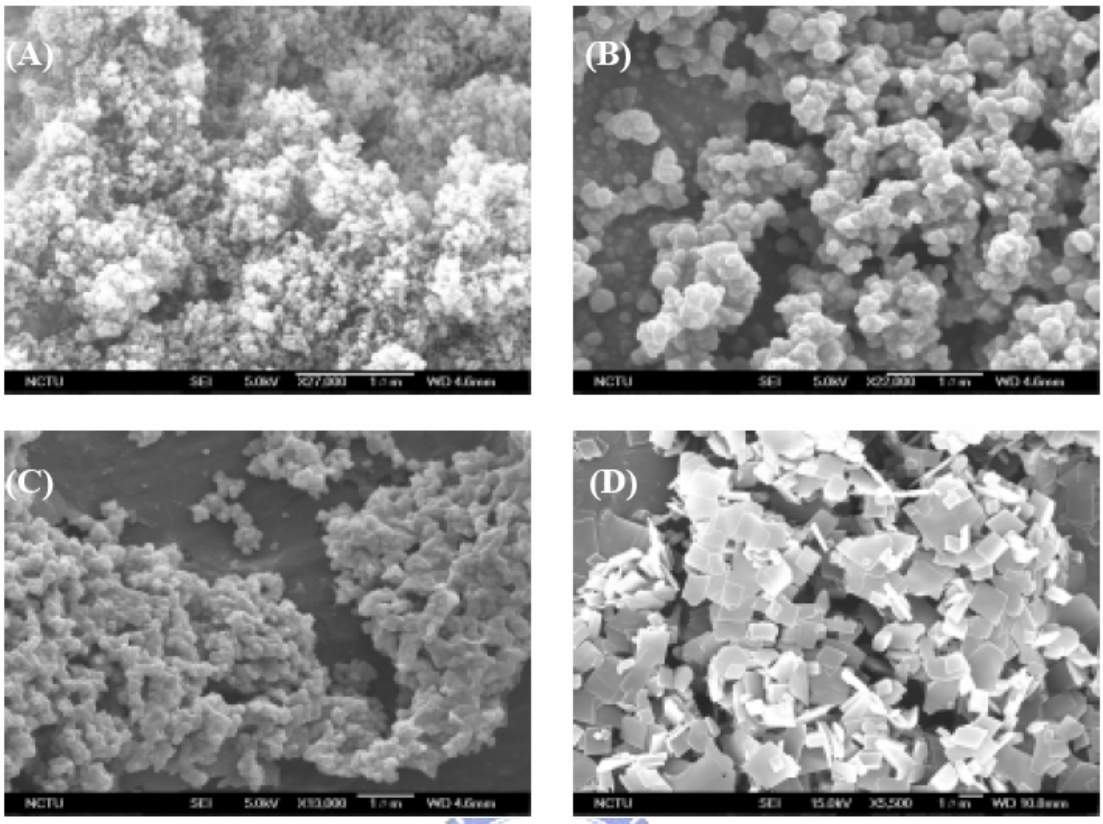

Figure 3.1: SEM images of PPB nanocrystals showing the sizes in average diameters of (A) 50, (B) 150, (C) 300 nm and (D) ~ μ m obtained from nanoparticle's suspension containing 65, 70, 75 and 80% volume fractions of water in THF, respectively.

In Figure 3.1, we found that the free molecule in the solution starting to aggregate at 65% volume fractions of water addition. In the preparation SEM samples, we need to dry the solvent on carbon tape, and aggregate might be formed. If the particle we observed is the aggregate formed during the evaporation, we should observe nanoparticles even in 0% water/THF solution, and the particle in all solution should the same. Therefore, we believed that the SEM image is not due to the aggregate formation during sample preparation. Initially, spherical shape particles were formed as the good solvent (THF) was replaced by the poor solvent (water). Therefore, the observing spherical shape of the nanoparticles is probably due to the minimization of interfacial energies between PPB and water molecules.[1] As the percentage of water addition became higher than 65%, the molecules aggregate to larger structures with

some germs of crystallization and the size of PPB nanoparticles increased dramatically. The size-dependent feature implies that the nanocrystallization of PPB proceeds as the water volume fraction of the solution increases, and it's because the water-insoluble PPB molecules aggregate together at higher water fractions. The size dependence in formation of PPB nanoparticles is similar to what has been reported recently in the cases of PDDP,[7a] DPP,[7b] and DAP.[7c] However, when the volume fractions of water addition increase up to 80%, the extraordinarily large particle size (~μm) is found, and the shape of the particle becomes rectangular (Figure 3.1D). The formation of rectangular nanoparticles in 80% solution is probably due to a competing process between the anisotropic growth and the spherical aggregation, which is similar to the case of recent study in evolving the one-dimensional nanostructures of *p*-BSP in water/THF mixtures.[1] In the present study, the size-dependent optical properties of the PPB nanoparticles are different from those of previous studies, which will be discussed in the following paragraphs.

3.3.2 Steady-state absorption/emission spectra

The UV/visible absorption spectra and the corresponding emission spectra at various volume fractions of water addition are shown in Figure 3.2A and 3.2 B, respectively. For the solutions of 0-65% water volume fractions, the UV/vis spectra (Figure 3.2A) feature a strong absorption band with maximum peak at 314 nm. As the water volume fractions increase to more than 70%, we observed the dramatic decrease in absorbance at 314 nm accompanying with the build up of new absorption band at 273 nm. The additional absorption band at 273 nm becomes more pronounced at 80%

solution. The blue-shifted nature in UV/Vis absorption spectra of the PPB nanoparticles is similar to what has been observed in the systems of DPST[8] and DSB.[11,12]

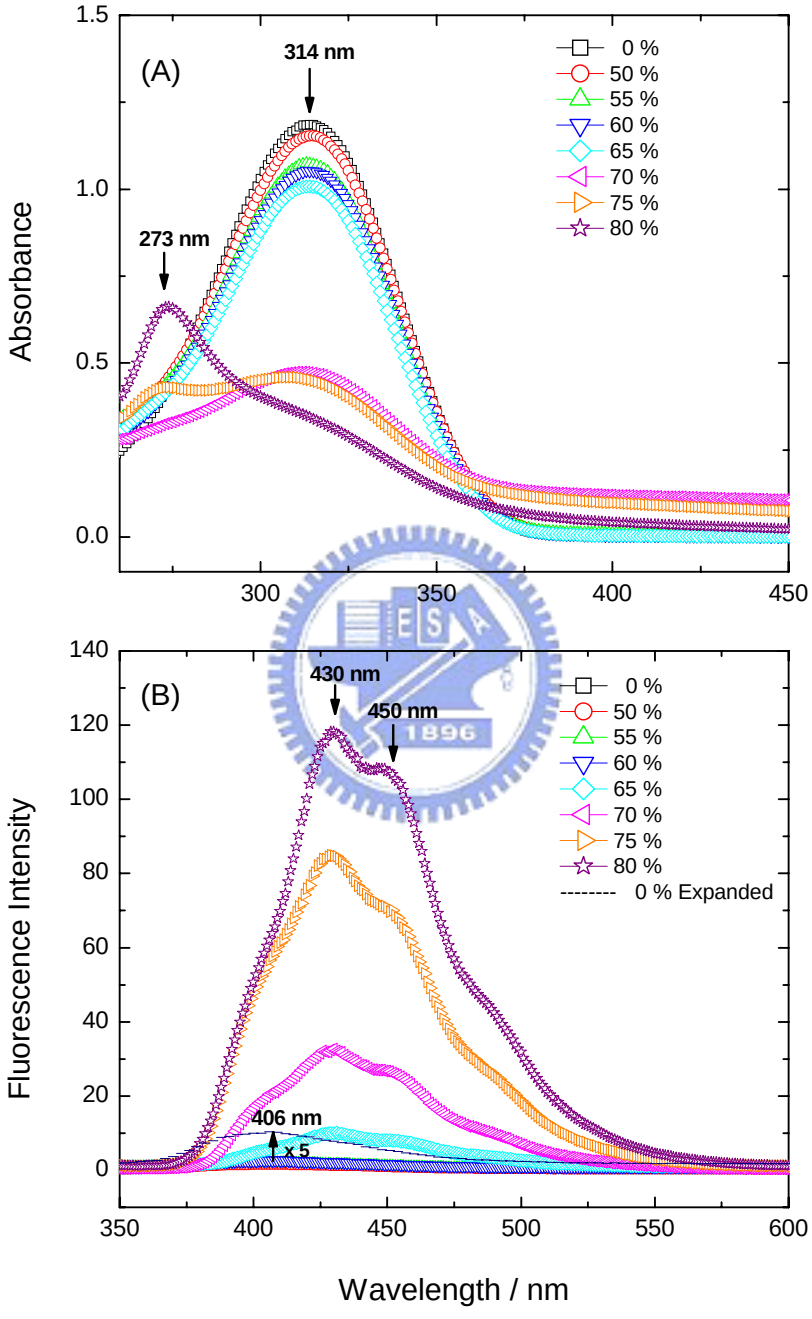

Figure 3.2: (A) UV-Visible absorption spectra changes of PPB depend on the water fractions in THF. (B) PL spectra changes of PPB depend on the water fractions in THF. The excitation wavelength was fixed at 310 nm.

[11] Oelkrug, D.; Tompert, A.; Gierschner, J.; Egelhaaf, H.-J.; Hanack, M.; Hohloch, M.; Steinhuber, E. *J. Phys. Chem. B* **1998**, *102*, 1902.
[12] Egelhaaf, H. J.; Gierschner, J.; Oelkrug, D. *Synthetic Metals* **1996**, *83*, 221.

The emission of PPB at 0–60% water volume fractions were hardly observed, which indicated the non-fluorescent nature of the free PPB molecule in solutions. In Figure 3.2B, the emission spectrum at 0% solution features a structureless broad emission band with the maximum peak at 406 nm. All the emission spectra with water volume fractions between 0–60 % are very similar in shape and intensity. As the water volume fraction becomes higher than 65 %, there are two new spectral features. First, the emission spectra at 65-80% solutions are distinctly shifted to a long wavelength region (peak maximum ~430 nm) with an apparent vibrational structure. Second, although the observed red-shifted emission spectra are all similar in shape, a substantial enhancement in intensity is found, and we found that the emission intensity increases with the particle size. (Figure 3.2B). Since the observed emission intensity systematically increases as a function of volume fractions of water addition, it reveals that formation of the PPB nanoparticles results in the enhancement of the emissions; the larger the particle size, the higher the emission intensity. This result is different from that of DPST[8] and DSB[11,12], in which the formation of nanoparticles accompany a substantial decrease in emission intensity.

The observed fluorescence enhancement in PPB nanoparticles is similar to that of CN-MBE nanoparticles.[8] In the literatures,[1,8] both intra- and intermolecular effects can be used to explain the observed fluorescence enhancement. Generally speaking, intramolecular effect assumes that the free molecules in solution undergo efficient nonradiative process via twisting motion, and the planar ones form in the solid state will suppress this channel. Intermolecular effect is arisen from intermolecular interactions when molecular aggregations become significant. This effect is strongly

dependent on the geometry of the packing structure. As described in the molecular exciton model,[13] two types of aggregations are involved: H-aggregates tend to accelerate the nonradiative relaxation process due to strong π-stacking interactions in the parallel aligned structures; J-aggregates, on the other hand, inhibit the nonradiative process for the molecules arranged in the head-to-tail direction. In the case of CN-MBE, the enhanced emission was attributed to both effects of intramolecular planarization and J-type aggregate formation in the nanoparticles, because a red shift in the UV absorption spectra was observed.[8] In our case, the UV spectra of PPB nanoparticles show a distinct blue shift (Figure 3.2A), which is usually an indication of the formation H-type aggregates. However, in figure 3.2B, the observation of the enhanced fluorescence cannot be explained by a usual H-type aggregation. More experimental evidence will be given in the following sections in order to understand the mechanism for the fluorescence enhancement of the PPB nanoparticles.

3.3.3 Picosecond relaxation dynamics of PPB nanoparticles

Time-dependent measurements of PPB in various water/THF solution mixtures were performed by TCSPC technique with excitation wavelength at 310 nm (λ_{ex}=310 nm), and probing at 420 nm (λ_{fl} = 420 nm). The transients are shown in Figure 3.3. The fluorescence decay in 0–60% volume fractions of water are all characterized exclusively by a sharp spike due to the limit of the time resolution of instrument response (~50 ps). However, the transient at 65% solution contains two major parts:

[13] Hans, K.; Försterling, H.-D. *Principles of physical chemistry: understanding molecules, molecular assemblies, supramolecular machines*; Wiley: New York, 2000

first part shows the fast-decay feature with the corresponding kinetics being instrument-limited; the second part shows a slow-decay character with the time coefficient in nanosecond time scale.

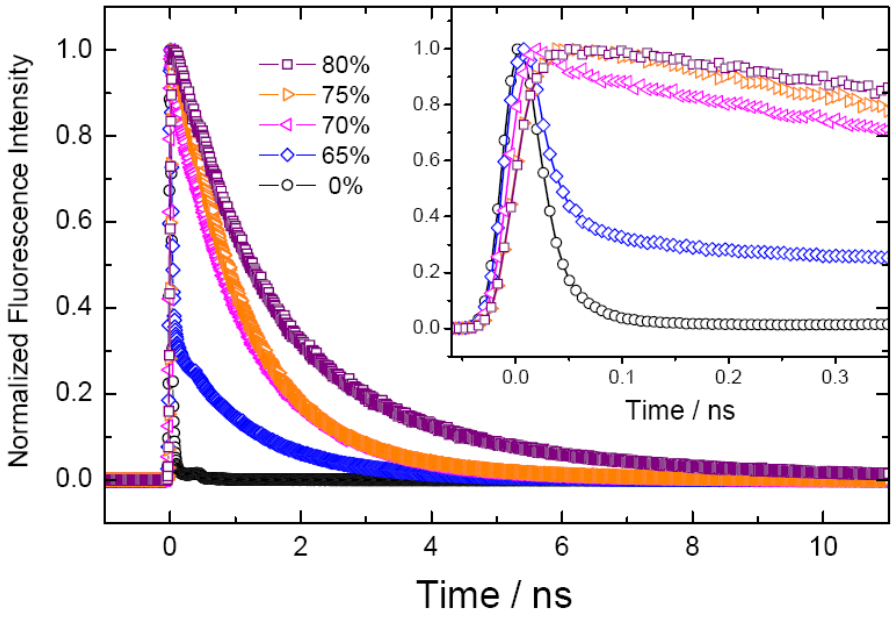

Figure 3.3: (A) Picosecond fluorescence transients of PPB shown in log scale are obtained from the excitation at λ_{ex} = 310 nm and the probe at λ_{fl} = 420 nm at various water/THF mixtures as indicated. (B) Picosecond fluorescence transients of PPB are shown in linear scale at 0, 65, 70, 75 and 80% solutions. The inset shows the corresponding transients in short time scale.

At 70% water volume fraction, the slow-decay part becomes the major component. When the water additions increase to 75% and 80%, the contribution of the fast-decay parts become negligible and the slow-decay parts become predominant in the transients. The above observations indicate that the formation of PPB nanoparticles leads to the formation of new components (the slow-decay part) in fluorescence transients with much longer excited-state lifetimes; the larger the nanoparticle size is, the more significant the slow-decay part becomes. This feature is consistent with the intensity enhancement in steady-state fluorescence spectra (Figure 3.2B). Since the fast-decay part arise from the contribution of free PPB molecules (studied by using

the femtosecond technique will be discussed below), we only focus on discussing the kinetic data of the PPB nanoparticles obtained from the 65–80% solutions. Figure 3.4A, B, and C show three typical transients of the 75% solution with λ_{ex} = 310 nm and λ_{fl} = 390, 450 and 510 nm, respectively

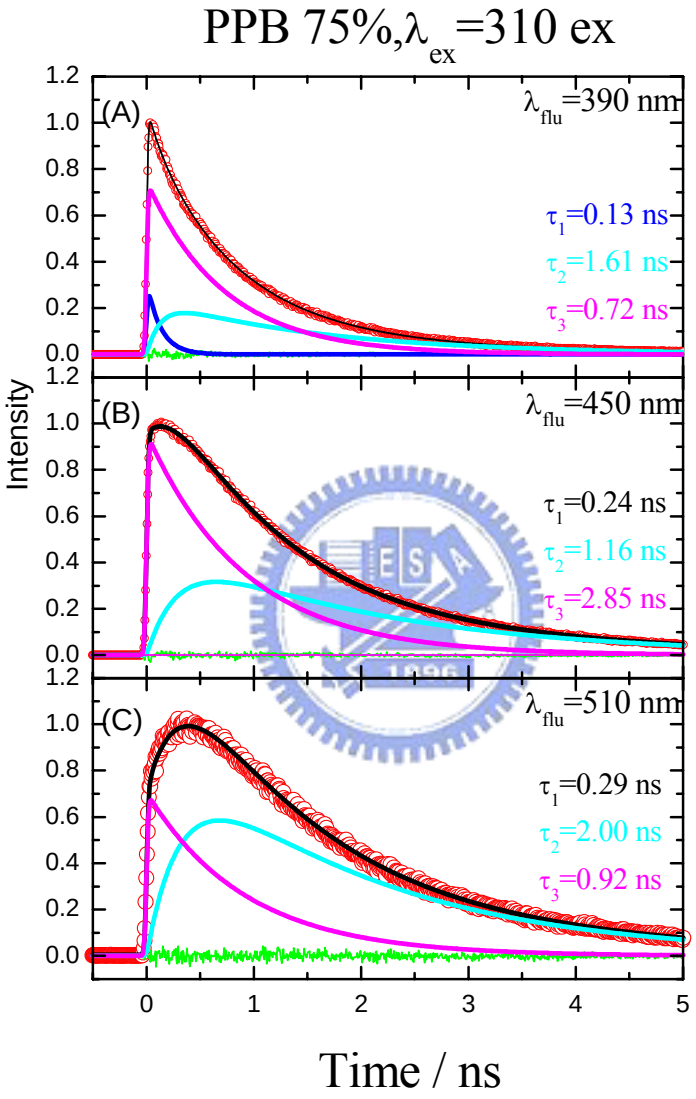

Figure 3.4: Picosecond fluorescence transients of PPB at 75% solution with λ_{ex} = 310 nm and λ_{fl}/nm = (A) 390, (B) 450 and (C) 510. The data are fitted according to the dual-emissive model (Scheme 2). The solid black curves are theoretical fits with residues shown as the green traces. The τ_1, τ_2 and τ_3 correspond to the A and B, and A′ in Scheme 2, respectively.

The transients show complex kinetic features, which cannot be described by a single exponential decay function. Since the transient at λ_{fl} = 510 nm clearly features

a rising character, a consecutive kinetic model, $A \xrightarrow{\tau_1} B \xrightarrow{\tau_2} C$, should be utilized for the curve-fitting procedure. In this Model, A represents the initial Franck-Condon (FC) state upon excitation, B stands for the excited state of the PPB nanoparticles (bright state), and *C* represents the ground state of the nanoparticles (dark state). The result indicates that the FC state decays with a time coefficient, τ_1, while the bright state builds up in τ_1 and then decays to the dark state in τ_2. This kinetic model is consistent with the dual-state model utilized in fitting the kinetic data of the DSB aggregates, in which A represents the intrinsic excitonic state and B for a low-energy defect state.[14]

Even though the consecutive Model was able to describe the rise and decay feature of the transients, the fitting quality of the decay part was not satisfying. In order to solve this problem, another component (*A′*) was added in the consecutive kinetic model (as shown in scheme2), while *B′* was produced parallel with *B*. In this case, *A′* represents another bright state of the PPB nanoparticles, and the structure might be different from component A. Based on this Model, all transients of 65-85% solutions can be described well, and the fitted parameters are summarized in Table 1, and Figure 3.5 shows the fitting time coefficient as a function of fluorescence.

For comparison, we also measured the time-resolved transient of the PPB crystal. We found that the transients of bulk single crystal of PPB involve no rising character, and can be well fitted by a single-exponential decay with minute offset. (Appendix B) According to the above kinetic analysis of the fluorescence transients, three dynamical features of the excited PPB nanoparticles emerge.

[14] Lim, S.-H.; Bjorklund, T. G.; Bardeen. C. J. *J. Phys. Chem. B* **2004**, *108*, 4289.

Table 1. Fitted time constants of PPB in various volume fractions of water/THF solutions at λ_{ex} = 310 nm.[a,b]

λ_{fl}	390 nm				420 nm				450 nm			
	65%	70%	75%	80%	65%	70%	75%	80%	65%	70%	75%	80%
τ_1/ns	0.31 (0.04)	0.05 (0.19)	0.13 (0.25)	0.09 (0.26)	0.26 (0.14)	0.30 (0.08)	0.22 (0.06)	0.23 (0.15)	0.26 (0.16)	0.39 (0)	0.29 (0)	0.23 (0.18)
τ_2/ns	1.00(0.02)	1.48 (0.08)	1.61 (0.17)	2.30 (0.19)	1.26 (0.10)	1.79 (0.16)	2.04 (0.17)	3.45 (0.23)	1.66 (0.19)	1.78 (0.35)	2.00 (0.31)	4.03 (0.35)
τ_3/ns		0.68 (0.19)	0.72 (0.58)	0.94 (0.55)		0.87 (0.60)	0.88 (0.77)	1.16 (0.63)		0.92 (0.65)	0.92 (0.69)	1.45 (0.47)
τ /ns[c]	0.02 (0.94)	0.01 (0.55)			0.02 (0.75)	0.03 (0.16)			0.02 (0.65)			
λ_{fl}	480 nm				510 nm				540 nm			
	65%	70%	75%	80%	65%	70%	75%	80%	65%	70%	75%	80%
τ_1/ns	0.35 (0.14)	0.41 (0)	0.32 (0)	0.31 (0.17)	0.39 (0.10)	0.41 (0)	0.32 (0)	0.36 (0.13)	0.40 (0.07)	0.45 (0)	0.32 (0)	0.42 (0)
τ_2/ns	1.78 (0.23)	1.73 (0.50)	1.89 (0.45)	4.28 (0.43)	1.86 (0.22)	1.69 (0.59)	1.87 (0.54)	4.43 (0.49)	1.92 (0.18)	1.68 (0.63)	1.86 (0.62)	5.04 (0.48)
τ_3/ns		0.91 (0.50)	0.89(0.55)	1.71 (0.40)		0.88 (0.41)	0.92 (0.46)	2.07 (0.38)		0.88 (0.37)	0.92 (0.38)	2.52 (0.52)
τ /ns[c]	0.02 (0.64)				0.02 (0.68)				0.02 (0.75)			

[a]The numbers in brackets are the relative amplitudes; the value was set to zero if the contribution of the component was too small to fit. [b]All parameters were obtained according to the kinetic model shown in *Scheme 2* except the transients of 65% solution via a simple consecutive model. [c]Time constants due to free PPB in solution are instrument-limited (<30 ps). The deconvolution of each transient was shown in appendixA.

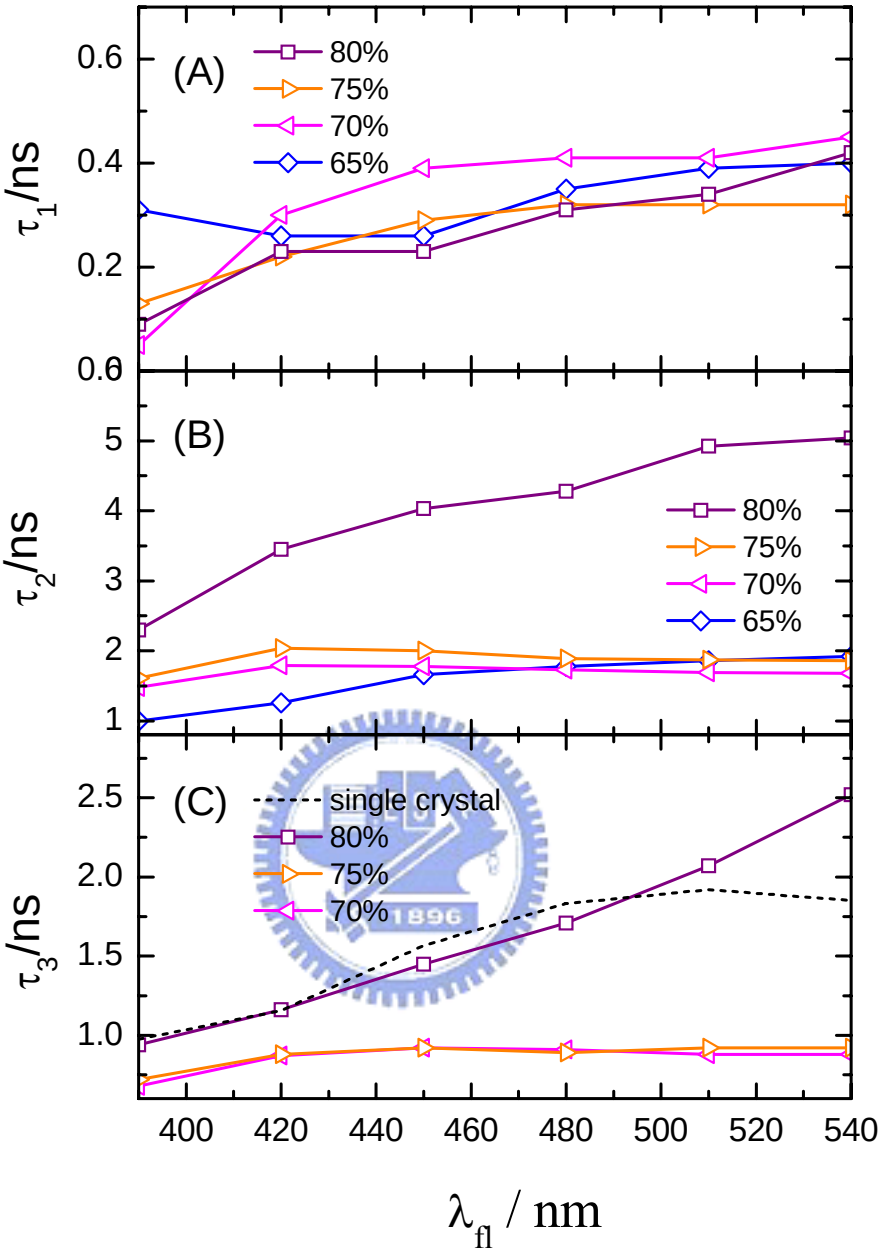

Figure 3.5: Three fitted temporal coefficients of PPB, (A) τ_1.(B) τ_2, and (C) τ_3. the corresponding fitted parameters are summarized in Table 1. The dashed curve shown in (c) represents the wavelength-dependent single-exponential-decay coefficient of the PPB single crystal.

SCHEME 2: A Dual-Emissive Model

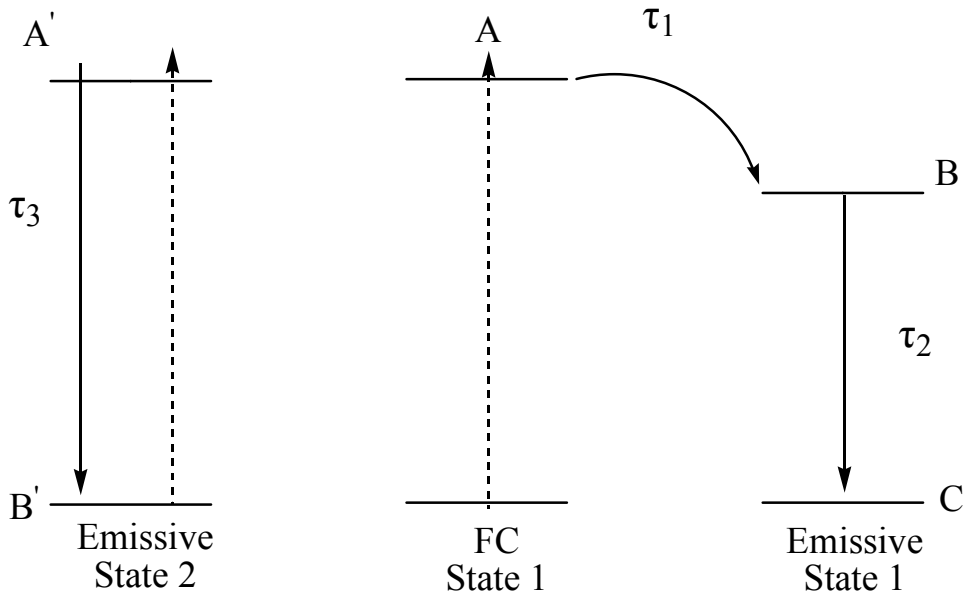

First, the observed time coefficients (Table 1 and Figure 3.5) are highly dependent on the probing wavelength. At longer wavelength, the fluorescence is emitted from the more relaxed state.[15] The systematic increasing in all time constants (τ_1–τ_3) as a function of λ_{fl} indicates that the energy-dependent nature of the relaxation in excited states of the nanoparticles.

Second, τ_2 and τ_3 are size-dependent, i.e., longer lifetimes are observed at larger nanoparticle size, and this relationship is more pronounced for τ_3. This size-dependent behavior on emission lifetimes was also reported for the systems of anthrance and DAP nanoparticles. Fluorescence quantum yield (Φ_F) can be obtained from the ratio of τ_f/τ_r, where τ_r is the time coefficient of the radiative process, and τ_f is the fluorescence lifetime. Assuming the radiative lifetime τ_r of free PPB and PPB nanopaticles is similar; the observed longer τ_f means the greater Φ_F. That explains the

[15] Lu, Y. C.; Chang, C. W.; Diau. E. W. G. *J. Chin. Chem. Soc* **2002**, *49*, 693.

increase in the emission intensity is the result of growth in nanoparticles. (Figure 3.2B).

Third, τ_3 for the 80% solution matches the decay coefficient of the single crystal with a lifetime in the range 1-2 ns, indicating a similarity between emissive state 2 in PPB aggregates (Scheme 2) and PPB bulk crystal. Therefore, the observing τ_3 was attributed to the fluorescence decay from the single crystal like structure in PPB aggregates. PPB aggregates in emissive state 1 were produced from the initial FC state with a rise time τ_1 and then decay with τ_2; this dual-state feature resembles that of DSB aggregates, in which the observed non-exponential fluorescence decays were modeled by two coupled excited states via an energy-transfer process from the excitonic state to the defect state, and it was similar to the procedure in our kinetic Model I mentioned previously.

To provide structural information for the two emissive states, the X-ray diffraction experiments based on the colloid samples of the 65-85% solutions were carried out.

3.3.4 Molecular structures of PPB in solid state and in solution

Powder XRD patterns of the colloid samples with different water additions (65-85%) are shown in Figure 3.6B. In the 2θ ranges of 6-15°, there are two diffractions at 2θ = 9.6° and 14.5° corresponding to [004] and [006] diffraction planes of the bulk materials. On the other hand, a new diffraction peak at 2θ = 7.3° (d = 12.2 Å) is clearly observed in XRD data of all 65-80% samples, and the diffraction intensity at 2θ = 7.3° shows no direct correlation for the samples of different water additions. The new diffraction peak suggests that a new type of three-dimensional

packing of the PPB molecules is formed when the colloid samples are prepared in the presence of H_2O.

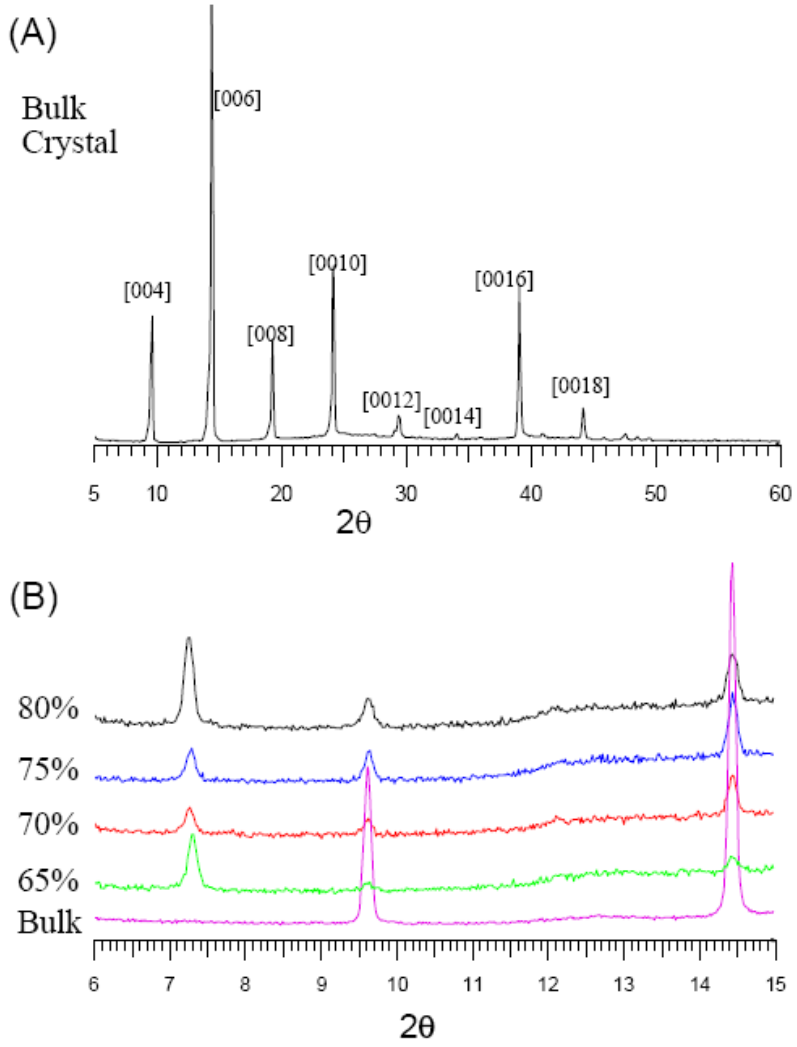

Figure 3.6: (A) Powder XRD pattern of the PPB bulk material. (B) Powder XRD patterns of the colloid PPB samples from various water/THF mixtures as indicated.

The presence of diffractions at both $2\theta = 7.3°$ and $2\theta = 9.6°/14.5°$ in water treated samples indicates that the water-induced PPB nanoparticles should contain two types of long range PPB packing structures. One is the same as the bulk material described below and the other is going to be uncovered. Because we do observe an induction period (τ_1 = 0.1–0.4 ns shown in Figure 3.4) for formation of the bright states, it is expected that water molecule may be involved in the unknown structure of the PPB

nanoparticles giving rise to the so-called “defect state” as proposed in the case of DSB aggregates.[14] The powder X-ray diffraction results have confirmed that two different packing structures are involved in the PPB nanoparticles. These result support our picosecond time-resolved experiments, in which we proposed two structures are exists in PPB nanoparticles.

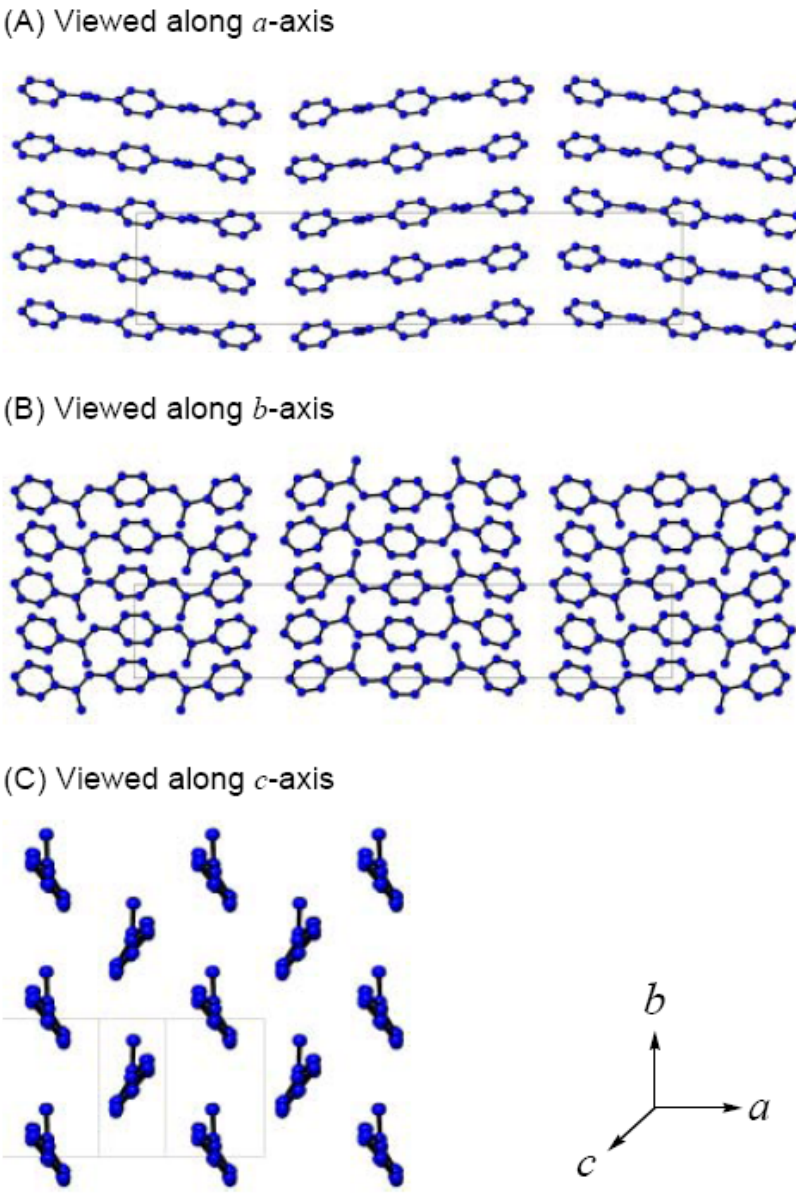

Figure 3.7: (A) Powder XRD pattern of the PPB bulk material. (B) Powder XRD patterns of the colloid PPB samples from various water/THF mixtures as indicated.

Single crystal suited for the X-ray diffraction study was prepared from the slow

evaporation of PPB in THF solution. Figure 3.7 shows the crystal structures of the plate-shaped PPB in three directions. There are four independent PPB molecules in a unit cell. The packing of PPB molecules alone *a*-axis shows the herringbone type structure (Figure 3.7A). Such molecular packing feature is similar to that of the chemically related compound (DSB). For each PPB molecule, the ethylene groups are parallel to *a*-axis and twisted with respect to the benzene ring in an average torsion angle of 31°. The direction of the ethylene groups in PPB molecule is shown in Figure 3.7B. For each PPB molecule, there are three benzene rings connected by two ethylene groups. Each ethylene group connects to two benzene rings in *trans*-form. The central benzene ring is connected with two phenyl groups via the ethylene bond in para- positions. It is apparent that the ethylene groups on 1,4-sites of the central phenyl ring are pointing to the same side.

The intermolecular packing of PPB molecules is shown in Figure 3.7C for a single layer of PPB molecules on the *ab* plane. The structure has been rotated 7° alone the *a*-axis to make the PPB molecule nearly perpendicular to the plane. It is quite obvious that each ethylene groups are parallel to the *a*-axis and twisted with respect to the benzene ring. The 2D packing of PPB molecule on the *ab* plane is close to the edge-to-face interactions of a 2×2 pinwheel, similar to that of DSB.[16]

For free PPB molecule, the structure was estimated using theoretical method. The structure was optimized at B3LYP/6-31G(d) level of theory. The optimized structures of the isolated PPB and DSB molecules are shown in Figure 3.8A and B, respectively. The free DSB molecule has a perfect planar geometry with all atoms located in the

[16] Spano. F. C. *Synth. Met.* **2001**, *116*, 339.

same symmetry plane, but surprisingly the structure of the free PPB molecule is non-planar with one end benzene ring twisted out of the molecular plane by ~80°. Note that the molecular structure of the free PPB molecule (Figure 3.8A) is entirely different from the structure in single crystal (see Figure 3.7B), where the three benzene rings in the latter are aligned parallel to a symmetry plane similar to the planar geometry of the free DSB molecule (Figure 3.8B).

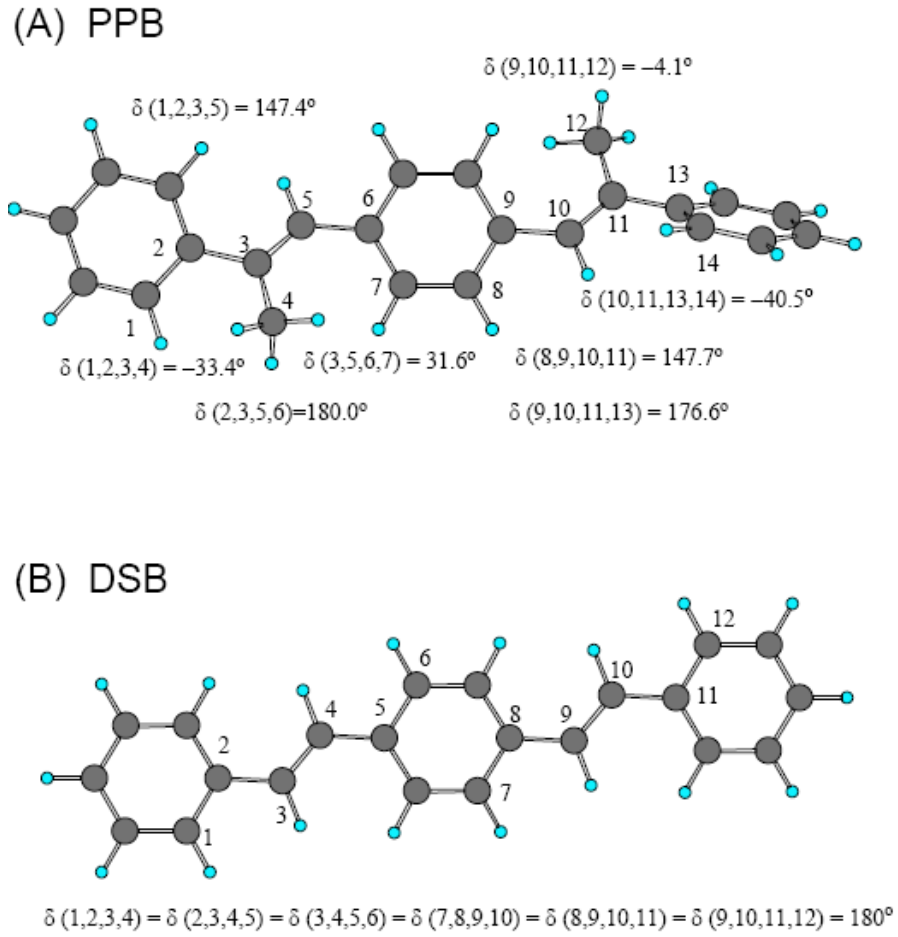

Figure 3.8: The ground state structures of (A) PPB and (B) DSB optimized at the B3LYP/6-31G(d) level of theory. The relevant torsional angles are indicated.

The correlation of the emission intensities on molecular structures of PPB between the solution and the solid phases has been found: the twisted conformation of the free PPB molecule is essentially non-fluorescent in dilute solution while the near planar geometry of the PPB unit cell in nanocrystals gives very strong emission in the solid

state. The conformational planarization of the PPB molecules when forming the nanoparticles seems to be the reason for the observed emission enhancement in the solutions of 65-80%. To further understand how the molecular planarity affecting the excited-state relaxation dynamics, we performed femtosecond fluorescence up-conversion measurements for both PPB and DSB molecules in dilute THF solution.

3.3.5 Femtosecond relaxation dynamics of free PPB and DSB molecules in THF

The structures of isolated PPB and DSB molecules are intrinsically different (Figure 3.8). The twisted geometry of PPB might due to the balance between strong hyper-conjugation of the methyl groups with the individual benzene rings and the long-range conjugation across all benzene rings. On the other word, PPB in dilute solution is nearly non-fluorescent, but free DSB molecules do give strong emissions.[11,12] Figure 3.9A and B show two typical fluorescence transients taken at λ_{ex} = 355 nm and λ_{fl} = 450 nm for PPB and DSB in THF, respectively. Apparently, the fast kinetics of PPB in 0% solution has now been unraveled. The transients were analyzed according to a proper kinetic model with convolution of instrument response function. For PPB, the transient are fitted with the combination of an independent exponential decay ($A' \xrightarrow{\tau_1} B'$) and a consecutive model ($A \xrightarrow{\tau_2} B \xrightarrow{\tau_3} C$). The decay time constants of τ_1, τ_2, and τ_3 are 1.3 ps, 9.2 ps and ~ns, respectively. For DSB, a consecutive model ($A \xrightarrow{\tau_1} B \xrightarrow{\tau_2} C$) is sufficient for an appropriate fit of the transient, where the two decay time constants are 13 ps and ~ns for τ_1 and τ_2, respectively. It reveals that the contribution of the ns component in the transient of

PPB is very minor while it becomes the major part of the transient in DSB.

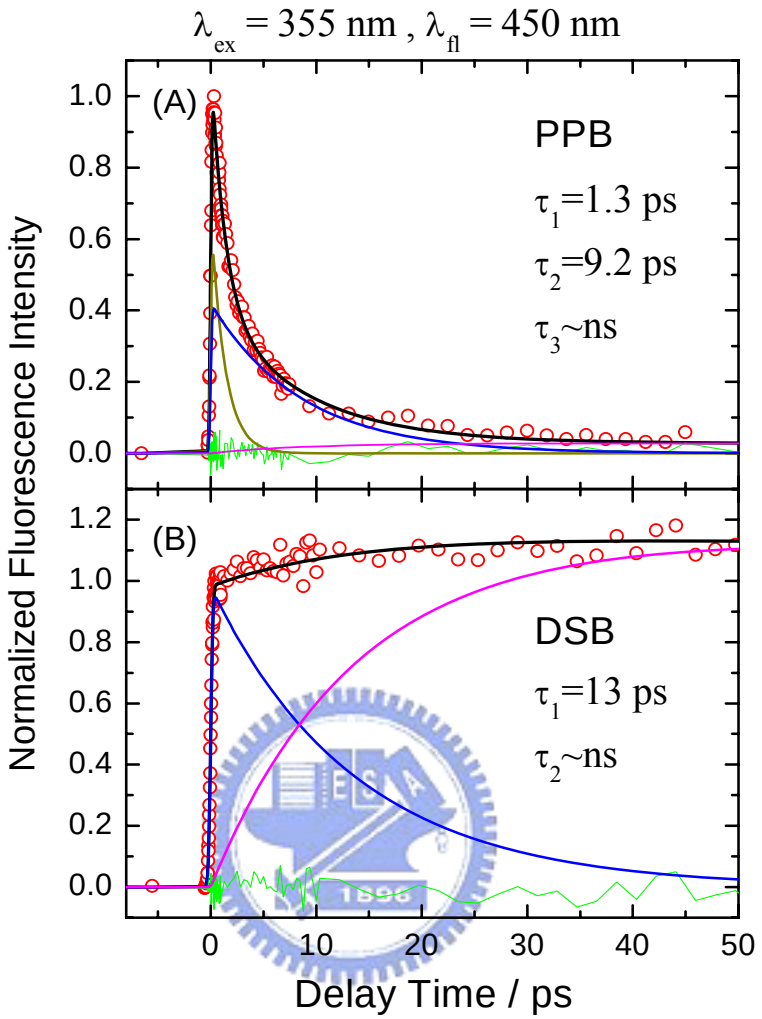

Figure 3.9: Femtosecond fluorescence transients of (A) PPB and (B) DSB in pure THF obtained from λ_{ex} = 355 nm and λ_{fl} = 450 nm. The transient of PPB was fitted according to a combined consecutive kinetic model, $A' \xrightarrow{\tau_1} B'$ and $A \xrightarrow{\tau_2} B \xrightarrow{\tau_3} C$, while that of DSB by a simple consecutive model, $A \xrightarrow{\tau_1} B \xrightarrow{\tau_2} C$. The solid black curves are theoretical fits with residues shown as green traces; the blue and magenta curves under each transient are the deconvoluted components corresponding to *A* and *B*, respectively; dark yellow curve shown under the transient of PPB represents *A'*.

This result is coincident with the steady state results, in which no observable emission for the former whereas strong emission was observed for the latter. On the other hand, the contribution of the ~1 ps component is significant in the transient of PPB, but it is negligible in the transient of DSB.

The fast ps component is unambiguously shown in the transient of PPB and therefore plays an important role in reducing the contribution of the ~ns component of fluorescence transient. Since the free PPB molecule has a twisted geometry while the free DSB molecule is completely planar (Figure 3.8), the existence of a correlation between the molecular structure and the observed relaxation dynamics is evident and will be discussed in the following.

According to the results obtained from the isolated *trans*-stilbene molecule, a planar molecule with two benzene rings connected by an ethylene group in a *trans* form, and the nonradiative process in the first singlet excited state (S_1) is governed by the isomerization of the ethylene twisting reaction coordinate with an energy barrier of only 3.4 kcal mol^{-1}.[17,18] Taking into consideration of the photoisomerization mechanism of *trans*-stilbene for the systems of present study, the observed ps relaxation in non-planar PPB is the result of crossing a small energy barrier along the C=C rotation channel on the S_1 surface. An efficient $S_1 \rightarrow S_0$ internal conversion follows at the perpendicularly twisted conformation, (so-called "phantom state" in the system of stilbene)[17,18] so that the ns component is hardly observed. For the planar DSB molecule, the ps nonradiative deactivation through the C=C twisting motion was not observed, probably due to a high energy barrier involved along the isomerization channel in S_1 state. Solvent-induced vibrational relaxation (VR) will also compete with the barrier-crossing deactivation process, and this leads to the ~10 ps component in both systems. Since the isomerization deactivation is much slower than the VR process in DSB, the electronically excited molecules would preferentially lose their

[17] Baskin, J. S.; Banares, L.; Zewail, A. H. *J. Phys. Chem.* **1996**, *100*, 11920, and references therein
[18] Felker, P. M.; Zewail, A. H. J. Phys. Chem. **1985**, 89, 5420

vibrational energy in the S_1 state, so that the electronic relaxation can only occur in the "cold" S_1 state which gives rise to the prominent ns component observed in DSB.

3.3.6 Femtosecond relaxation dynamic of PPB and DSB nanoparticles

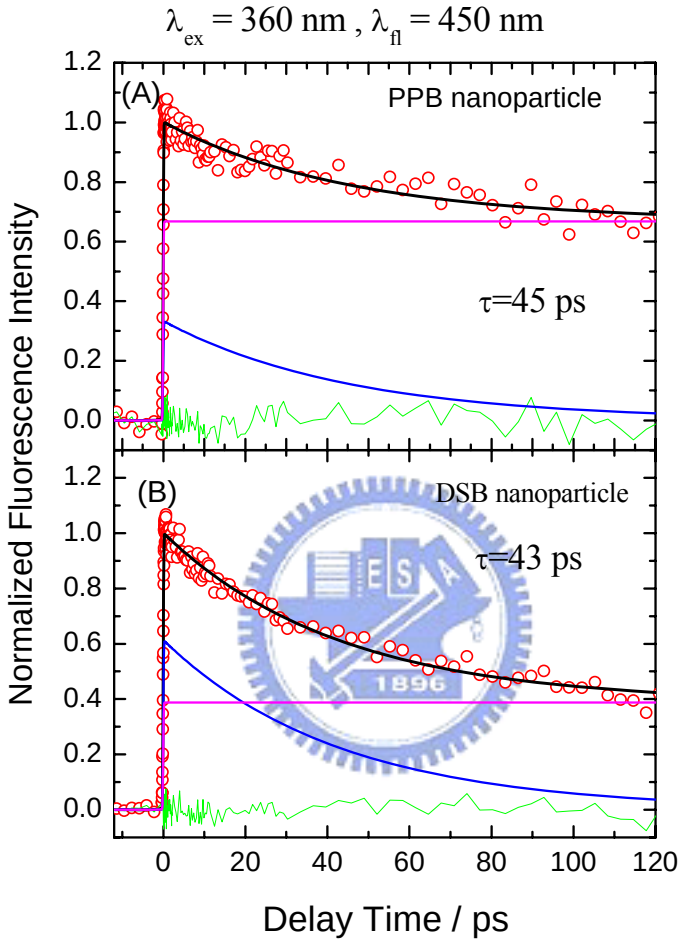

Figure 3.10: Femtosecond transients of (A) PPB and (B) DSB nanoparticles in 75% solution. The transient was obtained from λ_{ex}=360 nm and λ_{em}=450 nm. Both transient can be fitted by a bi-exponential function. The fast component (blue) decays ~45 ps, and the slow component (magenta) persists in 0~100 ps region.

Figure 3.10 , show two typical fluorescence transients taken at λ_{ex}=360 nm and λ_{em}=450 nm for PPB and DSB nanoparticles produced from the 75% solutions. Both transient can be fitted with a ~45 ps decay with an offset. In TCSPC experiment, because of the relatively worse temporal resolution , the ~45 ps is unresolved. Because the nuclear motions are restricted in nanoparticles, and the above-mentioned

rotational induced nonradiative process is inhibited. The observed 45 ps component in both systems might be due to the nonradiative deactivation process through intermolecular interactions involving π-stacking of the carbon backbones. In DSB nanoparticles, the relative amplitude of the 43 ps component is significant larger than in PPB nanoparticles, which states the stronger π-overlap interaction in solid state,[19,20] and this results in the much smaller quantum yield for DSB nanoparticles than for DSB in solution.[21]

3.4 Concluding Remarks

In the present study we reported the size-dependent optical properties of PPB nanoparticles prepared by reprecipitation in various volume fractions of the water/THF solutions and characterized by SEM, XRD, picosecond and femtosecond time-resolved laser spectroscopy methods. We observe strong emissions in PPB nanoparticles, but the emission of free PPB in dilute solution is hardly observed. In addition, fluorescence intensities of the nanoparticles systematically increased with the increasing of nanoparticle size. Femtosecond fluorescence measurements have shown that the nonradiative deactivation process through the ethylenic twisting isomerization channel was very efficient in PPB but inactivated in DSB. These dynamical behaviors were inferred due to the discrepancy of the structures between PPB and DSB in dilute solution, i.e., the twisted geometry of the PPB molecule should involve a small energy barrier for an efficient deactivation while the planar

[19] Wu, C. C.; DeLong M. C.; Vardeny, Z. V.; Ferraris J. P. *Synth. Met* .**2003**, 137, 939-941.
[20] Van Hutten, P. F.; Wildeman, J.; Meetsma, A.; Hadziioannou, G. *J. Am. Chem. Soc.* **1999**.121, 5910-5915.
[21] Oelkrug, D.; Tompert A.; Gierschner, J. Egelhaaf, H.-J.; Hanack, M.; Hohloch, M.; Steinhuber, E. *J. Phys. Chem. B* **1998**,102,1902-1907.

DSB molecule must involve a deactivation energy barrier that is too large to overcome in the excited state. This rationalizes the non-fluorescent nature of the twisted PPB molecule in dilute solution and establishes the concept of the molecular planarity giving strong fluorescent emissions in the PPB nanoparticles. The nearly planar geometrical nature of the PPB unit cell in the single crystal has been confirmed by our XRD studies. Moreover, powder XRD experiments demonstrated that there are two different packing structures involved in the PPB nanocrystals. One forms aggregates with the herringbone-type arrangement as observed in single crystal while the other is not yet to be determined. The dual-aggregate feature of the nanoparticles reflects the non-exponential kinetics in the picosecond time-resolved experiments for two emissive states being observed, one shows a single-exponential decay feature as observed in single crystal, and the other shows a rising feature assigned to be due to the unknown structure observed in the XRD data. In summary, we have found that PPB nanoparticles show weak emission in dilute solution but blue-shifted absorption and anomalously strong emissions in the aggregates. We provided experimental evidence for the enhanced emission of the nanoparticles being due to the combined effects of the conformational planarization, and the herringbone-type aggregate formed with an edge-to-face feature shown in the single crystal structure of PPB.

Chapter 4 Relaxation Dynamics of CNDSB Nanobelts

4.1 Introduction

In previous section, we have report the relaxation dynamics of PPB and its nanoparticles by the using of field-emission scanning electron microscopy (SEM), femtosecond (fs) and picosecond (ps) time-solved spectroscopy, and X-ray diffraction (XRD).[1] With the same methods, we extend our work to its derivatives: (*Z*)-3-{4-[(*Z*)-2-cyano-2-phenyl-1-ethenyl]phenyl}-2-phenyl-2-propenenitrile(CN-DSB, the structure was shown in scheme 1).

Scheme 1

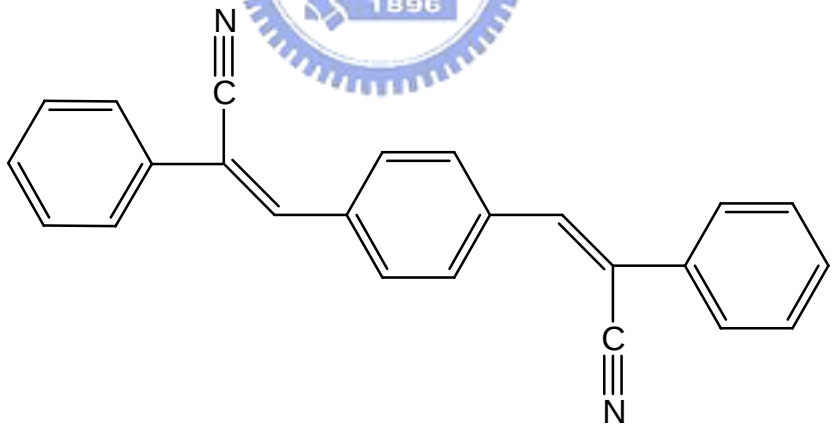

With the application of reprecipation method,[2] CNDSB form nanobelts as the volume fraction of water exceeds 70%. Like the case of PPB, CN-DSB itself is nonfluorescent and emitting strong fluorescence as it forms nanobelts. In this study

[1] Bhongale, C. J.; Chang, C. W.; Lee, C. S.; Diau, E. W. G.; Hsu, C. S. *J. Phys. Chem. B* **2005**, *109*, 13472

[2] Kasai, H.; Nalwa, H. S.; Oikawa, H.; Okada, S.; Matsuda, H.; Minami, N.; Kakuta, A.; Ono, K.; Mukoh, A.; H., N. *Jpn. J. Appl. Phys.* **1992**, *31*, 1132.

we measured the fluorescence lifetime of CN-DSB nanobelts and single crystal. The results indicate that two emissive states exist in those two conditions. We test the role of intramolecular motion by comparing the ps and fs time-resolved transients of CN-DSB in THF and Poly (methyl methacrylate) (PMMA). The result reveals that the intramolecular motion would lead to an efficient nonradiative channel, which caused the low quantum yield of CN-DSB THF solution. We also measure the fs time-resolved fluorescence decay of CN-DSB nanobelts in 80% water/THF solution. In CN-DSB nanobelts we observed a unique ultrafast decay, which was absent in PPB nanoparticles[1] , and the origin of this ultrafast decay will be discussed.

4.2 Experimental Section

Materials. CN-DSB was synthesized by Knoevenagel reaction.[3] Typically, KOH (4.2 g, 75.14 mmols) was added to a solution of terephthaladehyde (5.0 g, 37.20 mmol) and phenylacetonitrile (8.8 g, 75.14 mmol) in ethanol (50 mL). A greenish yellow gel-type mixture was formed immediately after addition. The resulting solution was stirred for overnight at room temperature. The mixture was then filtered and washed several times by ethanol. The crude power was recrystallized from chloroform to give greenish yellow solid (yield, 45%). ^{1}H NMR (300 MHz, $CDCl_3$): δ= 8.00 (s, 2H; Ar-H), 7.72-7.7.69 (m, 4H; Ar-H), 7.56 (s, 2H; Ar-H), 7.47-7.44 (m, 6H; Ar-H), 7.26 (s, 2H; vinyl); m.p. 270-272^{o}C.

Formation of Nanostructures. CN-DSB nanostructures were obtained by a simple reprecipitation method. Water served as a precipitating solvent for CN-DSB in THF.

[3] Pond. S. J. K.; Rumi , M.; Levin, M. D.; Parker, T. C.; Beljonne, D.; Day, M. W.; Brédas, J.-L.; Marder, S. R.; and Perry. J. W. *J. Phys. Chem. A* **2002**, *106*, 11470.

Volume fractions of water were added up to 90%, with vigorous stirring at 296 K. Distilled water and THF were filtered with a membrane filter (pore size 0.2μm). In all samples, the concentration of chromophore (3.6×10^{-5} M) is kept at 3.6×10^{-5} M. To test the concentration effect on the formation of CN-DSB nanostructures, the sample with different concentrations, viz. 1.8 x 10^{-5} M, 3.6×10^{-5} M, and 7.2×10^{-5} M are prepared. These suspensions were homogenous and stable. Samples for SEM tests were prepared by dropping the sample mixture onto a microscopic glass or carbon tape and dried under vacuum.

Steady-state Spectral Measurements. ^{1}H NMR spectra were recorded (Unity-300 spectrometer at 300 MHz) in $CDCl_3$ solutions. Images were acquired on a field-emission scanning electron microscope (JSM-6500 F, JEOL); to enhance the conductivity of the specimen, a layer of platinum was sputtered for 30 s at a current 30mA and a pressure 4Pa. UV-visible absorption spectra (Hewlett-Packard HP8453 spectrometer) and fluorescence spectra (Hitachi F4500 spectrophotometer) were measured in standard manners.

4.3 Results and Discussion

4.3.1 Formation of CN-DSB Nanostructures

CN-DSB nanostructures in series volume fractions of water, viz. 0, 70, 80 and 90%, were prepared according to a simple reprecipitation method with THF as solvent and water as non-solvent. As the percentage of water was increased, because of the formation of nanostructures, the solution became milky. The shape of nanostructures

also changed from curvy nanoparticles (at 70%) to nanobelts (at 80 and 90%). Parts A, B and C in Figure 4.1 presents the SEM photographs of CN-DSB nanostructures obtained by varying the percentage of water in THF solution of CN-DSB. Although the aggregation of CN-DSB molecules might start at the early stages of mixing, well-evolved nanostructures only could be observed as the water volume fraction exceeding 70%. As the proportion of added water became greater than 70%, the molecules aggregated to larger structures, and the shape and size of CN-DSB nanostructures changed greatly giving rise to nanobelts. The formation of nanobelts is more or less similar to the case involving one-dimensional nanostructures of *p*-BSP in mixtures of water and THF.[4] Concentration dependence of the formation of CN-DSB nanostructures was also studied. The nanobelts suspensions were prepared at different concentrations, and the water percentage was controlled at 80%. The result indicates that with the increasing of concentration, only the size along the entire length of nanobelts increasing from 150 nm to 300 nm, and no other significant change is observed. (Figure 4.1D, B and E).

[4] Yoshikava, H.; H., M. *J. Photochem. Photobiol., C* **2000**, 57.

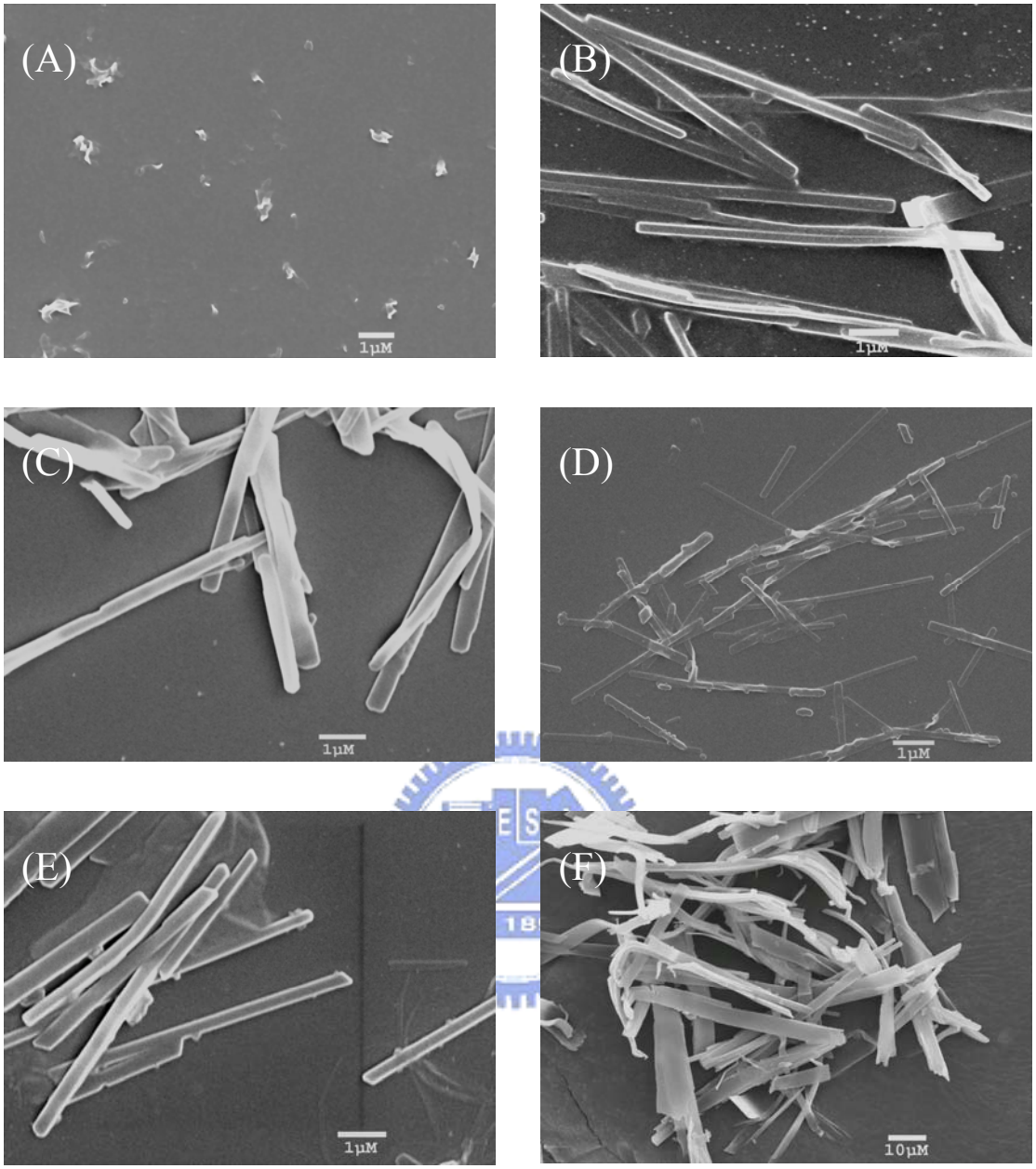

Figure 4.1: SEM images showing the evolution of CN-DSB nanostrutures obtained at different water additions and at concentrations of 3.6×10^{-5} M. (A) 70, (B) 80, (C) 90% to THF, (D) 1.8×10^{-5} M for 80% solution, (E) 7.2×10^{-5} M for 80% solution, and (F) CN-DSB bulk crystals, respectively.

4.3.2 Steady-state Absorption/Emission Spectra

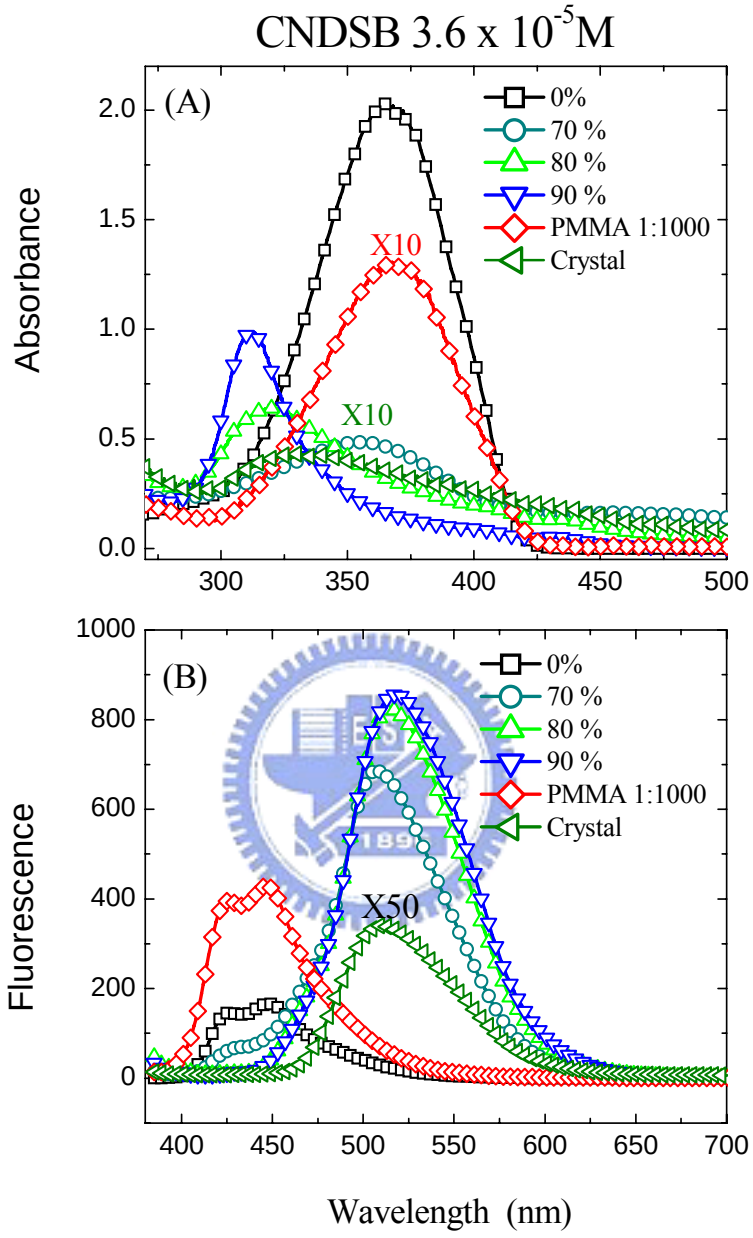

Figure 4.2: (A) UV-visible spectra of CNDSB in various water/THF mixtures, the absorbance of PMMA and single crystal film were also indicated as red and olive symbols, respectively. (B) PL spectra of CNDSB in various percentages of water/THF solutions, PMMA thin film, and single crystal film.

CN-DSB is a greenish yellow solid at room temperature. In solution, it is almost non-fluorescent. Figure 4.2 shows the characteristic UV-visible absorption spectra (Figure 4.2A) and the corresponding emission spectra (Figure 4.2B) of CN-DSB with

various percentage of added water, CN-DSB single crystal, and CN-DSB in PMMA with the ratio of 1:1000.

The absorption spectra of CN-DSB in THF solution featured with a strong absorption maximum at 366 nm. When the percentage of water reaches 70%, the absorption is blue-shifted about 10 nm with a significant decrease of the absorbance. The hypsochromic shift in absorbance is attributed to the formation of the thin, curvy nanoparticles. With the water addition, dramatic changes are observed in the absorption spectra; The absorbance increases with a large blue shift from 366 nm to 320 nm (or 310 nm) for 80 % (or 90%) water/THF solutions, and the increasing of the baseline at longer wavelengths is due to the scattering of nanoparticles.[5] Since SEM image indicated that well-evolved nanobelts are formed in 80% and 90% water/THF solutions. This considerable increase of the absorbance and much significant blue shift are attributed to the formation of nanobelts. The blue-shifted nature of the absorption of CN-DSB nanobelts resembles that observed in DPST[6] and DSB,[7,8] in which substantially decreased emission intensity is reported on the formation of nanoparticles. In contrast, we observed the greatly fluorescence enhancement of CN-DSB nanobelts. Emission of CN-DSB in THF is very weak, and clear vibronic structures is observed around 425~445 nm (Figure 4.2B). At 70% solution, these vibronic structures almost disappear and giving rise to a red-shifted emission band (~505 nm) with enhanced emission intensity. At 80 and 90% volume fractions of

[5] Li, S.; He, L.; Xiong, F.; Li, Y.; Yang, G. *J. Phys. Chem. B* **2004**, *108*, 10887.
[6] An, B.-K.; Kwon, S.-K.; Jung, S.-D.; Park, S.-Y. *J. Am. Chem. Soc.* **2002**, *124*, 14410.
[7] Egelhaaf, H. J.; Gierschner, J.; Oelkrug, D. *Synthetic Metals* **1996**, *83*, 221.
[8] Oelkrug, D.; A., T.; Gierschner, J.; Egelhaaf, H.-J.; Hanack, M.; Hohloch, M.; Steinhuber, E. *J. Phys. Chem. B* **1998**, *102*, 1902.

water addition, a highly intense emission band was observed with a maximum peak at 518 nm; the observed intensity increases with the added water and consequently with the formation of well-evolved nanobelts. For the absorbance of single crystal, the powder of CNDSB single crystal is dispersed on quartz. The result indicates that the maximum shifted to ~340 nm, and the tail at long wavelength was attributed to the scattering of powder particles. The emission of CN-DSB single crystal showed maximum peak at about 510 nm, which was similar to CN-DSB nanobelts (70%, 80% and 90%). The similarity of absorption and emission spectra between CNDSB single crystal and nanobelt indicated that the packing of nanobelts is similar to the crystal one.

To investigate how intramolecular rotation or torsional motion affects the excited-state dynamics, we prepared the thin film of CN-DSB in PMMA (1:1000). The shape of absorption spectra (Figure 4.2A) was similar to the spectra of CNDSB in THF solution, indicated that no aggregation occurred in PMMA films. In PMMA film, the PL intensity was significant enhanced, which might due to the suppression of nonradiative decay in rigid environments, which proposed by Ran Yen *et. al*.[9,10] and we will discuss later.

4.3.3 Picosecond Relaxation Dynamics of CNDSB nanobelts

In Figure 4.3, ps time-resolved fluorescence spectra of CNDSB in water/THF solution were obtained using time-correlated single-photon counting (TCSPC) system. The excitation and probing wavelength was fixed at 375 and 500 nm, respectively.

[9] Ren, Y.; Dong, Y.; Lam, J. W. Y.; Tang, B. Z.; Wong, K. S. *Chem. Phys. Lett.* **2005**, *402*, 468.
[10] Ren, Y.; Lam, J. W. Y.; Dong, Y.; Tang, B. Z.; Wong, K. S. *J. Phys. Chem. B* **2005**, *109*, 1135.

Due to the limited temporal resolution of TCSPC, a sharp spike featured the transient of CNDSB in THF solution (0%). At 70% volume of water, additional long component appeared in the transient. This result is consistent with the fluorescence enhancement at 70% water/THF solution. In 70% solution, the SEM image indicated that CNDSB molecules start to aggregate to form curvy nanobelts, thus the slow component was attributed the emission of nanobelts. In 80% and 90% solution, the sharp spike disappear, the long component that appeared in 70% become the dominant part of the transient. This result indicates that most CNDSB molecules are aggregated, and the residual nonaggregate molecules are neglectable.

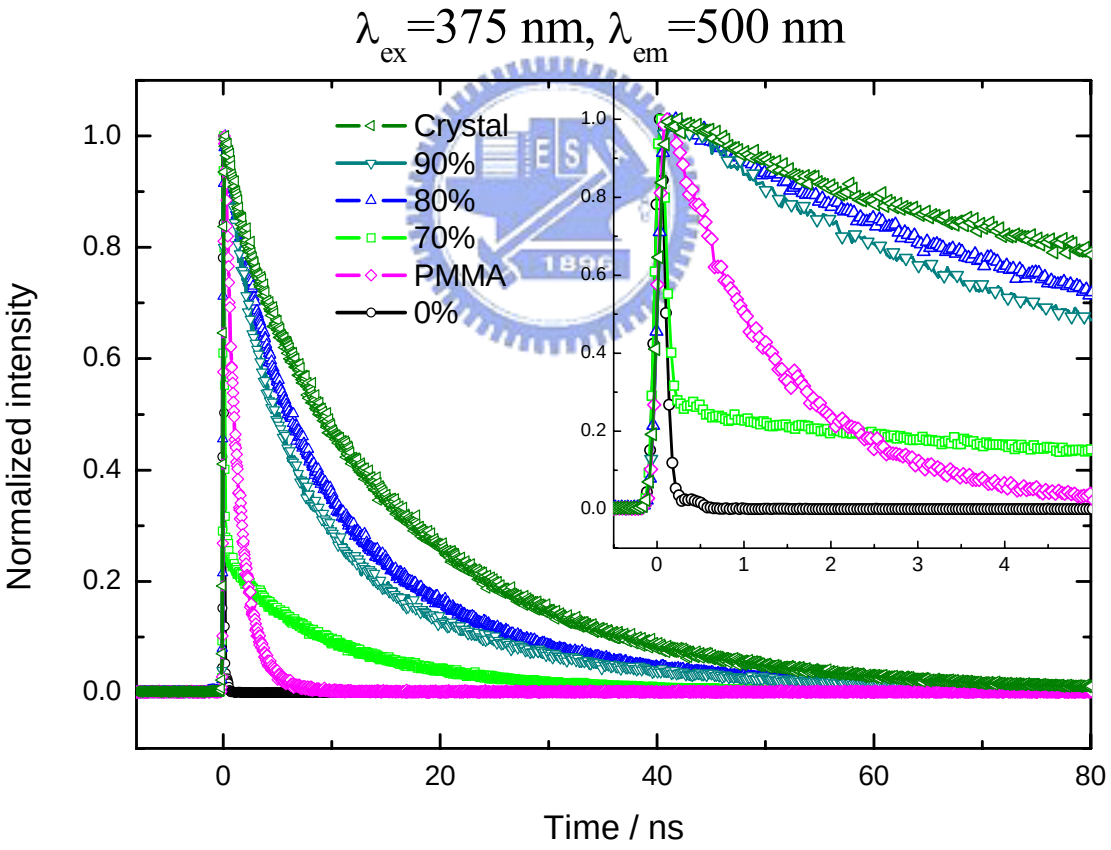

Figure 4.3: Picosecond time-resolved spectra of CNDSB in various water/THF mixtures, PMMA thin film, and single crystal obtained at λ_{ex}=375 nm, λ_{em}=500 nm. The inset was the corresponding transients in shorter time scale.

In order to avoid the interference from nonaggregate CNDSB molecules, we focused on the long decay components in 70%, 80%, and 90% solutions. Basically,

the transient can be fitted with a bi-exponential function:

$$A \xrightarrow{\tau_1} B$$
$$A' \xrightarrow{\tau_2} B' \qquad (1)$$

The deconvolution of each component is shown in Figure 4.4.

For the assignment of A and A´, we used the dual-emissive model, which we proposed previously in the study of PPB nanoparticles.[1] According to this model, two emissive states, intrinsic excitonic state and defect state exist in CNDSB nanobelts. For comparison, we measured the ps time-resolved transients of CNDSB single crystal. In Figure 4.4E, the transient of single crystal featured by a bi-exponential decay with τ_1=2.97 ns and τ_2=17.1 ns. Although τ_1 and τ_2 in single crystal are similar to that in nanobelts, the relative amplitude of τ_2 (or τ_1) differs from that in nanobelts. In signal crystal, the long component τ_2 became the dominant part of the transient. In 2003, with the application of femtosecond up-conversion microscopy, Tahara group measured the temporal resolved fluorescence transients of α -perylene microcrystal.[11] Their results indicated that the existence of the defect state in crystal would accelerate the fluorescence decay. It is reasonable for us to expect that the defects in single crystal are less than that in nanobelts. For above reason, the long component τ_2 in nanobelts or single crystal is attributed to the emission from the intrinsic excitonic state; the short component τ_1 is attributed to the emission of defect state.

[11] Fujino, T.; Tahara, T. *J. Phys. Chem. B* **2003**, *107*, 5120.

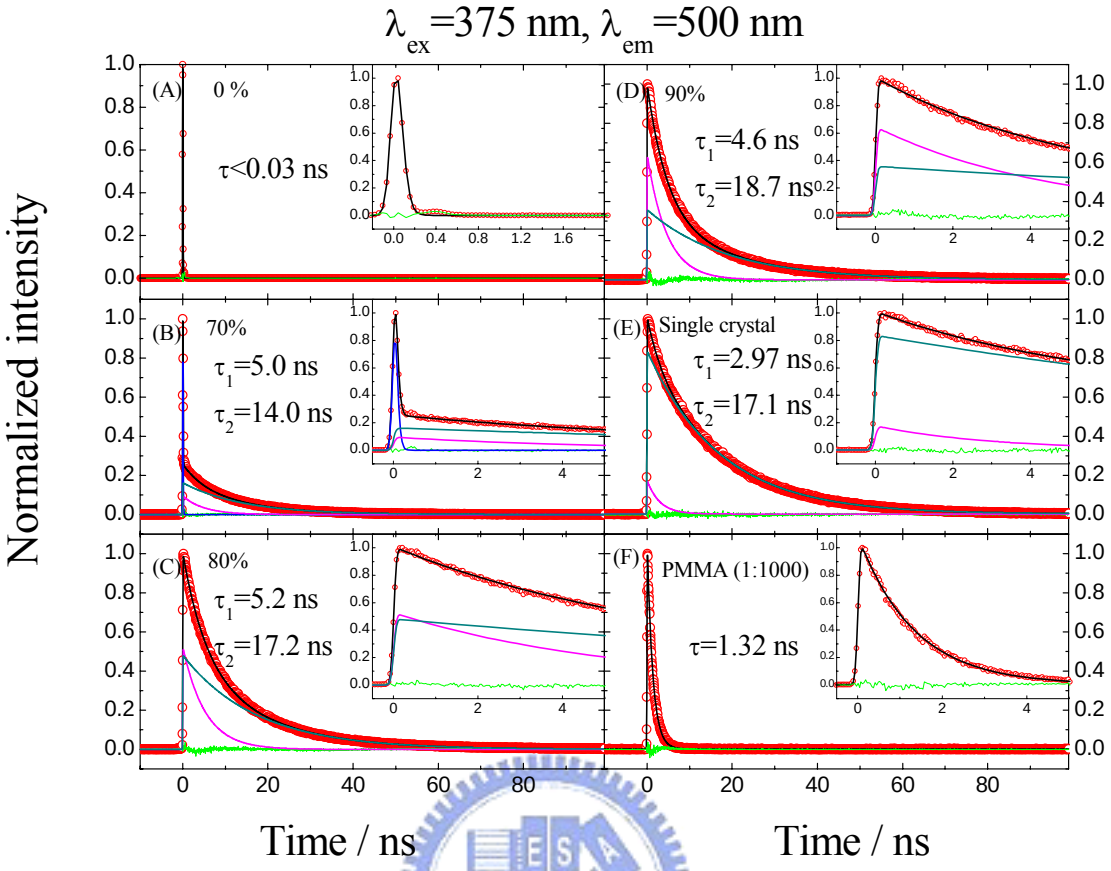

Figure 4.4: Picosecond transients of CNDSB in (A) 0%, (B) 70%, (C) 80%, (D) 90%, (E) single crystal, (F) PMMA film, each transients can be fitted with a bi-exponential function. The solid black curves are theoretical fits with residues shown as green traces; the short component was indicated as magenta line, and long component was indicated as dark cyan. The blue trace in 70% solution indicates the contribution from nonaggregate CNDSB molecules.

In Figure 4.4B, the observing τ_2 is shorter than that in 80%, 90% and single crystal. This is because the CNDSB molecules starts to aggregate to form nanoparticles at 70% solution, and the crystalline structure is not as good as those in higher percentage water/THF solutions or single crystal. The observing τ_2 is interfered by the defects in nanoparticles, thus caused the shorter lifetime we observed.

To investigate how intramolecular motion affects the excited state dynamics of CNDSB molecules, we measured the temporally resolved transients of CNDSB/PMMA films. In Figure 4.4F, the transients can be fitted by a

single-exponential decay with 1.32 ns time coefficient, which is much longer than that in THF, similar results were also observed by Yan Ren *et. al*.,[9,10] in which the lifetime of 1,1,2,3,4,5-hexaphenylsilole (HPS) increased significantly in high viscosity solvents and low-temperature glasses.

The UV and PL spectra of CNDSB in PMMA film are similar to that in THF solution. This result reveals that no aggregation and structural changes occurred in PMMA films. If the enhancement of the fluorescence quantum yield in nanobelt is only due to the structural confinement, the lifetime should close to that in PMMA film. However, in nanobelts, the lifetime is significant longer than that in PMMA films. This result indicated that structural confinement is not the only reason of fluorescence enhancement. The fluorescence enhancement in CNDSB nanobelts should contribute from both planar conformation and formation of aggregates, which has been discussed in our previous study.[1] Because of the limitation of temporally resolution, the ultrafast decay of CNDSB in THF solution could not be resolved by using TCSPC system. In order to get better understanding about the ultrafast processes, we measured the femtosecond time-resolved transients by fluorescence up-conversion technique, and the results would be shown in next section.

4.3.4 Femtosecond Relaxation dynamics of CNDSB in THF solution and nanobelts

Figure 4.5A is the typical fluorescence transient of CNDSB in THF solution. With the application of femtosecond up-conversion technique, the pulse-limited component in

TCSPC system is resolved. The transient can be fitted by a bi-exponential decay with time coefficients of 0.9 ps and 24 ps. In trans-silbene, the nonradiative process in S_1 state is dominated by the isomerization along C=C bond with an energy barrier only 3.4 kJ mol^{-1}.[12] Considering the structural similarity between trans-stilbene and CNDSB, the observed 0.9 ps decay is attributed to the twisting along C=C coordinate, which leads to an efficient $S_1 \rightarrow S_0$ internal conversion channel at perpendicularly twisted conformation. This interpretation is supported by the result of CNDSB in PMMA film (Figure 4.5B), In PMMA film, the intramolecular motion is restricted, and the isomerization channel is energetically unfavorable because of the increasing of the energy barrier, therefore the sub-picosecond component is absent. Since the solvent molecules surround solute molecule, the importance of solvent-induced vibrational relaxation (VR) should be considered. In VR process, the excess vibrational energy of the excited molecules transfer to the surrounding molecules as heat, and relaxed to the lowest vibrational sub-level. In general, the time-scale of the vibrational cooling process ranges from tens of ps to sub-ps[13] depends on the excess energy and the type of solvent molecules.[14,15] For above reason, the observing 24 ps component is attributed to the vibrational cooling process.

[12] Felker, P. M.; Zewail, A. H. J. Phys. Chem. **1985**, 89, 5420
[13] Zewail, A. H. *J. Phys. Chem. A.* **2000**, *104*, 5660.
[14] Tan, X.; Gustafson, T. L. *J. Phys. Chem. A.* **2002**, *106*, 3593.
[15] Goldie, S. N.; Blanchard, G. J. *J. Phys. Chem. A* **2001**, *105*, 6785.

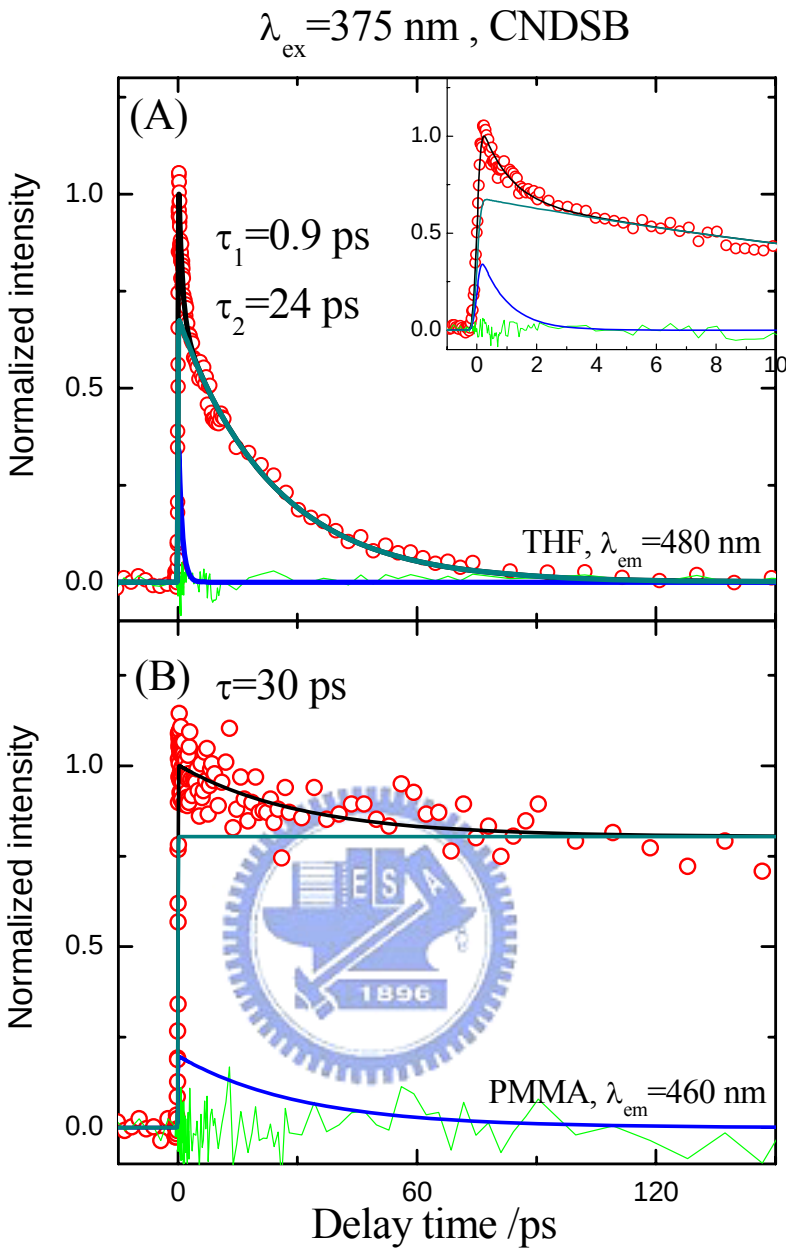

Figure 4.5: Femtosecond time-resolved spectra of CNDSB in (A) THF and (B) PMMA thin film. In each transient, the solid black curves are theoretical fits and the residues were shown as green trances. For THF solution, the transient was obtained at λ_{ex}=375 nm, λ_{em}=480 nm, and deconvoluted with bi-exponential function. The short component and long component were indicated as blue and dark cyan, respectively. For PMMA films, the transient was obtained at λ_{ex}=375 nm and λ_{em}=460 nm, and deconvoluted with bi-exponential function. The long component (dark cyan line) was fixed at the value obtaining from TCSPC technique.

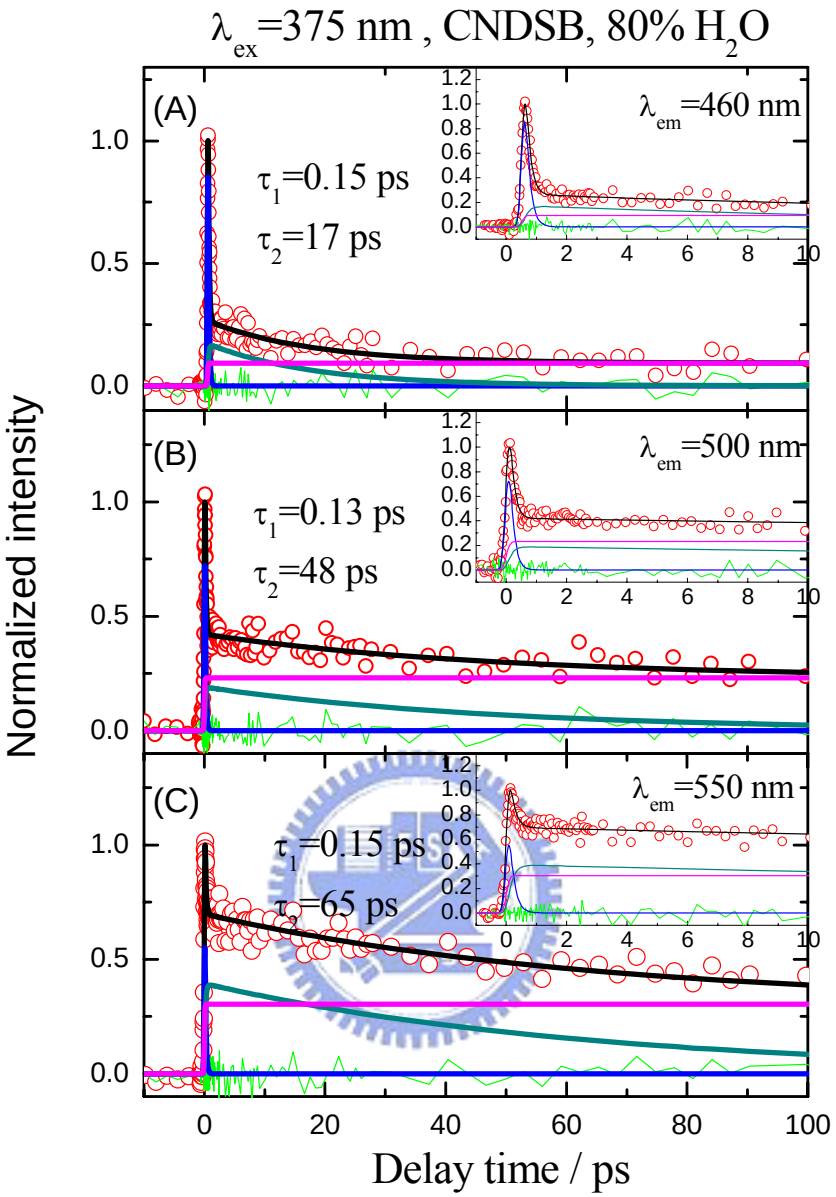

Figure 4.6: Femtosecond transients of CNDSB in 80% Water/THF solution, the excitation wavelength was fixed at 375 nm and probe at (A) 460 nm, (B) 500nm, (C) 550 nm. For each transient, at least three components were required to get the satisfactory fitting. The longest component (magenta line) was fixed at the value obtained from TCSPC result.

In Figure 4.5B the transient can be described with a 31 ps decay component, and an offset. Since similar energy transfer might also occur between CNDSB and PMMA polymer, the 30 ps component is attributed to the energy transfer process that occurred between CNDSB molecules and PMMA.

Figure 4.6 includes three typical fluorescence transients of CNDSB nanobelts probing at 460 nm, 500 nm, and 550 nm. In previous section, we have exam the fluorescence decay of CNDSB nanobelts in nanosecond time scale. In 0~100 ps range, the ns components become the offset in transient, and indicate as the magenta line. For the residual parts of the transient, a bi-exponential decay function is required to describe the transient. In generally, τ_1 is about 0.15 ps, which is wavelength independent. τ_2 varies from 17 ps to 65 ps and increases gradually with the detection wavelength. In previous study,[1] we measure the transients of PPB and DSB nanoparticles. The transient were dominated by a ~45 ps component, which was attributed to the nonradiative deactivation process through intermolecular interactions involving π -stacking of the carbon backbones. In CNDSB nanobelts, the τ_2 was attributed to the above mentioned energy transfer process, and the wavelength dependent feature indicated that this energy transfer process is more efficient for the molecules with more available energy. However, for nanobelts, an unusual ultrarapid process τ_1 is observed, which is absent in PPB and DSB nanoparticles. To verify the origin of this ultrafast component, a blank test has been done. We measured the fluorescence transient for 80% Water/THF solution at the same condition. The result (Figure 4.7A) indicated that the interference from the scattering light is small. In the other word, we also measure the fluorescence anisotropy spectra at λ_{ex}=375 nm and λ_{em}=500 nm. If the ultra-rapid component is the scattering light, r(0) should larger than 0.4, which is the theoretical value for the r(0),[16] and we should observe a pulse-limited component in anisotropy spectra.

[16] Lakowicz, J. R. *Principles of fluorescence spectroscopy*, 2 ed.; Kluwer Academic/ plenum: New York, 1999.

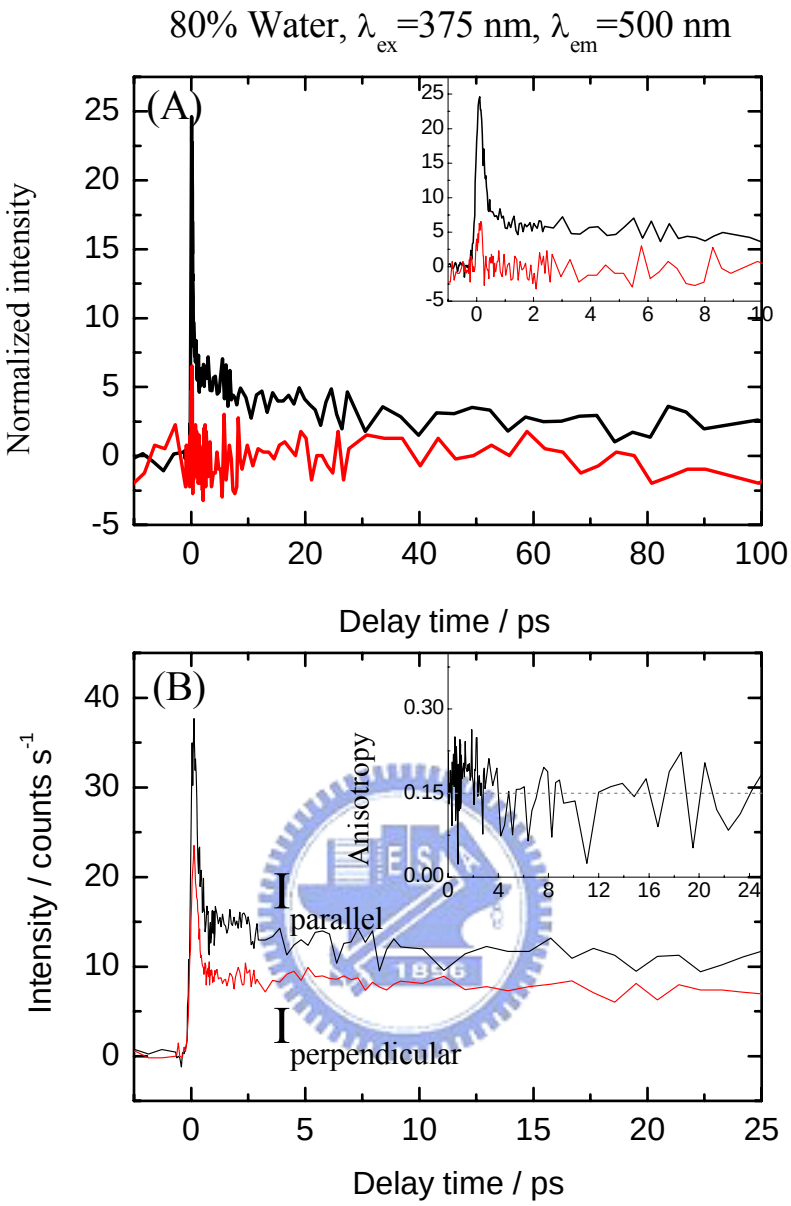

Figure 4.7: (a) The blank test of CNDSB at 80% water/THF solution: The solid black line indicated the signal of CNDSB nanobelts, and the red line was the transient of 80% water/THF solution. (b) $I_{//}$ and $I_{\perp}$ indicates the relative polarization of the collection fluorescence is parallel or perpendicular relative to the polarization of excitation beam. The anisotropy decay was calculated using the following equation:

$$r(t)=\frac{I_{//}-I_{\perp}}{I_{//}+2I_{\perp}}$$

Since we did not observe any ultrafast decay in Figure 4.7B, the result supported that the dynamic we observed is not the artificial effect. For nanoparticles, we only observed a single exponential decay, and we attributed this decay to the

intermolecular energy transfer process. Since there is no preferred direction for the energy transfer, the rate we observed is the sum of the energy transfer through any direction. However, unlike the nanoparticle, nanobelt has it own crystal axis for the grown of crystalline structure. In nanobelts, the energy transfer is anisotropic along two axes. For above reason, the τ_1 and τ_2 were attributed the energy transfer through the long and short axis, respectively.

4.4 Concluding Remarks

In the present work, by comparing the time-resolved transients of CNDSB in THF and PMMA film, the excited state dynamic of CNDSB were investigated. For CNDSB in THF, both isomerization process (0.9 ps) and vibrational relaxation (24 ps) were observed. In PMMA film, because the isomerization channel was blocked, we only observed the energy transfer process (30 ps). For single crystal, the observed bi-exponential decay was attributed to the decay of intrinsic excitonic state (17.1 ns) and defect state (2.97 ns). The optical properties of CNDSB nanobelts were also investigated. The nanobelts were prepared by reprecipation methods and characterized by SEM, pico and femtosecond time-resolved spectroscopy. The SEM results indicated that CNDSB molecules formed nanobelts as the volume fraction of the water exceed 70%, and the size of the nanobelts increases with the increase of water. In this case, the size-dependence of fluorescence lifetime is not significant, and the dual-emissive model that we proposed previously can be used to explain the excited dynamics of nanobelts very well.

For CNDSB molecules, we provided the direct evidence of that the deactivation

through intramolecular isomerization channel. The result indicated that structural confinement only contributed parts of the fluorescence enhancement in nanobelts. Both the planar conformation and formation of aggregates in nanobelts contribute parts of the fluorescence enhancement. The result of femtosecond time-resolved fluorescence spectroscopy indicated that a unique ultra-fast energy transfer process existed in CNDSB nanobelts, which is absent in nanoparticles.

Chapter 5 Hydration Dynamics of BMVC in organic solvent

5.1 Introduction

Recently, carbazole derivatives have attracted lots of attentions because of its potential to be used as light-emitting materials[1,2] and anti-tumor agents.[3,4] The large variety and flexibility in molecular synthesis makes it a good candidate to be used as a molecular probe in the biological systems.[5,6,7,8] In 2003, Chang *et. al.* synthesized a novel molecule, 3,6-bis(1-methyl-4-vinylpyridium) carbazole diiodide (BMVC, the structure is shown in Figure 5.1), which can recognize the guanine-rich quadruplex structure of DNA and has potential to be used as anti-cancer drug.[9] When BMVC dissolves in tris-HCl buffer (PH=7.5), fluorescence intensity is weak and central at ~590 nm. However, as BMVC interacted with linear duplex (LD) and quadruplex DNA (Hum24), the fluorescence intensity increased more than two orders of magnitude and the emission band blue-shifted to ~560 and ~580 nm, respectively. The excited state dynamics of carbazole derivatives (3,6-DPVTCz) with similar

[1] Wu, F.-I., Shih, P.-I., Yuan, M.-C., Dixit, A. K., Shu, C.-F., Chung, Z.-M. and Diau, E. W.-G. *J. Mater. Chem.* **2005**, *15*, 4753.
[2] Morin, J.-F., Drolet, N., Tao, Y. and Leclerc, M. *Chem. Mater* **2004**, *16*, 4619.
[3] Mann, J., Baron, A., Opoku-Boahen, Y., Johansson, E., Parkinson, G., Kelland, L. R. and Nidle, S. *J. Med. Chem.* **2001**, *44*, 138.
[4] Dias, N., Jacquemard, U., Baldeyrou, B., Tardy, C., Lansiaux, A., Colson, P., Tanious, F., Wilson, W. D., Routier, S., Mérour, J.-Y. and Bailly, C. *Biochemistry* **2004**, *43*, 15169.
[5] Pal, S. K., Zhao, L. and Zewail, A. H. *Proc. Natl. Acad. Sci.* **2003**, *100*, 8113.
[6] Pal, S. K., Zhao, L., Xia, T. and Zewail, A. H. Ibid., *100*, 13746.
[7] Pal, S. K., Peon, J. and Zewail, A. H. Ibid.**2002**, *99*, 1763.
[8] Nandi, N., Bhattacharyya, K. and Bagchi, B. *Chem. Rev.* **2000**, *100*, 2103.
[9] Chang, C.-C., Wu, J.-Y. and Chang, T.-C. *J. Chin. Chem. Soc* **2003**, *50*, 185.

structures has been investigated by Wang *et. al.*[10] Both experimental and theoretical results indicated that intramolecular motion plays an important role in determining the excited state dynamics of distyryl substituted carbazole derivatives.[10]

According to Chang's recent studies,[11] the emissive state of BMVC was attributed to the intramolecular charge transfer (ICT) state, and the charge separation occurred between carbazole moiety and methyl pyridinium cation. In general, the ICT state is a nonemissive state, and the fluorescence quantum yield is affected by both solvent polarity and environment rigidity.[12,13,14]. However, those studies were limited to the steady state measurement and nanosecond (ns) time-resolved emission spectra, and the information about the excited state dynamics is still absent.

With the application of picosecond (ps) and femtosecond (fs) time-resolved fluorescence spectra, we investigated the excited state dynamics of BMVC in tris-buffer and glycerol. For BMVC in tris-buffer, we found that the fluorescence would be quenched via the rotational induced internal conversion (IC) and intersystem crossing (ISC) processes. In other words, the fluorescence intensity of BMVC in glycerol is enhanced due to the restriction of intramolecular motion. The solvation dynamics of BMVC in those two environments is also investigated. When BMVC dissolved in tris-buffer, the solvation process deviated from that in bulk water. We believed that it is due to the interaction between water and tris-HCl molecules. In glycerol, because of the relative rigid environment, the rotational motion of solvent

[10] Wang, T.-T., Chung, S.-M., Wu, F.-I., Shu, C.-F. and Diau, E. W.-G. *J. Phys. Chem. B* **2005**, *109*, 23827.
[11] Chang, C.-C., Chu, J.-F., Kuo, H.-H., Kang, C.-C., Lin, S.-H. and Chang, T.-C. *J. Lumin.* **2006**.
[12] Shin, E.-J. and Lee, S.-H. *Bull. Korean Chem. Soc* **2002**, *23*, 1309-1314.
[13] Soujanya, T., Fessenden, R. W. and Samanta, A. *J. Phys. Chem.* **1996**, *100*, 3507.
[14] Willets, K. A., Nishimura, S. Y., Schuck, P. J., Twieg, R. J. and Monerner, W. E. *Acc. Chem. Res.* **2005**, *38*, 549-556.

molecule is restricted, and the solvation process is decelerated.

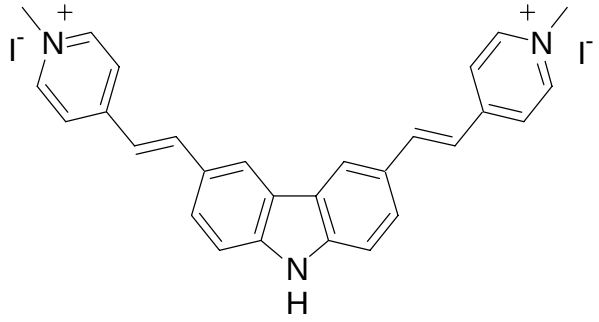

BMVC

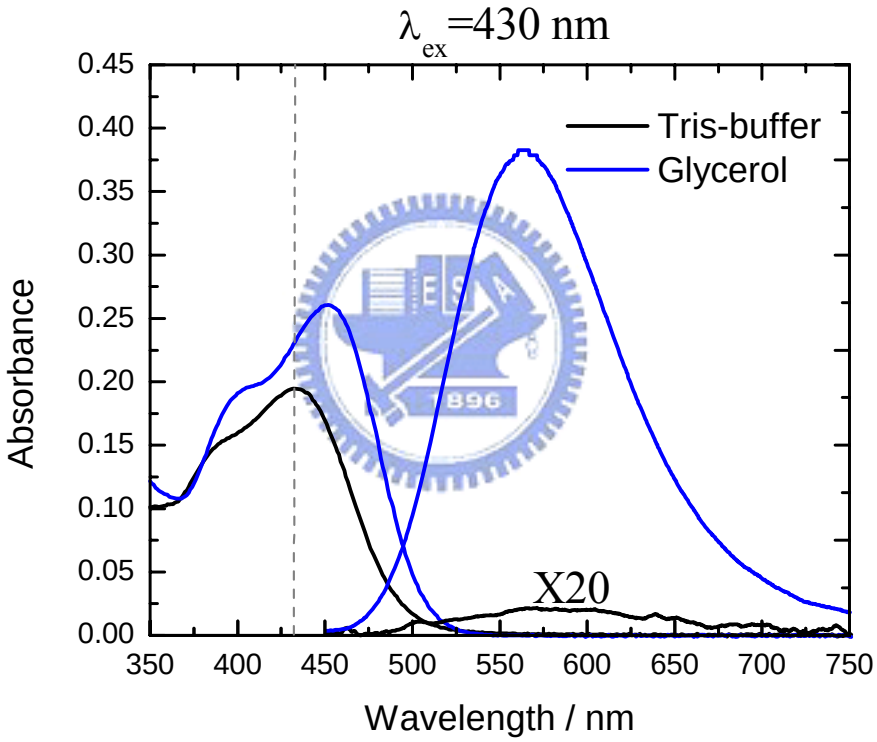

Figure 5.1: The steady state UV and PL spectra of BMVC in tris-buffer and glycerol. The concentration of each sample is fixed at $5x10^{-6}$M, and the excitation wavelength is fixed at 430 nm.

5.2 Experimental section

BMVC is synthesized through the method described elsewhere.[9] The tris-buffer solution (10 mM tris-HCl (PH 7.5) [$(CH_2(OH))_3CNH_2$], and 150 mM NaCl) are prepared and used immediately. Glycerol (99.9%) is purchased from Fisher Scientific

and used without further purification. The UV-Vis absorption spectra are recorded with CARY50 UV-Vis spectrophotometer (VARIAN). For emission spectra, the excitation light source is frequency doubled femtosecond Ti:sapphire laser, and the output wavelength is fixed at 430 nm. The fluorescence is collected by an optical fiber and introduced into charge coupled device (CCD) spectrometer (USB2000, Ocean optics). Picosecond temporally resolved spectra are obtained with a time-correlated single-photon counting (TCSPC) system (Fluotime 200, PicoQuant) as reported previously.[15]

5.3 Results and Discussion

5.3.1 Steady state spectra

Figure 5.1 is the steady state absorption and emission spectra of 5 μM BMVC in tris-buffer and glycerol. For BMVC in tris-buffer, the absorption band located at ~435 nm with a weak emission band at ~590 nm, and the total stoke shift is 6040 cm^{-1}. This result is similar to the result reported by Chang *et. al.*[11] To understand how intramolecular motion affects the excited state dynamics, we dissolved BMVC in glycerol. In glycerol, the intramolecular motion is suppressed due to its high viscosity (934 cp at 25 ^{o}C). We noticed that the absorption band is red-shifted to 450 nm. The results can be explain in two ways. From the polarity point of view. The polarity of water is larger than that of glycerol (Δf=0.32 and 0.26 for water and glycerol, respectively), the observing bathochromic shift indicated that the dipole moment of

[15] Bhongale, C. J., Chang, C.-W., Lee, C.-S. and Diau, E. W.-G. *J. Phys. Chem. B* **2005**, *109*, 13472-13478.

the excited state is small than that in ground state. Since the charge separation occurred between carbazole moiety and methyl pyridinium cation, it is reasonable for us to expect that the optical excitation will reduce the dipole moment of molecules. Second is from the structure point of view. Because the structure of BMVC is constructed by the repetition of C=C and C-C bond units, this red-shifted phenomena of the absorption spectra can be explained by the model of π-conjugated system, in which the absorption maximum would shift to long wavelength with the increasing of π-conjugation length.[16] Because the conjugation length relates with molecular geometry, this result indicates that the ground state geometry of BMVC in glycerol favors a planar structure. In glycerol, the fluoescence intensity increases dramatically, and the emission specra blue-shift to ~560 nm. The total stoke shift becomes 4370 cm^{-1}. This hypsochromic shift of the emission spectra and decrease of the Stoke shifts support that the intramolecular motion is restricted in glycerol.[10,11] Therefore, we expect that the enhancement of fluorescence intensity of BMVC in glycerol is due to the restriction of the molecular motion in high viscosity solvent.

5.3.2 Excited state dynamics of BMVC in tris-buffer

In order to get complete information about the excited state dynamics of BMVC in tris-buffer, we excite the molecules at 430 nm and probe the fluorescence decay within the range between 510nm ~640 nm. Figure 5.2A and Figure 5.2B are the typical fluorescence transients for BMVC in tris-buffer probing at 540 nm and 600 nm, respectively. Each transient is obtained by TCSPC and fluorescence

[16] Atkins, P. and Jones, L. *Chemical principles: The quest for insight*, 3; W. H. Freeman and company: New York, 2004

up-conversion technique (the data are shown in the inset). For the transients obtaining from TCSPC, at least three exponential decays are required to get a satisfactory fitting. The time-coefficient and relative amplitudes of each component are shown in Table, and the deconvolution of each component is shown in Appendix C. In Figure 5.2A, the data in the inset are obtained by fluorescence up-conversion technique, and the pulse-limited component is resolved due to its superior temporally resolution (~200 fs).

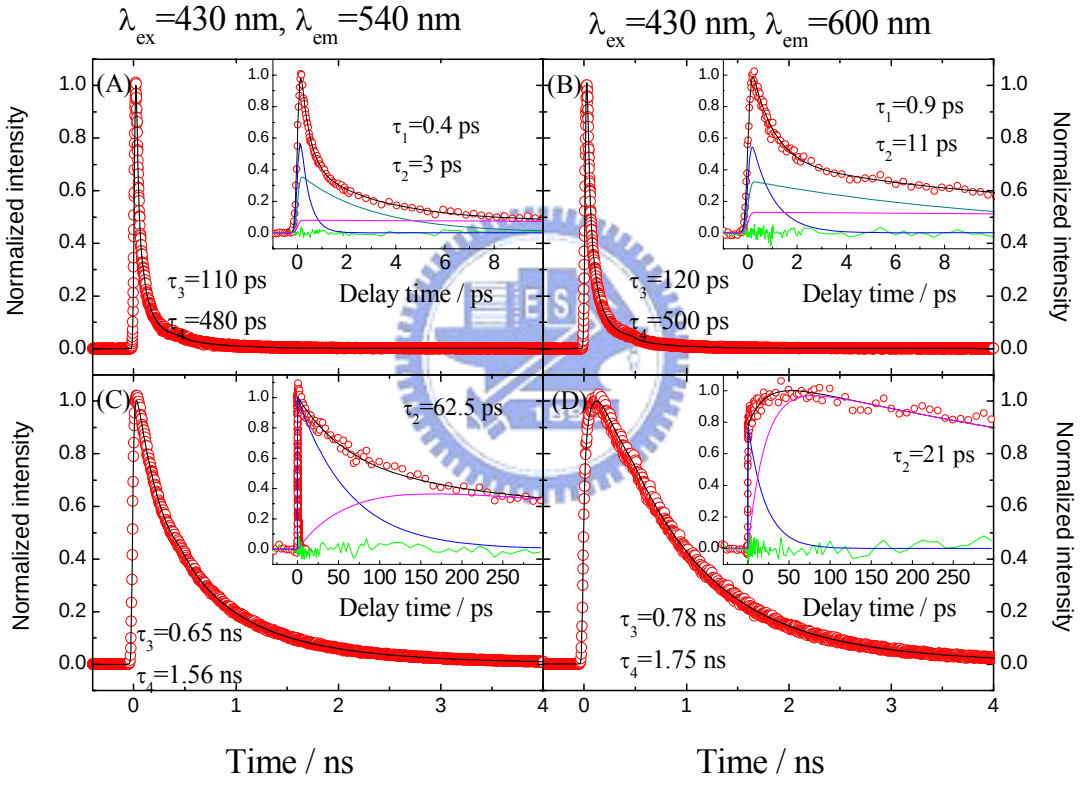

Figure 5.2: Time resolved fluorescence spectra of BMVC dissolved in tris-buffer and glycerol. The TCSPC result is shown in the main panel, and the up-conversion results in the inset. The fitting time-coefficients of each transient are shown as indicated. Figure A and B are the transients of BMVC in tris-buffer;Figure C and D are the transients of BMVC in glycerol.

Table: Fitting parameters of BMVC in tris-buffer, and glycerol. The value in brackets are the relative amplitude of each component. τ_3 and τ_4 was fixed at the value obtaining from TCSPC technique and indicated as blue color.

	510	520	530	540	550	560
BMVC in tris buffer	τ_1=0.3 ps (0.68) τ_2=1.3 ps (0.27) τ_3=90 ps (0.05) τ_4=440 ps	τ_1=0.3 ps (0.67) τ_2=1.4 ps (0.28) τ_3=90 ps (0.05) τ_4=440 ps	τ_1=0.4 ps (0.69) τ_2=2.5 ps (0.25) τ_3=100 ps (0.06) τ_4=460 ps	τ_1=0.4 ps (0.65) τ_2=3.0ps (0.29) τ_3=110 ps (0.06) τ_4=480 ps	τ_1=0.4 ps (0.67) τ_2=4.0 ps (0.26) τ_3=110 ps (0.07) τ_4=480 ps	τ_1=0.6 ps (0.70) τ_2=6.5 ps (0.21) τ_3=120 ps (0.09) τ_4=520 ps
BMVC in glycerol	τ_1= τ_2= τ_3= τ_4=	τ_1=1.2 ps (0.06) τ_2=36 ps (0.67) τ_3=510 ps (0.26) τ_4=1360 ps	τ_1= τ_2=44 ps (0.71) τ_3=590 ps (0.29) τ_4=1470 ps	τ_1= τ_2=62.5 ps (0.69) τ_3=650 ps (0.31) τ_4=1560 ps	τ_1= τ_2=82 ps (0.65) τ_3=650 ps (0.35) τ_4=1560 ps	τ_1= τ_2=152 ps (0.67) τ_3=730 ps (0.33) τ_4=1620 ps
	570	580	590	600	620	640
BMVC in tris buffer	τ_1=0.6 ps (0.74) τ_2=7.8 ps (0.20) τ_3=120 ps (0.06) τ_4=490 ps	τ_1=0.8 ps (0.74) τ_2=14 ps (0.20) τ_3=120 ps (0.06) τ_4=510 ps	τ_1=0.9 ps (0.66) τ_2=9.6 ps (0.25) τ_3=120 ps (0.09) τ_4=500 ps	τ_1=0.9 ps (0.60) τ_2=11 ps (0.29) τ_3=120 ps (0.11) τ_4=500 ps	τ_1=1.1 ps (0.54) τ_2=14 ps (0.33) τ_3=120 ps (0.13) τ_4=480 ps	τ_1=1.4 ps (0.59) τ_2=12.0 ps (0.35) τ_3=130 ps (0.06) τ_4=480 ps
BMVC in glycerol	τ_1= τ_2=127 ps (0.59) τ_3=630 ps (0.41) τ_4=1430 ps	τ_1= τ_2=5 ps (0.47) τ_3=710 ps (0.53) τ_4=1600 ps	τ_1= τ_2=15 ps (0.44) τ_3=750 ps (0.56) τ_4=1700 ps	τ_1= τ_2=21 ps (0.42) τ_3=780 ps (0.58) τ_4=1750 ps	τ_1= τ_2=28.0 ps (0.41) τ_3=790 ps (0.59) τ_4=1740 ps	τ_1= τ_2=37 ps (0.35) τ_3=800 ps (0.65) τ_4=1690 ps

For the transient obtained from up-conversion, it can be fitted with the following kinetic model:

$$I(t) = Amp1 \times e^{-t/\tau_1} + Amp2 \times e^{-t/\tau_2} + A3 \times (A_1 \times e^{-t/\tau_3} + A_2 \times e^{-t/\tau_4}) \qquad (1)$$

In this equation, A1, A2, τ_3, and τ_4 are fixed at the value of the corresponding TCSPC results, and used as a single parameter to describe the long component in the transient. For the transient probing at 510~530 nm, because of the interference of the third harmonic generation signal, an additional Gaussian is added to get the satisfactory fitting.

In our previous studies,[10] the excited state dynamics of 3,6-Distyrylcarbazole (3,6-DPVTCz) has been investigated. The structural similarity between BMVC and 3,6-DPVTCz indicates that the intrinsic process involving in the excited state of those two molecules should be similar. In 3,6-DPVTCz, both the twisting of CC single bond and CC double bond would lead to an efficient non-radiative process. The rotation of CC double bond has been extensively investigated in stilbene[17] and distyrylbenzene derivatives.[15] Those results reveal that it would lead to a barrier crossing internal conversion (IC) process. For above reason, the IC process should show a clear wavelength dependence feature. At long wavelength, the increasing of τ_1 and the decreasing of its relative amplitude strongly supported the above prediction. Therefore, τ_1 is attributed to the IC occurred via the rotation of CC double bond. After optical excitation, the excess vibration energy of the vibrationally hot molecules would dissipate to the surrounding environment. According to previous studies, the rate of vibration cooling process varied from ~ps[18,19] to tens of ps.[20,21] In general, vibration

[17] Baskin, J. S., Banares, L. and Zewail, A. H. *J. Phys. Chem.* **1996**, *100*, 11920-11933.
[18] Kropman, M. F. and Bakker, H. J. *Chem. Phys. Lett.* **2003**, *370*, 741-746.

relaxation process is strongly depended on probing wavelengthes.[20,21] Both the time scale and wavelength dependent feature of τ_2 in agree with the above-mentioned feature, hence τ_2 is assigned to the vibration relaxation. The theoretical calculation results indicated that for 3,6 DPVTCz the C-C single bond rotation would lead to a barrier-less ISC process between S_1 and triplet state.[10] Therefore, the ~110 ps component and ~480 ps component is attributed to the ISC process. However, unlike the case in 3,6-DPVTCz, which only one time-coefficient is responsible for this process. We observed a bi-exponential decay in this case. This result indicated that there might have more than one minimum in S_1 state, which is similar, to what reported by Willets *et al.*[14] In their report, they proposed that there were two local minima in S_1 state, and each minimum was responsible for the individual lifetime.

In this section, the excited-state dynamics of BMVC in tris-buffer has been studied. Nevertheless, it should be noticed that the observing transients will also be affected by the solvation process between the solute and solvent molecules.[22] For above reason, it is worthwhile to reconstruct the solvation dynamics, and the result will be shown in next section.

5.3.3 Solvation dynamics of BMVC in tris-buffer

Because of the importance in biological systems, the hydration dynamics of solute in water has been extensively investigated in past decades. In general, the hydration dynamics of water is featured with a bi-exponential function. The ultrafast component

[19] Lock, A. J. and Bakker, H. J. *J. Chem. Phys* **2002**, *117*, 1708.
[20] Assmann, J., Benten, R. V., Charvat, A. and Abel, B. *J. Phys. Chem. A* **2003**, *107*, 5291.
[21] Tan, X., Gustafson, T. L., Lefumeux, C., Burdzinski, G., Buntinx, G. and Poizat, O. Ibid.**2002**, *106*, 3593.
[22] Glasbeek, M. and Zhang, H. *Chem. Rev.* **2004**, *104*, 1929.

(<200 fs) is attributed to the libration and intermolecular vibration; the slow (~ps) component is attributed to the diffusive rotation and translation.[23] In order to compare with the above-mentioned results, we reconstructed the time resolved emission spectra. Figure 5.3A are the femtosecond time-resolved fluorescence spectra of BMVC in tris-buffer, and the probing wavelength are changed from 510 nm to 640 nm with 10 nm interval. The emission spectra at various delay times are reconstructed by using the method proposed by M. Maroncelli and G. R. Fleming.[24] The reconstructed spectra are shown in Figure 5.4A. The result indicates that the spectra gradually shift from ~530 nm to ~600nm due to the stabilization of solvent molecules. In order to obtain better quantitative description of this time-dependent Stoke shift, the spectra are fitted with a log-normal equation,[24,25] and the average peak position at various time $\bar{\nu}(t)$ can be described with the following equation:

$$\bar{\nu}(t) = \bar{\nu}(\infty) + \left[\bar{\nu}(0) - \bar{\nu}(\infty)\right] \times \left(a_1 \times e^{-t/\tau_1} + a_2 \times e^{-t/\tau_1}\right) \quad (2)$$

In which $\bar{\nu}(0), \bar{\nu}(\infty)$, and $\bar{\nu}(0)$ indicate the averaged frequency at time-zero, time = infinite, and time = t, respectively. For comparison, above equation can be rearranged and defined as a solvation correlation function C(t):[24]

$$C(t) = \left[\bar{\nu}(t) - \bar{\nu}(\infty)\right] / \left[\bar{\nu}(0) - \bar{\nu}(\infty)\right] = a_1 \times e^{-t/\tau_1} + a_2 \times e^{-t/\tau_2} \quad (3)$$

In Figure 5.4B, a bi-exponential decay function is required to describe the C(t), and the time coefficients are 0.6 ps and 1.6 ps. According to previous results,[8,26],[27] the 1.6 ps is attributed to the diffusive rotation or translation of water molecule. However, the

[23] Bagchi, B. *Annu. Rep. Prog. Chem, Sect. C* **2003**, *99*, 127.
[24] Maroncelli, M. and Fleming, G. R. *J. Chem. Phys* **1987**, *86*, 6221-6239.
[25] Siano, D. B. and Metzler, D. E. Ibid.**1969**, *51*, 1856-1861.
[26] Lu, W. Y., Kim, J. J., Qiu, W. H. and Zhong, D. P. *Chem. Phys. Lett.* **2004**, *388*, 120-126.
[27] Pal, S. K., Peon, J., Bagchi, B. and Zewail, A. H. *J. Phys. Chem. B* **2002**, *106*, 12376.

observing 0.6 ps component is significant longer than the corresponding component in bulk water. Dong-Ping Zhong group has reported the similar results,[26] in which the retardation of the ultrafast component is caused by the water molecules between solute and proximate solutes (tris-HCl).

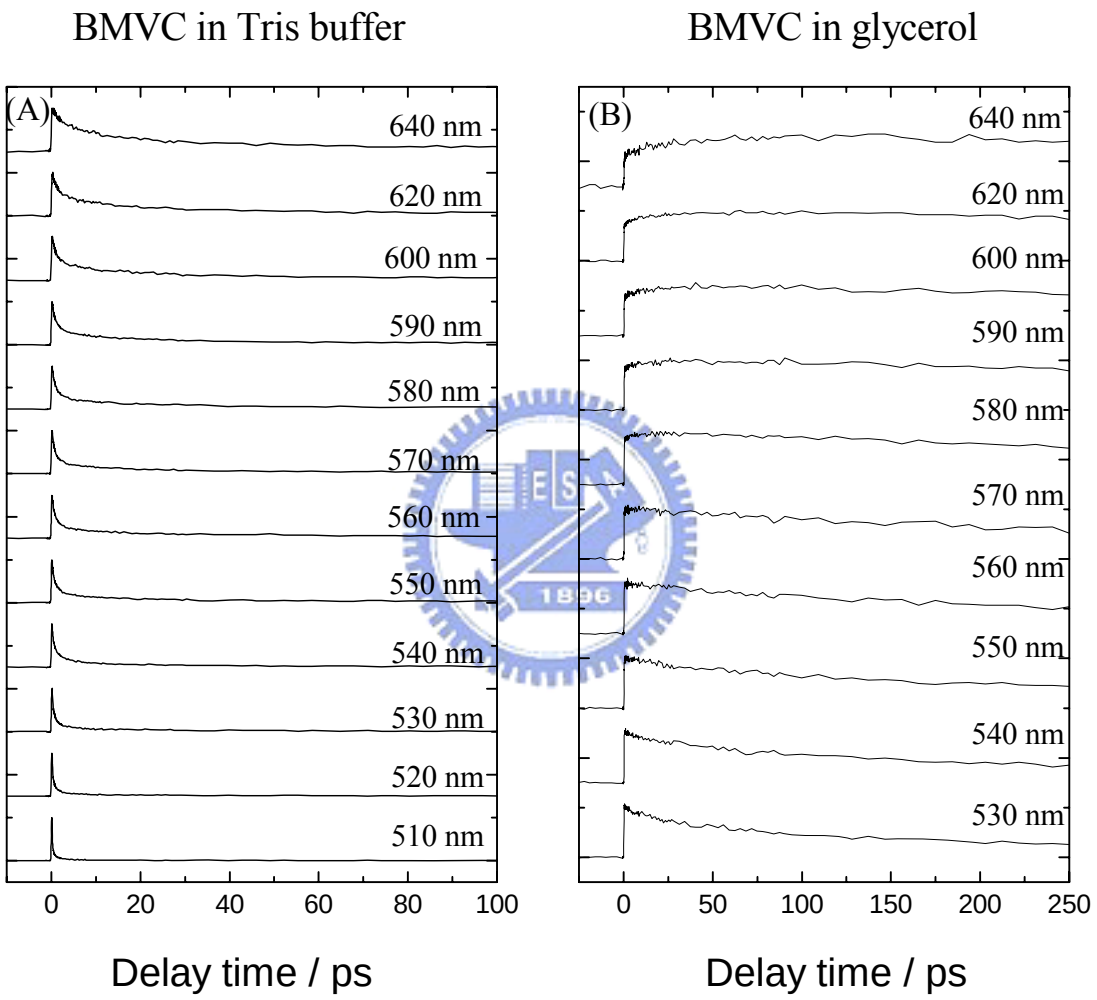

Figure 5.3: (A) Femtosecond time-resolved spectra of BMVC in tris-buffer with λ_{ex}=430 nm, and probing wavelength varied from 510 nm to 640 nm. (B) Femtosecond time resolved spectra of BMVC in glycerol with λ_{ex}=430 nm, and probing wavelength varied from 530 nm to 640 nm.

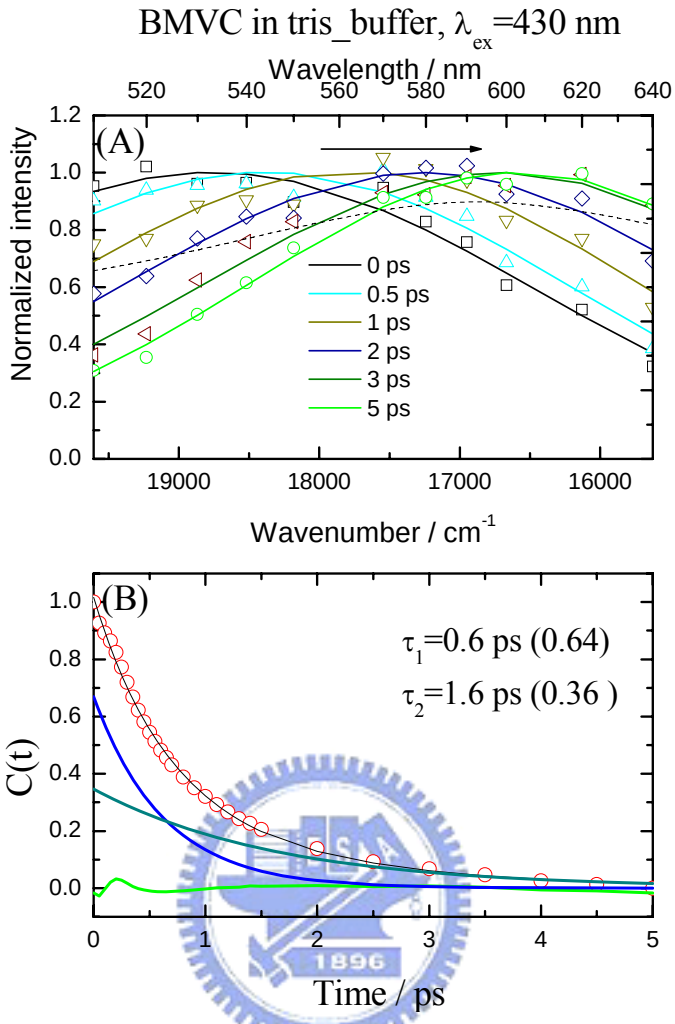

Figure 5.4: (A) The reconstructed time-resolved emission spectra of BMVC in tris-buffer. The row data at each delay time were shown as scatter and the fitted curves as solid curves. Steady state spectrum was indicated at dash line. (B) The C(t) value of BMVC in tris-buffer. Time coefficients were obtained by fitted the curve with bi-exponential model. The two components were indicated as blue and dark cyan curves, and the residual was indicated as green line.

5.3.4 Excited state dynamics and solvation dynamics of BMVC in glycerol

Figure 5.2C and Figure 5.2D are the typical fluorescence transients of BMVC in glycerol. The probing wavelength is fixed at 540 nm and 600 nm, respectively. In both wavelengths, the excitation wavelength is fixed at 430 nm. It is obvious that the fluorescence lifetime of BMVC in glycerol is longer than that in tris-buffer. This

result is in agreement with the steady state observation, in which the fluorescence intensity is enhanced in glycerol. In this case, the TCSPC results need to be fitted with three components. As the probing wavelengths varied from 540 nm to 600 nm, the initial decay part becomes a rise. The residual part of transient can be fitted with a bi-exponential function with time coefficient varied form 500~800 ps and 1.4 ns~1.8 ns. For up-conversion results (the transient in inset), the initial rise and decay feature are resolved, and the transients can be described with the following kinetic model:

$$\begin{aligned} A &\xrightarrow{\tau_2} B \xrightarrow{\tau_3} C \\ A' &\xrightarrow{\tau_2} B' \xrightarrow{\tau_4} C' \end{aligned} \qquad (4)$$

In this model, the relative amplitudes and time coefficients of τ_3 and τ_4 are fixed at the value obtained from TCSPC technique, and used to describe the slow decay and offset. A and A' indicate the BMVC with different geometries; B and B' represent the BMVC molecules at S_1 minimum. For BMVC in tris-buffer, the excited-molecule would be quenched via the rotational induced IC channel. In glycerol, this rotational motion would be restricted due to the high viscosity of glycerol, and the rate of IC would be decreased. However, we still observed an addition 1.2 ps component at 520 nm. Therefore, the 1.2 ps component at 520 nm is attributed to the IC conversion process. At the wavelength longer than 520 nm, because we probe the molecule with less available energy, the 1.2 ps component is absent. In the range between 520 nm and 570 nm, the observing τ_2 increases from 36 ps to 152 ps, and the relative amplitude decreases correspondingly. At the probing wavelength longer than 580 nm,

the probing window sets at the relative cold position, hence the decay component at 530~570 nm becomes a rise in this region. These rise and decay features are similar to the general solvation phenomena. Finally, the observed τ_3 and τ_4 are one order of magnitude longer than that in tris-buffer. In this case, the barrier of the molecule rotation increases due the high viscosity. If the molecular rotation is totally suppressed, the τ_3 and τ_4 can be expected as the radiative lifetime of BMVC with different structures. Otherwise, τ_3 and τ_4 can be attributed to the rotational induced ISC process, and it is reasonable for us to expect the retardation of those two processes in high viscosity solvent.

In Figure 5.3B, we also show the time-resolved spectra of BMVC in glycerol, and the probing wavelengths are varied from 530 nm to 640 nm. The reconstructed emission spectra at various delay time are shown in Figure 5.5A, and the corresponding C(t) value is shown in Figure 5.5B. The result in Figure 5.5A indicates that the solvation process is not complete within the range between 0~100 ps. Therefore, we also reconstructed the solvent response function C(t), by TCSPC technique (data are shown in appendix D) and the 590 ps component in Figure 5.5B is fixed at the value obtaining from TCSPC technique. In Figure 5.5B, the initial decay of the C(t) is dominated by a ~18 ps decay, and the 590 ps component is shown as an offset. According to previous results, the diffusive rotation component in solvation process will be decelerated with the increasing of solvent viscosity.[28,29,30,31,32] For

[28] Zhang, Y. and Berg, M. A. *J. Chem. Phys* **2001**, *115*, 4231.
[29] Simon, J. D. *Pure&Appl. Chem.* **1990**, *62*, 2243.

above reason, we expect that the observing 590 ps decay is due to the diffusive rotation motion of glycerol molecules, and the 18 ps component is attributed to the local motion of the OH group or intermolecular vibration.

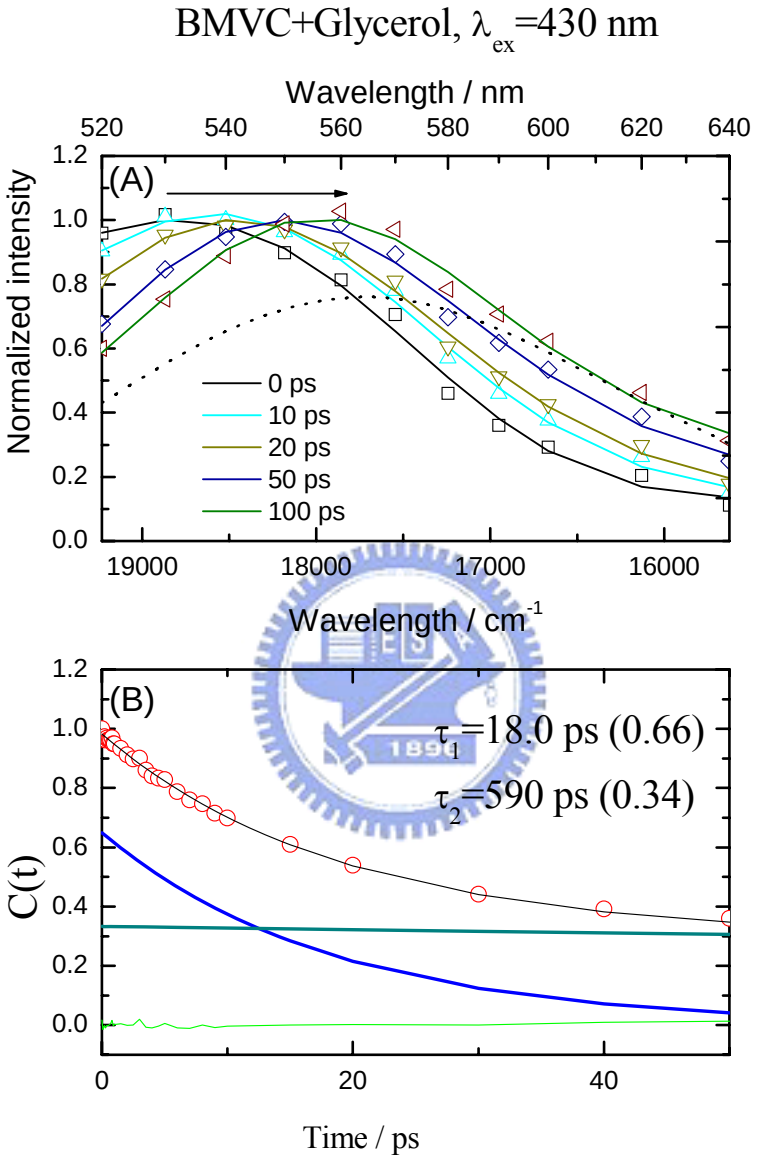

Figure 5.5: (A) The reconstructed time-resolved emission spectra of BMVC in glycerol. The row data at each delay time and the fitted curves were shown as scatter and solid curves, respectively. Steady state spectrum was indicated at dash line. (B) The C (t) value of BMVC in glycerol. The time coefficient was obtained by fitted the curve with bi-exponential model. The two components were indicated as blue and dark cyan curves, and the residual was indicated as green line.

---

[30] Zhang, Y., Jiang, J. and Berg, M. A. *J. Chem. Phys* **2003**, *118*, 7534.
[31] Zhang, Y., Sluch, M. I., Somoza, M. M. and Berg, M. A. Ibid.**2001**, *115*, 4212.
[32] Zhang, Y. and Berg, M. A. Ibid., 4223.

5.4 Concluding Remarks

In this study, the excited-state dynamics of BMVC in tris-buffer has been investigated. After initial excitation, a rotational induced IC competed with the solvent induced vibration relaxation. Because IC process is much faster (0.3~1.5 ps) than vibration relaxation (1.3 ps~12 ps), most of the excited-state populations are quenched by IC process. However, there still are small parts of molecules relaxing to S_1 minimum and returning to ground state via a rotational induced ISC channel with time coefficients of ~130 ps and ~480 ps. For BMVC in glycerol, the above-mentioned non-radiative process is suppressed by the high viscosity of glycerol. Therefore, the rate of rotational IC and ISC process is decreased, which results in the fluorescence enhancement we observed in steady state measurement. The solvation dynamic of BMVC in tris-buffer and glycerol are also studied. In tris-buffer, the biphasic nature of solvation correlation function is similar to the well-known solvation process in bulk water. However, because of the interaction between water molecules and tris-HCl, the observed dynamics (0.6 ps and 1.6 ps) is longer than that in bulk water. For BMVC in glycerol, the dramatic decrease of the solvation rate indicated that the high viscosity suppressed the rotation of the solvent molecule. The solvent-dependent solvation dynamics indicated that it could be used in probing the local environment of the solute molecules.

Chapter 6 Hydration dynamics of BMVC in duplex and quadruplex DNA

6.1 Introduction

Telomeres, the end of chromosomes, has been extensively studied because its importance in biological systems.[1,2,3,4] During replication, the length of telomeres decreased each cycle. Once the length of telomere shorten to certain extent, the cell stops replication and results in cellular senescence.[5,6,7,8] In tumor cells, the length of telomere is maintained by telomerase, which leads to the abnormal overgrowth and immortalization of cancer cells.[9,10,11] For above reason, the research about the interaction between telomere and telomerase has received large attention in past few years.[12,13,14] In more than 85% of human tumor cells, the activity of telomerase increased significantly, and the inhibition of the activity of telomerase is thought to be

[1] Blackburn, E. H. and Greider, C. W. *Telomeres*; Cold Spring Harbor Laboratory press: New Work, 1996
[2] Blackburn, E. H. *Annu. Rev. Biochem.* **1984**, *53*, 163.
[3] Williamson, J. R. *Annu. Rev. Biophys. Biomol. Struct.* **1994**, *23*, 703.
[4] Colgin, L. and Reddel, R. *Current Biology* **2004**, *14*, R901.
[5] Harley, C. B. and Futcher, A. B. *Nature* **1990**, *345*, 458.
[6] Lundblad, V. and Szostak, J. W. *Cell* **1989**, *57*, 633.
[7] Sandell, L. L. and Zakian, V. A. Ibid.**1993**, *75*, 729.
[8] Harley, C. B. and Villeponteau, M. P. *Curr. Opin. Genet. Dev.* **1995**, *5*, 249.
[9] Greider, C. W. and Blackburn, E. H. *Cell* **1987**, *51*, 887.
[10] Feng, J., Funk, W. D., Wang, S.-S., Weinrich, S. L., Avilion, A. A., Chiu, C.-P., Adams, R. R., Chang, E., Allsopp, R. C., Yu, J., Le, S., West, M. D., Harley, C. B., Andrews, W. H., Greider, C. W. and Villeponteau, B. *Science* **1995**, *269*, 1236.
[11] Hahn, W. C., Counter, C. M., Lundberg, A. S., L., B. R., Brooks, M. W. and Weinberg, R. A. *Nature* **1999**, *400*, 464.
[12] Blackburn, E. H. Ibid.**1991**, *350*, 569.
[13] Breslow, R. A., Shay, J. W., Gazdar, A. F. and Srivastava, S. J. *J. Natl. Cancer Inst.* **1997**, *89*, 618.
[14] Mergny, J. L. and Hélène, C. *Nat. Med.* **1998**, *4*, 1366.

a potential cancer therapy.[15] According to previous studies, the formation of quadruplex structure in telomeric 3´-overhang repeats could inhibit the activity of telomerase,[16,17] and the interaction between telomerase and quadruplex structure has became more and more important. However, the existence of quadruplex structure in native human telomeres in vivo has not been verified and became a challenging question.[18] In 2003, C.-C. Chang *et. al.* synthesized a novel fluorescence biomarker: 3,6-bis(1-methyl-4-vinylpyridinium) carbazole diiodide (BMVC), which can interact and recognize the linear duplex and quadruplex structures of DNA.[19] With the application of BMVC, the existence of the quadruplex structure in native human telomeres was demonstrated for the first time.[20]

In their studies, when BMVC is dissolved in tris-buffer, the fluorescence intensity is weak and central at ~590 nm. On the other word, when the molecule interacted with linear duplex and quadruplex DNA, the fluorescence intensity increased more than two order of magnitude and the emission band blue-shifted to ~560 and ~580 nm, respectively.[20] However, the studies of C. C. Chang *et. al*. are limited on steady state measurement and ns time-resolved emission spectra. With the application of femtosecond and picosecond time resolved fluorescence spectroscopy, the excited state dynamics of BMVC molecule has been investigated and reported in previous chapter. The result reveals that intramolecular motion would lead to an efficient non-radiative process. This process would be suppressed by the high viscosity of

[15] Brunori, M., Luciano, P., Gilson, E. and Geli, V. *J. Mol. Med.* **2005**, *4*, 4.
[16] Zahler, A. M., Williamson, J. R., Cech, T. R. and Prescott, D. M. *Nature* **1991**, *350*, 718.
[17] Neidle, S. and Parkinson, G. N. *Nat. Rev. Drug Discovery* **2003**, *1*, 383.
[18] Neidle, S. and Parkinson, G. N. *Curr. Opin. Struct. Biol.* **2003**, *13*, 275.
[19] Chang, C.-C., Wu, J.-Y. and Chang, T.-C. *J. Chin. Chem. Soc* **2003**, *50*, 185.
[20] Chang, C.-C., Kuo, I.-C., Ling, I.-F., Chen, C.-T., Chen, H.-C., Lou, P.-J., Lin, J.-J. and Chang, T.-C. *Anal. Chem.* **2004**, *76*, 4490.

glycerol. In this article, we focus on the specific interaction between BMVC and different types of DNA (linear duplex and quadruplex). In this studies, BMVC interacted with linear duplex DNA(LD) and Human quadruplex DNA(Hum 24). The result indicated that for BMVC/LD and BMVC/Hum24 complexes, BMVC is buried into a relative non-polar environment, and the restriction of intramolecular motion plays an important role in the fluorescence enhancement. Solvation dynamics are also investigated, we found that the solvation processes of BMVC in those two types of DNA are different, and the results would be discussed in following section.

6.2 Experimental section

BMVC molecules are synthesized and purified using the method that described elsewhere.[19] The tris-buffer solution of 10 mM Tris-HCl ($CH_2(OH))_3CNH_2$PH 7.5) and 150 mM NaCl are prepared and used immediately. All oligonucleotides are purchased from Applied Biosystems. DNA samples are mixed with the tris-buffer solution and heated to 90ºC for 5 mins. After heated, the solution cooled to room temperature and stored at 4ºC more than 24 hours before using. The UV-Vis absorption spectra are recorded with CARY50 UV-Vis spectrophotometer (VARIAN). In emission spectra, excitation light source is frequency doubled femtosecond laser, and excitation wavelength fixed at 430 nm. The fluorescence is collected by an optical fiber and introduced into charge coupled device spectrometer (USB2000, Ocean optics). Picosecond temporally resolved spectra are obtained with a time-correlated single-photon counting (TCSPC) system (Fluotime 200, PicoQuant) as reported

previously.[21] Femtosecond relaxation dynamics of the system are measured by fluorescence up-converted system (FOG100, CDP) in combine with a mode-locked Ti:sapphire laser as describe elsewhere.[22]

6.3 Results and discussion

6.3.1 Steady state spectra

The steady state absorption and fluorescence spectra of BMVC in tris-buffer, LD and Hum24 are presented in Figure 6.1. The concentration of BMVC , LD and Hum 24 are fixed at 5 μM. In tris-buffer, the absorption maximum located at 435nm. However, as BMVC interacted with LD and Hum24, the absorption shifted to 450nm and 470 nm, respectively. For π-conjugate system, the absorption wavelength increases with the increasing of conjugation length, and the planar structure would increase the effective conjugation length of the molecules.[23,24] This result indicates that the ground state geometry of BMVC in Hum 24 is relative planar than that of LD and tris-buffer. In Figure 6.1, the emission spectra of BMVC in tris-buffer, LD, and Hum24 are indicated by dash line with different color. For BMVC in tris-buffer, the fluorescence of BMVC is weak and central at ~590 nm. When BMVC interacted with LD and Hum24, the fluorescence intensity increased more than two orders of magnitude, and this result has been reported by Chang *et. al.*[19,25] On the other words,

[21] Bhongale, C. J., Chang, C.-W., Lee, C.-S. and Diau, E. W.-G. *J. Phys. Chem. B* **2005**, *109*, 13472-13478.
[22] Lu, Y.-C., Chang, C.-W. and Diau, E. W.-G. *J. Chin. Chem. Soc* **2002**, *49*, 693.
[23] Kuhn, H. and Försterling, H.-D. *Principles of physical chemistry*; Wiley: Chichester, 2000
[24] Atkins, P. and Jones, L. *Chemcial principles: The quest for insight*, 3; W. H. Freeman and company: New York, 2004
[25] Chang, C.-C., Wu, J.-Y., Chien, C.-W., Wu, W.-S., Liu, H., Kang, C.-C., Yu, L.-J. and Chang, T.-C. *Anal. Chem.* **2003**, *75*, 6177.

we also observed the decreasing of the stoke shift when BMVC interacted with LD (4060 cm^{-1}) and Hum24 (3900 cm^{-1}). Similar results are also observed when BMVC dissolved in high viscosity solvent (glycerol). In high viscosity solvent, the molecule can not relax to the minimum of S_1 state because the restriction of intramolecular motion, and the fluorescence was emitted from the non-relax state. Therefore we observed the decreasing of the stoke-shift. Since we observed similar decreasing of the stoke-shift, this result supported that in BMVC/LD and BMVC/Hum24 complex, the intramolecular motion is also restricted.

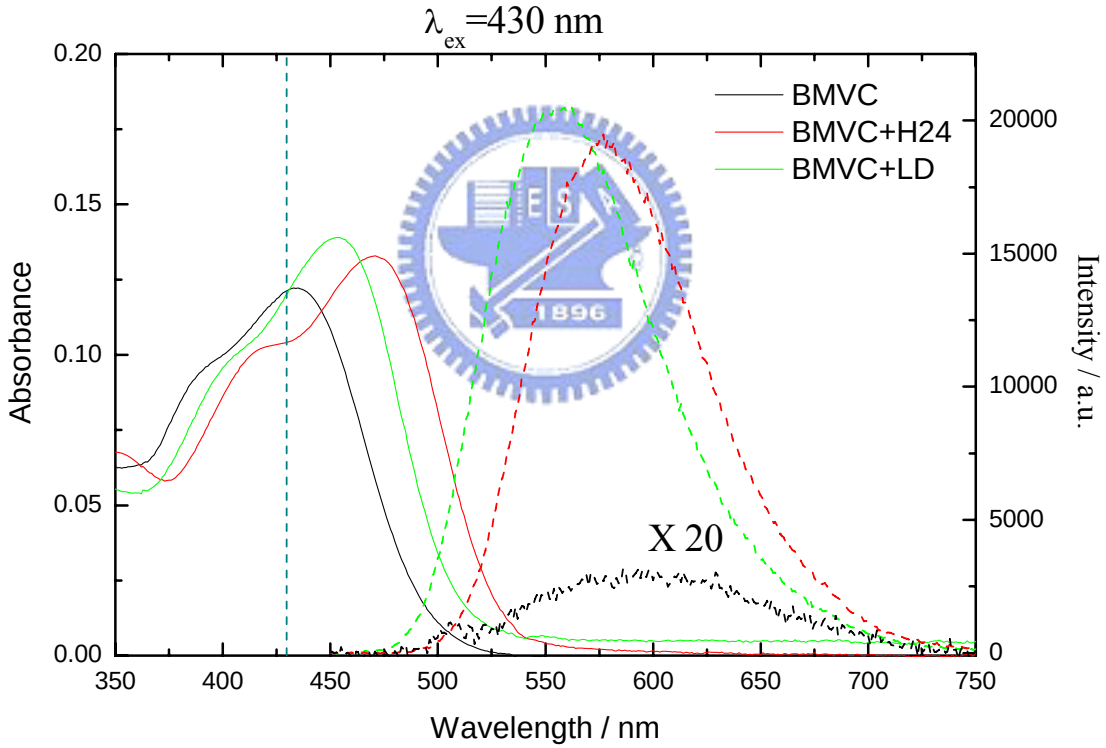

Figure 6.1: Steady state spectrum of BMVC and BMVC interacted with LD and Hum24 DNA. The concentration is fixed at 5×10^{-6} M, and the excitation wavelength was indicated as gray dash line.

6.3.2 Time-resolved fluorescence measurement

The time resolved fluorescence of BMVC in tris-buffer has been reported in

previous section. In high viscosity solvent (glycerol), the fluorescence lifetime increases due to the restriction of intramolecular motion. For comparison, similar measurement was performed as BMVC interacted with LD and Hum24 DNA. Figure 6.2 is the typical fluorescence transients of BMVC interacted with LD and Hum24 DNA. For comparison, the transient of BMVC in tris-buffer is also demonstrated. It is evident that the fluorescence lifetime increases significant due to the interaction between BMVC and DNA macromolecule. The time-resolved measurement supported that the interaction between BMVC and DNA would restrict the intramolecular motion, and caused the increasing of the fluorescence lifetime.

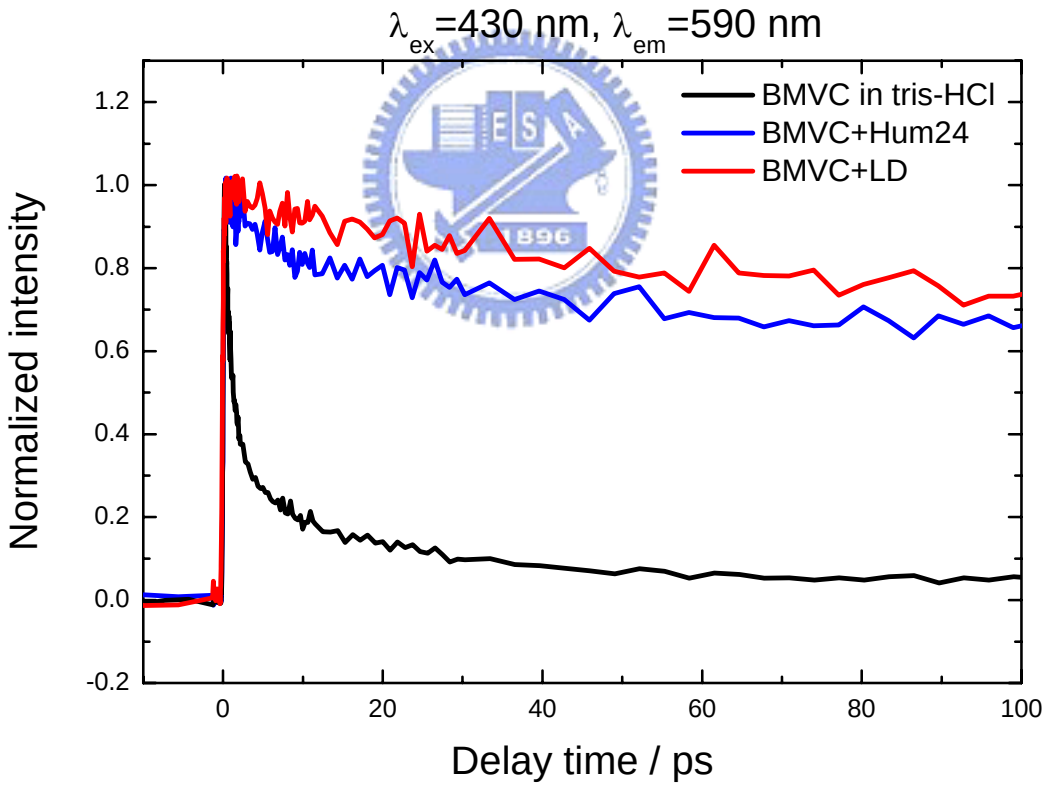

Figure 6.2: The femtosecond time-resolved spectra of BMVC in tris-buffer, and BMVC interacted with LD and Hum24 DNA. The excitation was fixed at 430 nm, and the probing wavelength was fixed at 590 nm

6.3.3 Fluorescence anisotropy measurement

When BMVC is mixed with LD and Hum 24, another important issue is the percentage of BMVC interacted with DNA. A useful tool is the temporally-resolved fluorescence anisotropy measurement, which can observe the rotational Brownian motion of the chromophore.[26,27] According to Perrin's equation, the rotation diffusion coefficient is inversed proportional to the hydrodynamic molecular volume of fluorophore.[26] Therefore, the anisotropy decay of interact and non-interact molecule is quite different. In TCSPC experiment, the anisotropy decay can be calculated with the following equation:

$$r(t) = \frac{I_{VV}(t) - G \times I_{VH}(t)}{I_{VV}(t) + 2 \times G \times I_{VH}(t)} \quad (1)$$

I_{VV} and I_{VH} represent the intensity of fluorescence which excite with vertically polarized light and monitor at vertical and horizontal polarization, respectively. G indicates the G-factor of monochromator. Figure 6.3 is the results obtained by TCSPC technique. In Figure 6.3A, the anisotropy decay of BMVC in tris-buffer can be fitted with a 0.37 ns decay. However, we also observed a long component (11.2 ns). Because the fluorescence decay of BMVC in tris-buffer is not long enough for us to observe the 11.2 ns anisotropy decay, the 11.2 ns component might be caused by the artificial effect. Figure 6.3B and Figure 6.3C are the fluorescence anisotropy decay of BMVC+Hum24 and BMVC+LD, respectively. In those two Figures, the anisotropy decay increases from 370 ps to 4.4 ns (Hum24) and 5.3 ns (LD). This result indicates

[26] Valeur, B. *Molecular Fluorescence:principles and applications*; WILEY-VCH: New York, 2002
[27] Lakowicz, J. R. *Principles of fluorescence spectroscopy*; Kluwer Acaademic/Plenum Publishers: New York, 1999

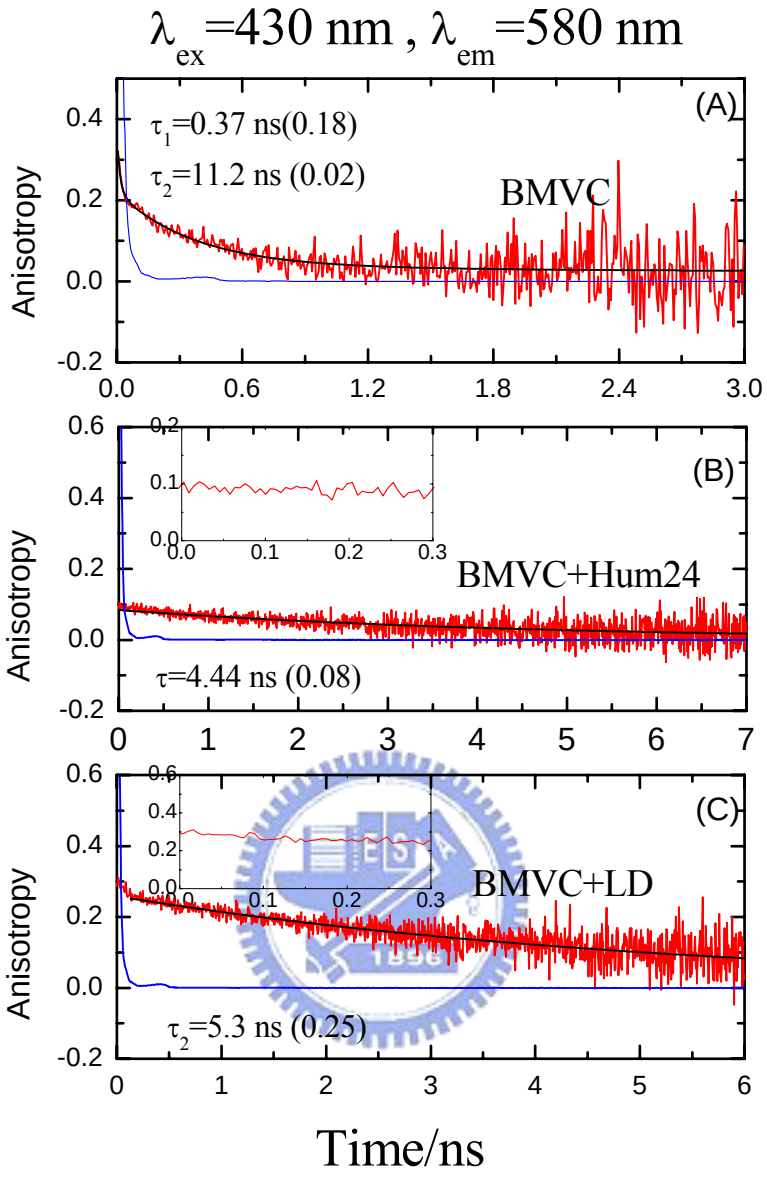

Figure 6.3: Fluorescence anisotropy decay of BMVC at various environments. The anisotropy was reconstructed using the TCSPC results, and the instrument response function is indicated as blue line. (A) BMVC in tris-buffer; (B) BMVC+Hum24; (C) BMVC+LD

that BMVC is connected with the DNA macromolecules, and the increase of the anisotropy time is attributed to the increase of the hydrodynamic volume.

Similar anisotropy measurement is also performed using fluorescence up-conversion technique. For up-conversion experiment, r(t) can be calculated with the following equation:

$$r(t) = \frac{I_{//}(t) - I_{\perp}(t)}{I_{//}(t) + 2I_{\perp}(t)} \quad (2)$$

The polarization of the probe beam is fixed at horizontal, $I_{//}$ and $I_{\perp}$ indicated the relative polarization of excitation beam at parallel and perpendicular direction, respectively.

In Figure 6.4A, the anisotropy decay can be fitted with a bi-exponential function. The fast component is 32 ps and the other one is fixed at the value obtained from TCSPC. Because not only the rotational Brownian motion but also the segmental motion would cause the depolarization of fluorescence, the 32 ps component is attributed to the segmental motion of molecules. However, in the anisotropy decay of BMVC/LD and BMVC/Hum24 complexes we do not observe any fast component in the range between 0~300 ps. This result indicates that the segmental motion of BMVC is restricted due to the interaction between BMVC and DNA and the amount of non-interact BMVC molecules is undetectable.

6.3.4 Hydration dynamics of BMVC/LD complex

Figure 6.5A is the typical fluorescence transients of BMVC/LD complex. The excitation wavelength is fixed at 430 nm and probed at 540 nm, 600 nm, and 640 nm. On the blue edge of spectra the signal decays with multi-exponential components at different time scale, whereas on the red edge of spectra a significant rise component is observed. In order to reconstruct the time-resolved emission spectra (TRES), we measured the transient with 10 nm interval in the range between 520 nm and 640 nm.

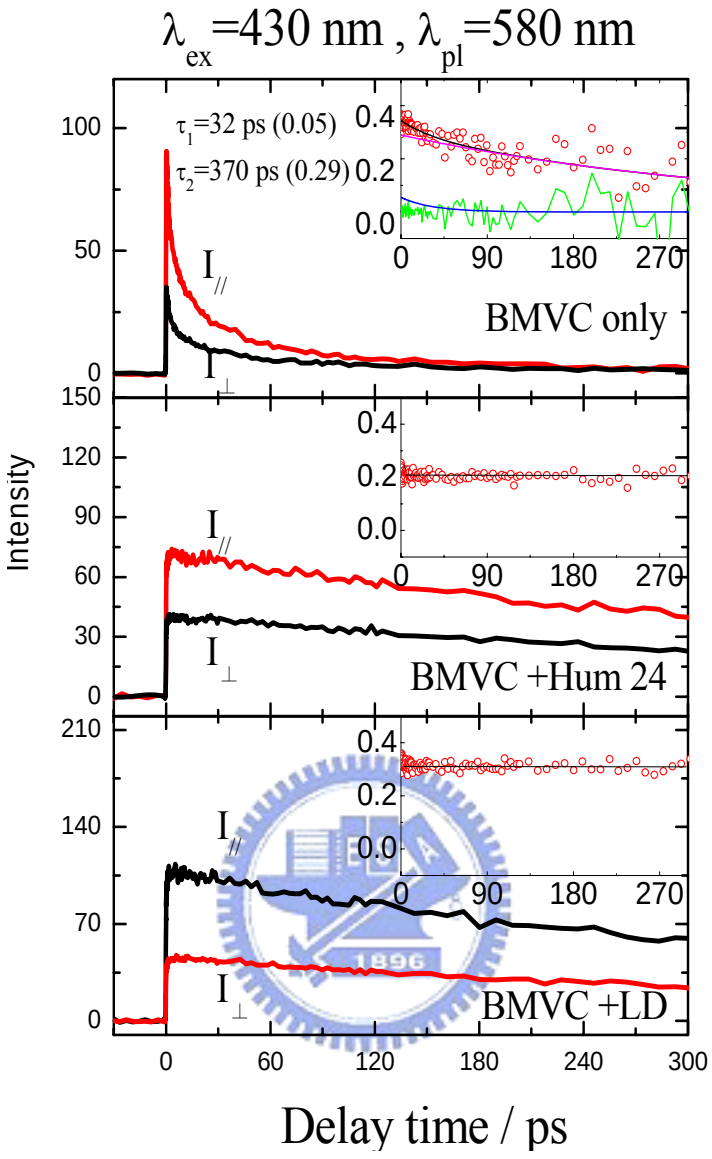

Figure 6.4: Femtosecond time-resolved anisotropy decay of (A)BMVC in tris-buffer, (B) BMVC/Hum24 and (C)BMVC/LD complex.

The reconstructed TRES are shown in Figure 6.5B, and the net spectral shift is 881 cm^{-1} within 50 ps. This result is smaller than that in tris-buffer (~2300 cm^{-1}). Similar decrease of the stoke shift in dye/DNA system is also observed in previous studies.[28,29] This result indicated that in BMVC/LD complex, BMVC molecules are located in relative nonpolar environment in comparison with that in tris-buffer. Figure

[28] Pal, S. K., Zhao, L. and Zewail, A. H. *Proc. Natl. Acad. Sci.* **2003**, *100*, 8113.
[29] Brauns, E. B., Murphy, C. J. and Berg, M. A. *J. Am. Chem. Soc.* **1998**, *120*, 2449.

6.5C is the corresponding C(t) function, which can be fitted by a bi-exponential decay function with time coefficients of 0.9 ps (0.88) and 8.4 ps (0.12).

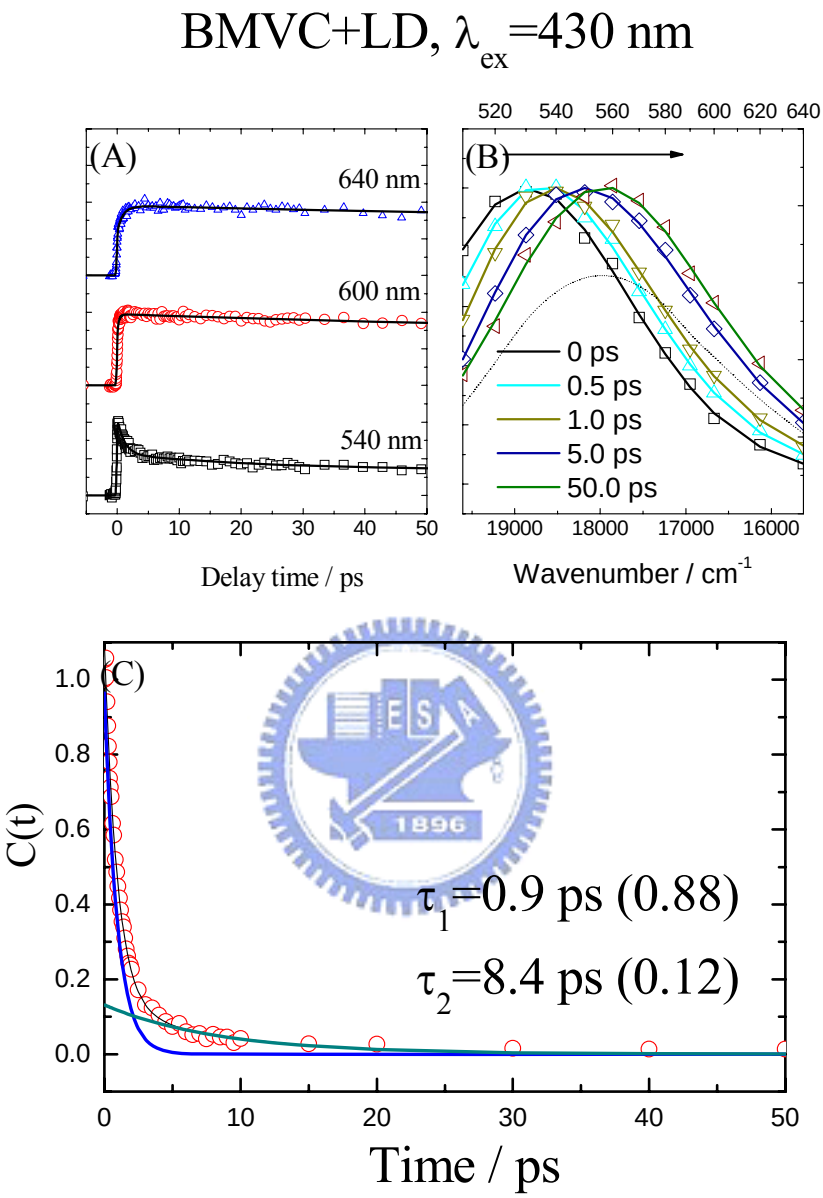

Figure 6.5: (A) The fluorescence transient of BMVC/ LD complex probing at 540 nm, 600nm, and 640 nm. (B) The constructed time-resolved emission spectrum of BMVC/ LD complex at various delay time. (C) The corresponding solvent relaxation spectra of BMVC/ LD complex

In 2003, Zewail group investigated the hydration dynamics of drug in the minor groove of duplex DNA.[28,30] A bi-model hydration behavior was observed, and the results indicated that there are two kinds of water at DNA surfaces: bulk like (labile

[30] Pal, S. K., Zhao, L., Xia, T. and Zewail, A. H. *Proc. Natl. Acad. Sci.* **2003**, *100*, 13746.

water) and weakly bound (order water) water. Therefore, we believe that the 0.9 ps component is contributed form the bulk like water, and the 8.4 ps is attributed to the hydration caused by weakly bound water. However, according to previous study, the hydration process in the minor groove of DNA is determined to be ~20 ps,[28,30] and the observing 8.4 ps process is significant shorter than that. This result indicated that in LD surface, the water close to BMVC has more degree of freedom than that in DNA minor grooves. The possible conformation is within the interface between major and minor groove, thus the effect of bound water is not as strong as that in minor groove.

6.3.5 Hydration dynamics of BMVC/Hum 24 complex

Figure 6.6A is the fluorescence transient of BMVC/Hum24 complex. Like the case of BMVC/LD complex, the fluorescence shows the typical solvation feature. The reconstructed spectra are shown in Fig. 6.6B, and the total spectral shift is 923 cm^{-1} within 50 ps. The decreasing of the stoke shift is similar to that of BMVC/LD complex, and we think that BMVC is also buried in the hydrophobic site of Hum24 DNA. The C(t) function in Fig. 6.6C can be described with a bi-exponential function, and the time coefficients are 1.0 ps (0.6) and 9.5 ps (0.4). The time-scale of those two components is similar to that of BMVC/LD complex, and we believed that they are contributed from the bulk like water and weak bound water. However, the relative amplitude of the weak bound water (9.5 ps) is significantly larger than that in BMVC/LD DNA. The increasing of the relative amplitude of the weak bound water indicates that in BMVC/Hum24 complex BMVC feels more weak bound water,

therefore it might further buried into the DNA surface. The variety of the solvation dynamics of BMVC in LD and Hum24 indicated that it serve as a alternative method to recognize the DNA structure

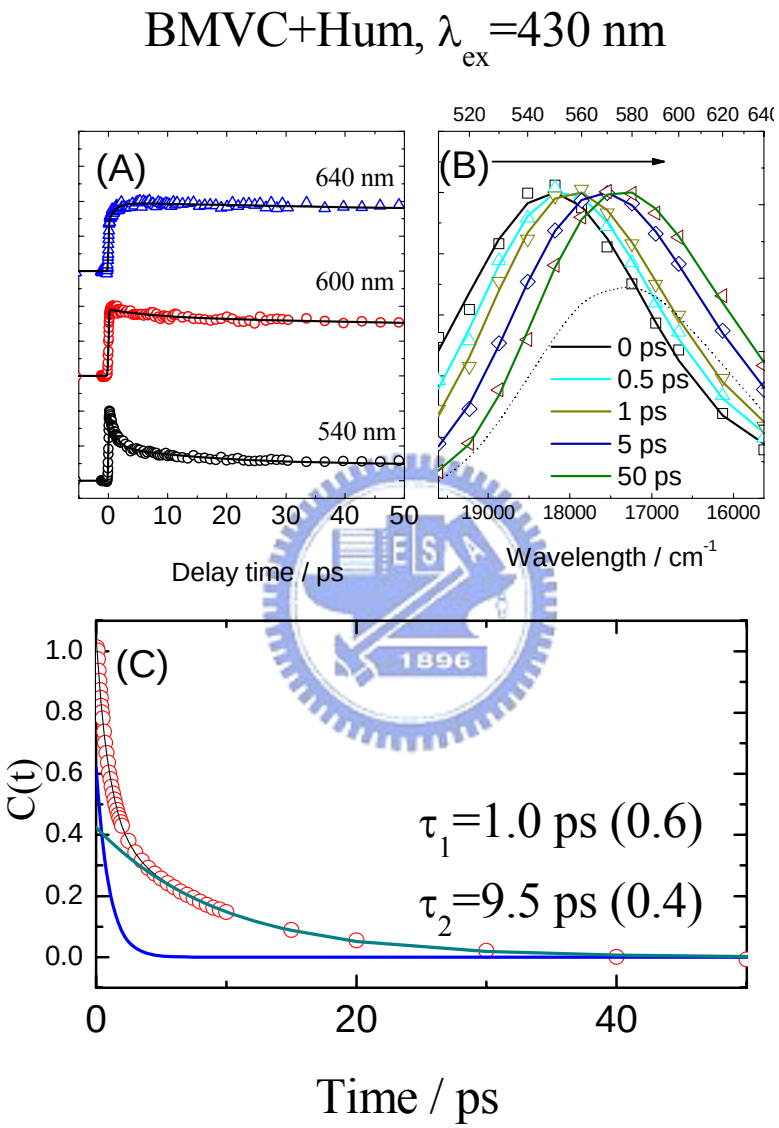

Figure 6.6: (A) The fluorescence transient of BMVC/ Hum24 complex probing at 540 nm, 600nm, and 640 nm. (B) The constructed time-resolved emission spectrum of BMVC/ Hum24 complex at various delay time. (C) The corresponding solvent relaxation spectra of BMVC/ Hum 24 complex

6.4 Concluding Remarks

In this study, we reported the fluorescence enhancement of BMVC/DNA (LD and Hum24) complex. The anisotropy measurement indicates that the segmental motion of BMVC in those two complexes is suppressed. Because similar fluorescence enhancements are also observed for BMVC in high viscosity solvent (glycerol), we concluded that the fluorescence enhancement in BMVC/LD and BMVC/Hum24 complexes is due to the restriction of intramolecular motion. The solvation dynamics of BMVC/DNA complex has also been investigated. For BMVC/LD complex, the C (t) decay with two time coefficient: 0.9 ps and 8.4 ps. The 0.9 ps component is contributed from the solvation process of bulk like water, and the 8.4 ps is attributed to the solvation of weakly bound water. This result indicates that the binding site is located in the interface between major and minor groove. For BMVC/Hum24 complex, the solvation dynamics is similar to that of BMVC/LD complex. However, the relative amplitude of the weakly bound water is significantly larger than that of BMVC/LD complex, which indicated that BMVC is buried in the relative hydrophobic site of the DNA macromolecule.

Appendix A

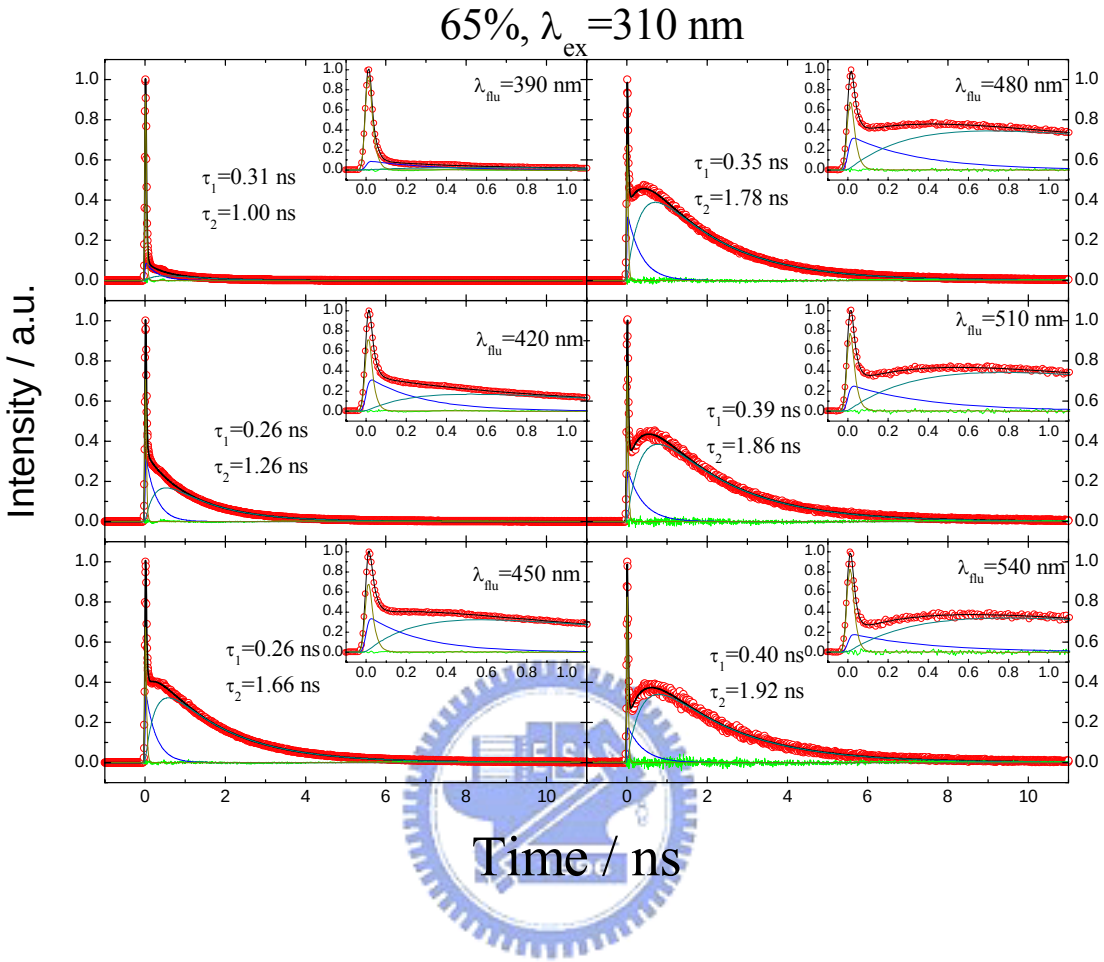

Appendix A-1: The time-resolved transient of PPB in 65 % water/THF solution. The excitation wavelength is fixed at 310 nm.

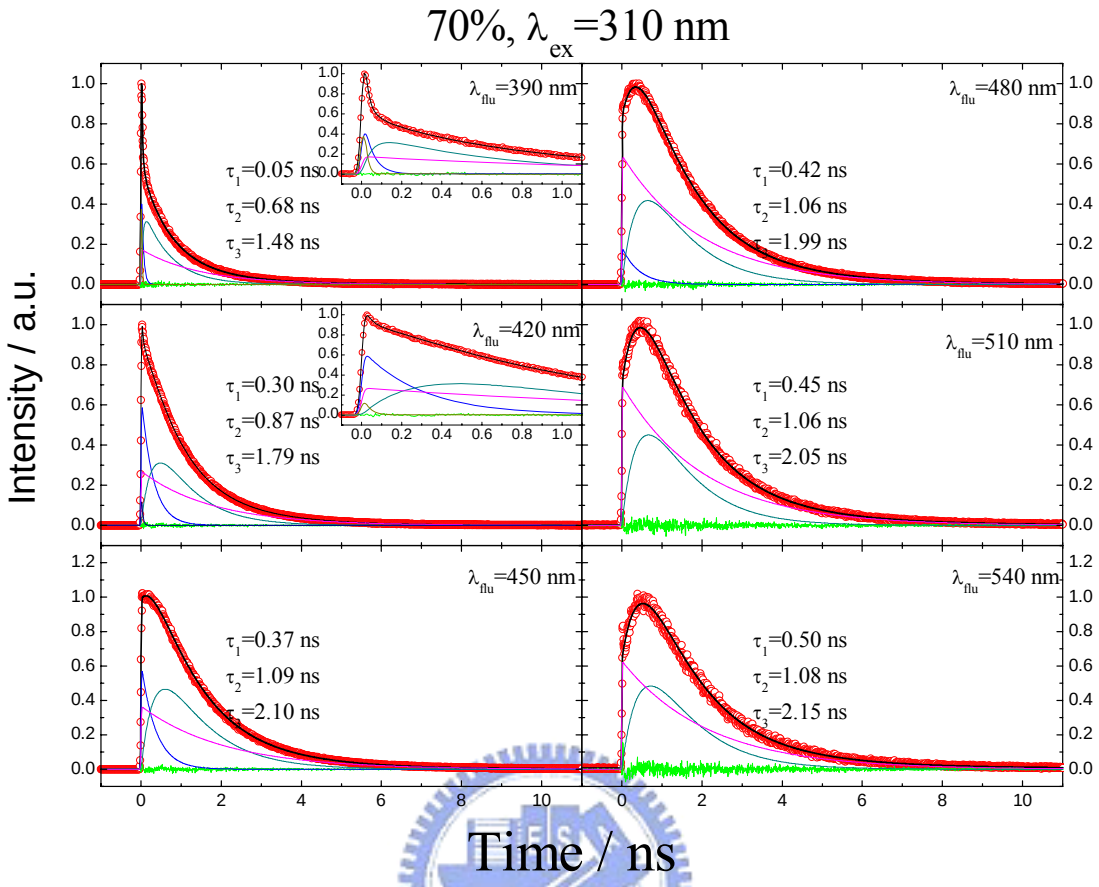

Appendix A-2: The time-resolved transient of PPB in 70 % water/THF solution. The excitation wavelength is fixed at 310 nm

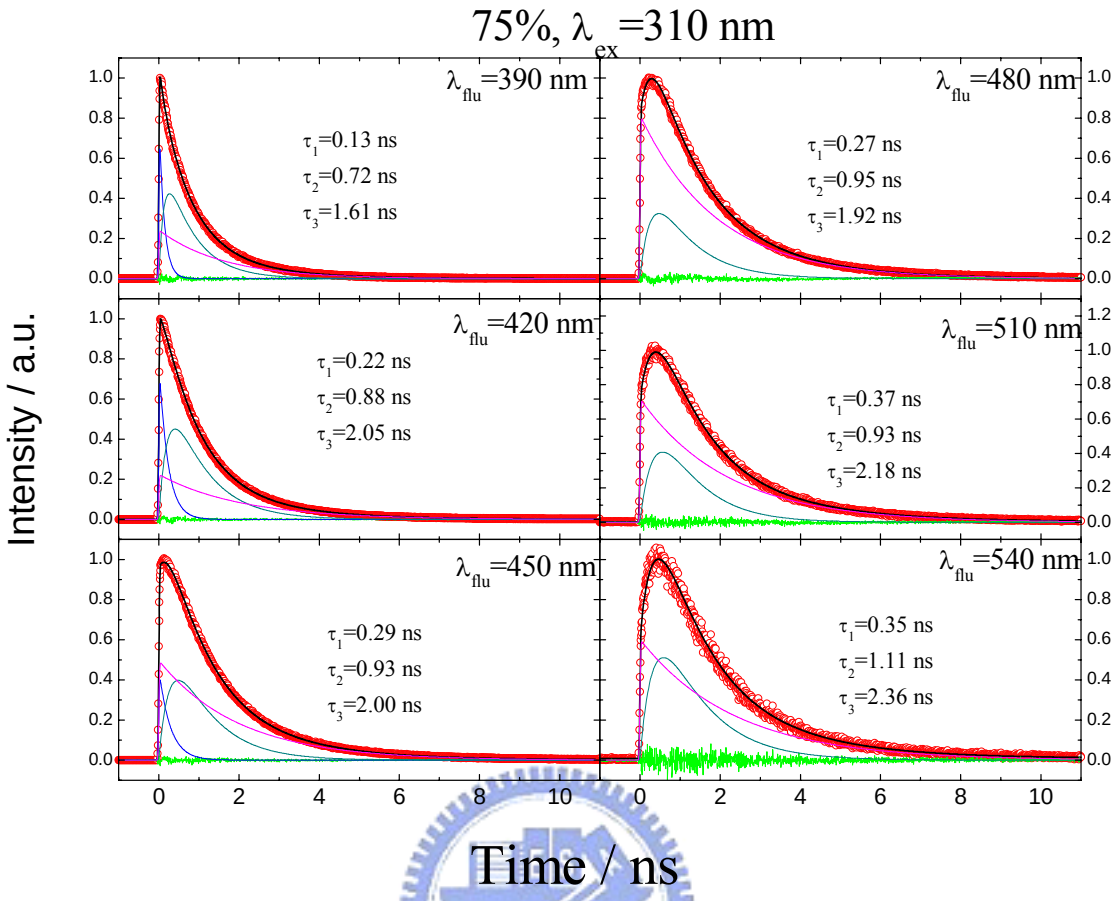

Appendix A-3: The time-resolved transient of PPB in 75 % water/THF solution. The excitation wavelength is fixed at 310 nm

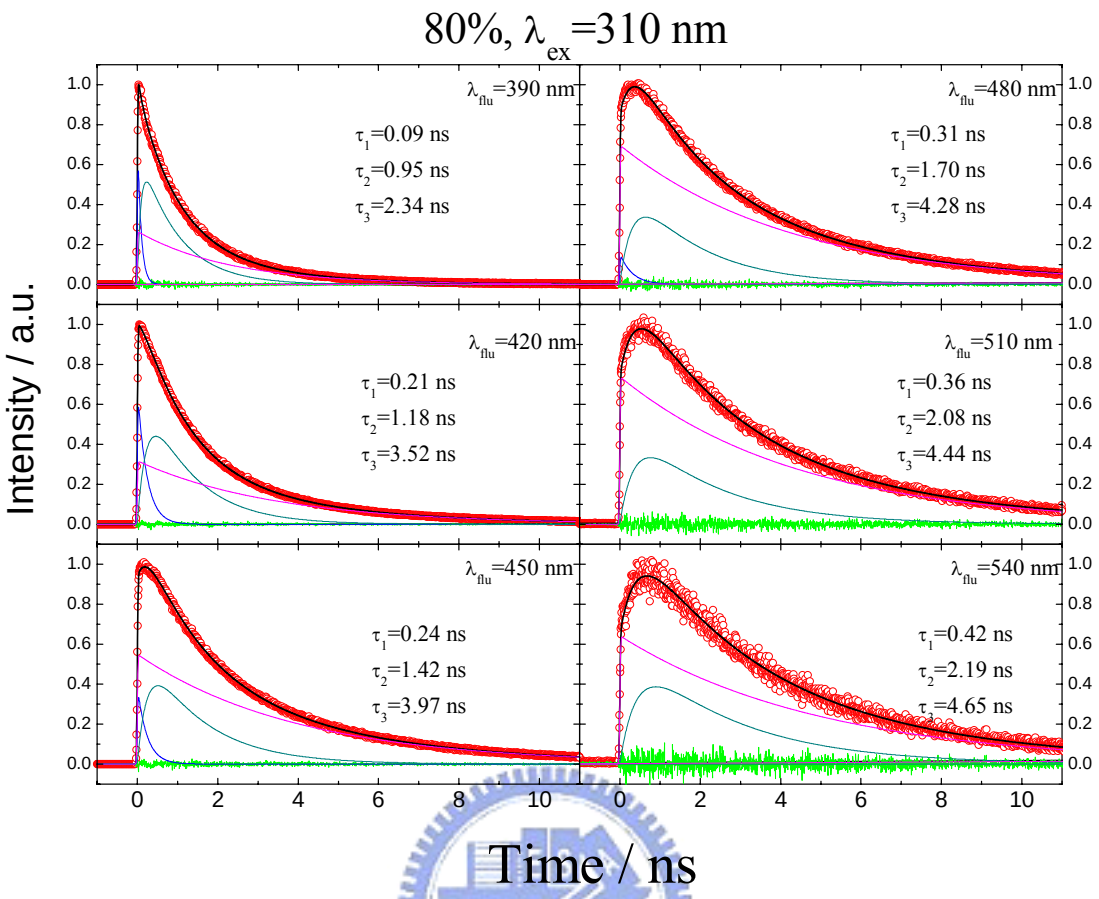

Appendix A-4: The time-resolved transient of PPB in 80 % water/THF solution. The excitation wavelength is fixed at 310 nm

Appendix B

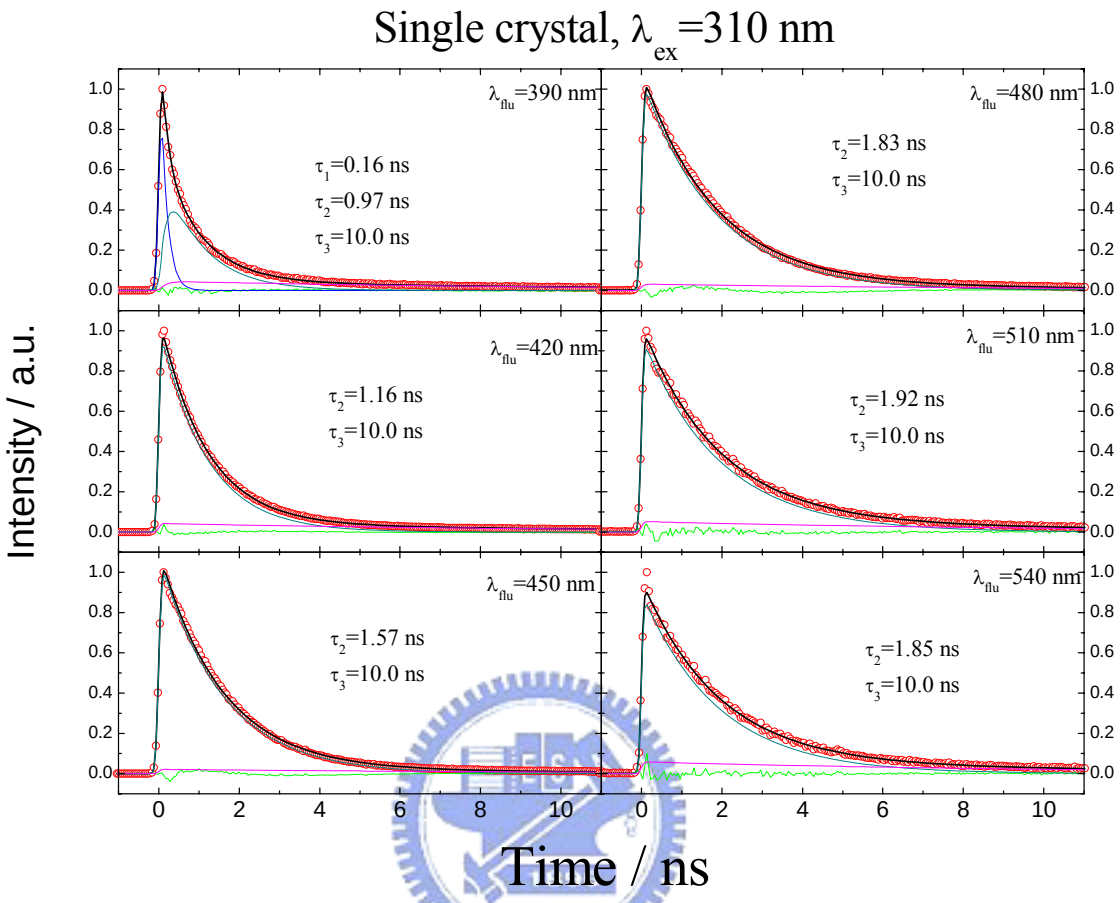

Appendix B-1: The time-resolved transient of PPB single crystal. The excitation wavelength is fixed at 310 nm.

Appendix C

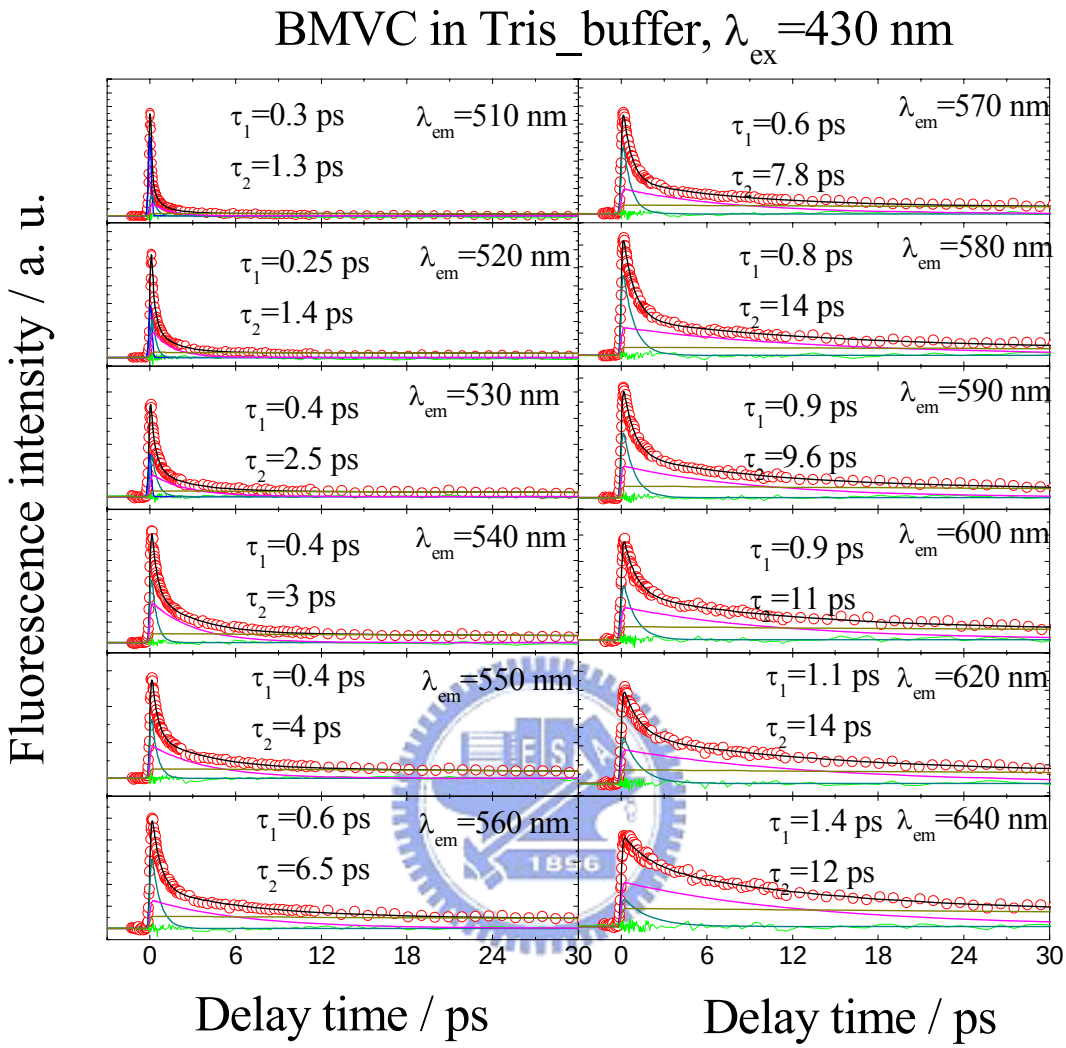

Appendix C- 1: The deconvolution of the time-resolved transients of BMVC in Tris-HCl solution

Appendix D

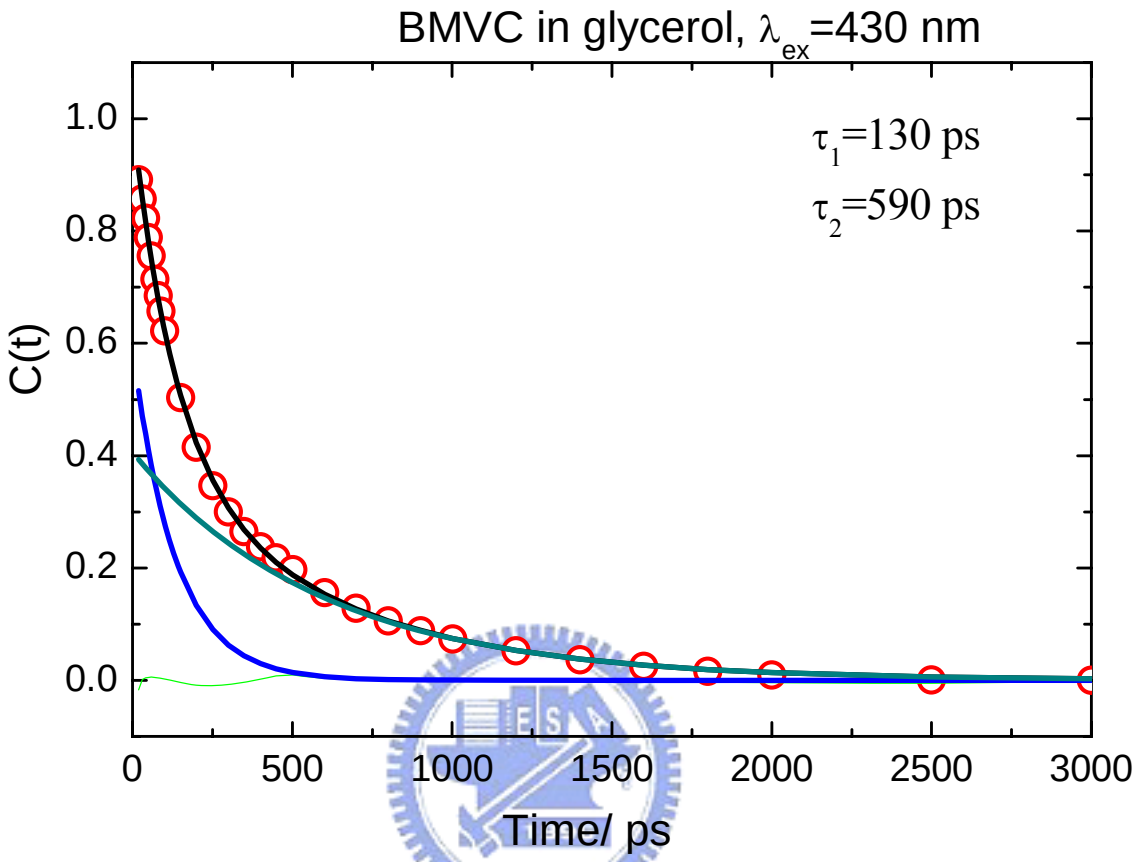

Appendix D-1: The solvent response function , C(t), of BMVC in glycerol. The spectra was obtained using TCSPC technique